
Development of Active Vibration Control System for Gearbox Housings

Author: Sneha Rupa Nampally, M. Sc.

Herausgeber: Prof. Dr.-Ing. S. Rinderknecht



TECHNISCHE
UNIVERSITÄT
DARMSTADT

Nampally, Sneha Rupa
Development of Active Vibration Control System for Gearbox Housings
Darmstadt, Technische Universität Darmstadt
Jahr der Veröffentlichung der Dissertation auf TUpriints: 2024
Veröffentlicht unter CC-BY-NC 4.0 International
<https://creativecommons.org/licenses/>
Tag der mündlichen Prüfung: 22.10.2024

Eine gebundene Ausgabe ist bei der Shaker Verlag GmbH, Düren erhältlich.



Development of Active Vibration Control System for Gearbox Housings

Am Fachbereich Maschinenbau
an der Technischen Universität Darmstadt
zur
Erlangung des Grades eines Doktor-Ingenieurs (Dr.-Ing.)
genehmigte

Dissertation

vorgelegt von
Sneha Rupa Nampally, M.Sc.
aus Hyderabad, Indien

Berichterstatter:	Prof. Dr.-Ing. Stephan Rinderknecht
Mitberichterstatter:	Prof. Dr.-Ing. Tobias Melz
Tag der Einreichung:	02.09.2024
Tag der mündlichen Prüfung:	22.10.2024

Darmstadt 2024
D17



Declaration

I hereby declare that I have written this thesis independently. Acknowledgements of help and feedback acquired during this work have been duly credited. The "Principles for Safeguarding Good Scientific Practice at the Technical University of Darmstadt" and the "Guidelines for Handling Digital Research Data at the TU Darmstadt" were observed in the respective current versions when writing the dissertation.

02. September 2024, Darmstadt

Sneha Rupa Nampally



Acknowledgements

I would like to express my deepest gratitude to my supervisor Prof. Dr.-Ing. Stephan Rinderknecht for placing his trust in my abilities and offering me this chance to pursue my PhD under his guidance at IMS. I am extremely grateful for the continuous support of Prof. Dr.-Ing. Rainer Nordmann, Prof. Dr.-Ing. Tobias Melz and Dr. Mauro Fontana for their valuable guidance throughout this project. Their constructive feedback has been instrumental in shaping both this thesis and my development as a researcher.

My sincere appreciation goes to Mr. Sherif Okda for his unwavering support and contributions, particularly in setting up test-rig prototypes and coordinating the tests for successful completion. I am thankful for the insightful guidance of Dr.-Ing. Zhihong Liu for his mentorship in the execution of tests at IMS and his constructive feedback on the validation tests.

I would like to thank the EU H2020 Marie-Curie ITN Network for providing the financial support that made this research possible. Additionally, I am grateful for the fruitful collaboration within the H2020 LIVE-I project with all the researchers involved.

To my colleagues at Powerflex in Italy, Dario, Nando and Enzo including Dr. Mauro Fontana - I would like to express my heartfelt gratitude in helping me navigate the Italian life and culture.

I am grateful for the valuable comments provided by Sidharth Dave, Guanlin Gao, and Christian Fischer, which have certainly helped in shaping this thesis. To my dear friends and colleagues at IMS, thank you for creating a welcoming working atmosphere. I also owe this milestone to my roommates Eslem and Lin, who have been my emotional support system during my time in Darmstadt.

I am extremely indebted to my family back in India for their belief in my choices and their unending support in my endeavours. Without their love this would not have been possible. I am glad to have shared this PhD journey alongside my dear husband, Aman. His valuable inputs as a researcher and a partner, despite the distance fuelled my motivation throughout this PhD.



Abstract

This thesis presents a systematic approach to developing an active vibration control system for lightweight transmissions by placing piezoelectric inertial mass actuators on the gearbox housing. The main objective is to minimise the structure-borne vibrations caused by gear whine at the mounting points of the gearbox where it is connected to the car body. These vibrations, particularly in the frequency range of 1000 - 5000 Hz, can be amplified into audible noise in the passenger compartment, reducing comfort.

The development process begins with studying the system's dynamics through two gearbox housing models. The first model is a simplified version of a dual-clutch transmission with a non-rotating load, analysed using ANSYS to determine actuator requirements. The second model is a hybridized version of a fully operational dual-clutch gearbox, modelled with Romax to simulate dynamic behaviour under realistic excitation, helping establish actuator force requirements, placement, and control strategies.

Macro-Fibre Composites (MFCs) are chosen as sensors for their low cost and wide operating bandwidth in the desired frequency range. They are calibrated for use in place of piezoelectric accelerometers. A real-time system is constructed with a microcontroller development board for high-speed data acquisition from the MFCs and closed-loop control implementation with the actuators.

Optimal actuator placement is determined using Frequency Response Functions (FRFs) from an experimentally correlated model of the gearbox and actuator. The optimization considers spatial and modal controllability in the frequency domain. The thesis discusses single and paired actuator positioning.

Multi-point control approaches based on the FxLMS algorithm are developed to minimize vibrations at the mounting points within the computational constraints of a microcontroller. Three variations—single input multi-output, mixed error, and switched error algorithms—are studied and compared. Mixed and switched error algorithms reduced the computational time of multi-point control by almost half compared to single input multi-output approach.

The active vibration control system is demonstrated on an operational gearbox, achieving vibration attenuation of 4 - 14 dB can be achieved with both switched and mixed error approaches at 2500 Hz. The mixed error algorithm proved to be most feasible to implement given its comparable performance in achieving vibration reduction across all points and computational simplicity. The thesis also discusses the cost and weight implications of the add-on system.



Kurzfassung

Die Arbeit beschreibt die Entwicklung eines aktiven Schwingungsminderungssystems für Leichtbaugetriebe mithilfe von piezoelektrischen Aktoren am Getriebegehäuse. Ziel ist es, Körperschall-schwingungen zu minimieren, die durch das Heulen des Getriebes an den Befestigungspunkten entstehen, insbesondere im Frequenzbereich von 1000 bis 5000 Hz, um den Fahrkomfort zu verbessern.

Der Entwicklungsprozess beginnt mit der Untersuchung der Systemdynamik anhand zweier Getriebemodelle. Ein vereinfachtes Modell eines Doppelkupplungsgetriebes wird mit ANSYS analysiert, um die Anforderungen an die Aktuatoren zu bestimmen. Ein weiteres Modell, eine hybridisierte Version eines voll funktionsfähigen Doppelkupplungsgetriebes, wird mit Romax modelliert, um das dynamische Verhalten unter realistischer Anregung zu simulieren.

Makrofaserverbundwerkstoffe (MFC) werden als kostengünstige Sensoren mit großer Betriebsbandbreite eingesetzt. Ein Echtzeitsystem mit einem Mikrocontroller Entwicklungsboard wird für die Datenerfassung und Aktuatorsteuerung implementiert.

Die optimale Aktuatorplatzierung erfolgt mithilfe von Frequenzgangfunktionen (FRFs) aus einem experimentell korrelierten Modell. Die Optimierung berücksichtigt die räumliche und modale Kontrollierbarkeit. Die Dissertation erörtert die Positionierung einzelner und gepaarter Aktoren.

Zur Schwingungsminimierung werden Mehrpunkt-Regelungsansätze basierend auf dem FxLMS-Algorithmus entwickelt. Drei Varianten - Single-Input-Multi-Output, Mixed-Error und Switched-Error - werden verglichen. Das aktive Schwingungsminderungssystem wird an einem betriebsbereiten Getriebe demonstriert, wobei eine Schwingungsminderung von 4 - 14 dB sowohl mit geschalteten als auch mit gemischten Ansatz bei 2500 Hz erreicht werden. Der Mixed-Error-Algorithmus erwies sich als am praktikabelsten, da er vergleichbare Leistung bei der Schwingungsreduzierung in allen Punkten und Vibrationsreduzierung in allen Punkten und der Einfachheit der Berechnungen. Die Arbeit befasst sich auch mit den Auswirkungen des Zusatzsystems auf Kosten und Gewicht .

Contents

Declaration	i
Acknowledgements	iii
List of symbols	x
1 Introduction	1
1.1 Aim of research	3
1.2 Scope of research	4
1.3 Introduction to the gearboxes	5
1.4 Research questions	7
1.5 Structure of thesis	8
2 State of the art	11
2.1 Vibration behaviour of gearbox housings	11
2.2 General overview of active vibration control	12
2.3 Modelling of high frequency dynamics of gearbox vibrations	13
2.4 Review of sensors and actuators	19
2.5 Review of actuator placement techniques	21
2.6 Review of hardware for control system deployment	28
2.7 Review of relevant control algorithms	29
3 Modelling of high frequency gear whine dynamics	33
3.1 Model of the prototyping gearbox	34
3.2 Model of the demonstration gearbox	49
3.3 System Level Simulation model	63
4 Sensor architecture	65
4.1 Sensing scheme for gearbox	65
4.2 Principle of operation of MFC	66
4.3 Design of the signal conditioning for MFCs	69
4.4 Calculation of parameters of signal conditioning	71
4.5 Calibration of the MFC sensor	72
5 Strategy for actuator placement	81
5.1 Coupling of actuator dynamics with gearbox housing	83

<hr style="border: 2px solid yellow;"/>	
5.2	Actuator placement criteria 89
5.3	Single actuator positioning 94
5.4	Derivation of actuator combination 96
6	Control algorithms for multi-point control 101
6.1	Mathematical basis of SISO FxLMS algorithm 102
6.2	SIMO-FxLMS algorithm 104
6.3	Switched-error FxLMS algorithm 107
6.4	Mixed-error FxLMS algorithm 109
7	Experimental validation 113
7.1	Comparison of algorithms 121
7.2	Projected FxLMS algorithm 125
7.3	System level economics 128
8	Conclusions and outlook 131
A	Hardware details of developed AVC system 137
A.1	Sensor data and actuator data 137
A.2	Data Acquisition (DAQ) board 138
A.3	Details of IC chips used 139
B	MADYN analysis for bearing stiffness 141
C	References 145

List of symbols

Latin symbols

Symbol	Meaning	Unit
A	State matrix in state space system	
A_A	Cross section area of IMA stack	m^2
A_d	Block Diagonal representation of $[A_{gt}]$ and $[A_{gb}]$ combined diagonally	
$[A_{gb}]$	State space matrices of geartrain model, similar for $[B_{gb}]$, $[C_{gb}]$, $[D_{gb}]$	
$[A_{gt}]$	State space matrices of geartrain model, same for $[B_{gt}]$, $[C_{gt}]$ and $[D_{gt}]$	
B	Input matrix in state space system	
B_d	Block Diagonal representation of $[B_{gt}]$ and $[B_{gb}]$ combined diagonally	
C	Output matrix in state space system	
C_d	Block Diagonal representation of $[C_{gt}]$ and $[C_{gb}]$ combined diagonally	
$C_{d,ac}$	Truncated part of C_d related to the acceleration outputs	
\mathcal{B}^s	Set of all possible sensor locations on gearbox	
c_p	Piezoelectric element damping coefficient in IMA	
c_j	Joint damping coefficient of IMA attachment point on gearbox	
C	Capacitor	nF
\mathcal{C}	Controllability matrix	
C_l	Discrete actuator combination set in the gearbox	
C_{opt}	optimised 2- actuator combination	
$C_{H\beta}$	Lead slope of gear microgeometry	μm
C_β	Lead crowning of gear microgeometry	μm
$C_{H\alpha}$	Involute slope of gear microgeometry	μm
C_α	Involute barelling of gear microgeometry	μm
D	Direct transmission matrix in state space system	
D_d	Block Diagonal representation of $[D_{gt}]$ and $[D_{gb}]$ combined diagonally	
$D_{d,ac}$	Truncated part of D_d related to the acceleration outputs	
$\hat{d}(t)$	Primary path vibration at sensor due to gear whine	
d_{33}	piezoelectric constant	
D_q	Electrical displacement density	C/m^{-2}
e	Exponent	2.718
E	Electrical Field	V m^{-1}
F_p	Force in IMA element	N
F_a	Total Force exerted by IMA on gearbox	N

$f_n(P_i)$	Spatial H2 norm for actuator position P_i across all sensor points	
$f_n(C_l)$	Spatial H2 norm for actuator combination C_l across all sensor points	
F_{piezo}	Force exerted by piezo exciter in Prototype gearbox	N
G	3D secondary path matrix	
G_s	Gain parameter in Acceleration MFC transfer function	
\mathcal{H}_2	2-Norm	
\mathcal{H}_∞	H_∞ norm	
$H_{bea,A2}$	transfer function from piezo exciter to point A2 via the bearing connection point	
$H_{fix,A2}$	transfer function from piezo exciter to point A2 via the testrig frame	
$\hat{H}_{mix,n}$	Secondary path transfer function of mixed error	
$\hat{H}(s_1, P_1, \omega_n)$	Transfer function from actuator P_1 to sensor s_k at frequency ω_n	
I	Identity matrix	
j	Complex number	$\sqrt{-1}$
k_p	Piezoelectric element stiffness in IMA	$N m^{-1}$
k_j	Joint stiffness of IMA attachment point on gearbox	$N m^{-1}$
L_m, M_m, N_m	Numerator coefficients in acceleration MFC transfer function	
\mathbb{L}	Total number of actuator combinations	
m_a	Moving mass of IMA	g
m_b	Mass of IMA base	g
\mathcal{M}_C	Modal controllability matrix for actuator combinations	
\mathcal{M}_P	Modal controllability matrix for discrete actuator positions	
$\mathcal{M}_n(P_i)$	relative modal controllability index for actuator Position P_i	
$\mathcal{M}_n(C_l)$	relative modal controllability index for actuator combination C_l	
n_A	Number of Layers in piezostack	
n_a	Number of actuators required for control	
n_c	Number of actuators in a combination C_l	
n_{mix}	Number of sensors mixed to form the mixed error signal	
n_s	Total number of mounting point sensors on gearbox	
N	Number of Degrees of Freedom in the system	
N_a	Total number of actuator positions possible on gearbox	
p, q, r	Notations of directions in MFC	
P_a, Q_a	Denominator coefficients in acceleration MFC transfer function	
P_i	Discrete actuator position in the gearbox	
P_{opt}	optimised single actuator position	
$\hat{q}(t)$	Total vibration measured at sensor on gearbox	
$\hat{q}_{sw,n}(t)$	Instantaneous switched error sensor vibration	
$\hat{q}_{mix,n}(t)$	Instantaneous vibration at mixed error sensor	
$[Q_f]$	Constraint mapping matrix	
r_1	Location of actuator on gearbox	
R	Electrical resistance	Ω
S_q	Strain in direction q	

$s = j\omega_n$	Laplace variable	
s_k	kth sensor position in gearbox	
S_i	Spatial controllability measure of actuator position P_i	
S_l	Spatial controllability measure of actuator combination C_l	
S_{qac}	Sensitivity of accelerometer	V/m^{-2}
\hat{S}_i	Spatial controllability score of actuator position P_i	
\hat{S}_l	Spatial controllability score of actuator combination C_l	
T_q	Stress in direction q	N/m^{-2}
Δt	Time step	s
t	Instantaneous time	s
$TF_{S21,n}$	Transmissibility function between sensors S_2 and reference S_1	
t_s	Switching time	
$\hat{U}_a(t)$	Control voltage to IMA	
$\{u_{gt}\}$	Input force vector for geartrain model	
$\{u_{gb}\}$	Input force vector for gearbox housing model	
V_{IMA}	Voltage supplied to IMA	V
V_{DC}	DC Voltage offset	V
$V_{acc}(s)$	Voltage readout at accelerometer	V
W_c	Measure of Controllability	
W_s	Weighting matrix for sensors	
w_k	Weight of individual sensor s_k	
$\{x\}$	Combined state vector of geartrain model	
x_a	Displacement of moving mass of IMA	m
x_b	Displacement of IMA base mass	m
x_g	Displacement of gearbox surface	m
$\{x_{gt}\}$	State vector of geartrain model	
$\{x_{gb}\}$	State vector of gearbox housing model	
$X_n(t)$	Reference signal containing sine and cosine of gear mesh frequency	
$\{y\}$	Combined output vector of gearbox housing model	
$\{y_{gt}\}$	Measured outputs vector of geartrain model	
$\{y_{gb}\}$	Measured outputs vector of gearbox housing model	
$Y_{gt,A2}$	Vibration at the position A2 in the prototype gearbox	

Greek symbols

Symbol	Meaning
α	Rayleigh damping parameter 1
β	Rayleigh damping parameter 2
β_m	Modal controllability limit at each frequency
Γ_1	Diagonal matrix of square of resonance frequencies
Γ_2	Diagonal matrix of square of with modal damping
ϵ_T	is the dielectric constant (permittivity) under constant stress T in the p-direction
ζ	Damping ratio
μ	Step size of FxLMS
ξ	Error function : SISO
ξ_{mix}	Error function : mixed error
ξ_{simo}	Error function : SIMO
ξ_{sw}	Error function : switched
ϕ	Phase delay in secondary path transfer function
$\phi_{mix,n}$	Phase delay of mixed error sensor
ω_n	n^{th} Frequency
Ω^a	Set of all possible actuator locations on gearbox

Hz

Notation

Symbol	Meaning
$\exp()$	Exponential function
\dot{r}, \ddot{r}	Time differentiation $dr/dt, dr/dt^2$
\mathbf{r}^T	Transpose of \mathbf{r}
\mathbf{r}^*	Complex conjugate of \mathbf{r}
\mathbf{r}^H	Transposed complex conjugate von \mathbf{r}
$r[n]$	Discrete sample r at time point $t = n \Delta t$
$ r $	Absolute value of r

List of abbreviations

Abbrev.	Full form
ADC	<i>Analog to Digital Converter</i>
AVC	<i>Active Vibration Control</i>
BEM	<i>Boundary Element Methods</i>
CAN	<i>Control Area Network</i>
CMS	<i>Component Mode Synthesis</i>
DAC	<i>Digital to Analog Converter</i>
DAQ	<i>Data Acquisition</i>
DC	<i>Direct Current</i>
DCT	<i>Dual Clutch Transmission</i>
DOF	<i>Degree of Freedom</i>
EOL	<i>End of Line</i>
FEA/M	<i>Finite Element Analysis/ Method</i>
FPGA	<i>Field Programmable Gate Array</i>
FRF	<i>Frequency Response Function</i>
FxLMS	<i>Filtered-x Least Means Square</i>
GBTE	<i>Gearbox Transmission Error</i>
GMF	<i>Gear Mesh Frequency</i>
HDT	<i>Hybridised Dual Clutch Transmission</i>
IC	<i>Integrated Circuit</i>
ICP	<i>Integrated Circuit-Piezoelectric</i>
IEPE	<i>Integrated Electronic Piezo Electric</i>
IMA	<i>Inertial Mass Actuator</i>
LMS	<i>Least Mean Squares</i>
LOA	<i>Line of Action</i>
LQ	<i>Linear Quadratic</i>
LTI	<i>Linear Time Invariant</i>
MCU	<i>Microcontroller Unit</i>
MEMS	<i>Micro-Electro-Mechanical Systems</i>
MFC	<i>Macro Fibre Composite</i>
MIMO	<i>Multi Input Multi Output</i>
MOR	<i>Model Order Reduction</i>
MPB(s)	<i>Mounting Point(s) Back</i>
MPF(s)	<i>Mounting Point(s) Front</i>
NVH	<i>Noise Vibration and Harshness</i>
OEM	<i>Original Equipment Manufacturer</i>
Op-Amp	<i>Operational Amplifier</i>
PCB	<i>Printed Circuit Board</i>
PI	<i>Performance Index</i>

PID	<i>Proportional-Integral Differential</i>
PSD	<i>Power Spectral Density</i>
PVDF	<i>Polyvinylidene Fluoride</i>
RMS	<i>Root Mean Square</i>
RQ	<i>Research Question</i>
SBC	<i>Single Board Computer</i>
SEA	<i>Statistical Energy Analysis</i>
SIMO	<i>Single Input Multi Output</i>
SISO	<i>Single Input Single Output</i>
SLS	<i>System Level Simulation</i>
TCU	<i>Transmission Control Unit</i>
TE	<i>Transmission Error</i>
TF	<i>Transfer Function</i>
TPA	<i>Transfer Path Analysis</i>
UUT	<i>Unit Under Test</i>



1 Introduction

One of the key trends in gearbox development is lightweight construction. This is pursued by automotive transmission manufacturers by incorporating advanced materials like including high-strength steels, aluminium alloys, magnesium, plastics, and composites coupled with additive manufacturing techniques. These lightweighting efforts in gearboxes contribute to overall vehicle efficiency improvements and help automotive manufacturers meet increasingly stringent emissions standards. A direct consequence of lightweight construction improved energy efficiency [29] for the vehicle but the major disadvantage is increased vibration and noise. With hybridisation and push towards electrification, transmission noise would be a greater contributor for Noise, Vibration and Harshness (NVH). Hybridised transmissions contain additional gearsets connecting the main transmission to the electrical motor, leading to more sources of vibration. The absence of broadband engine noise in electric driving modes would lead to a greater perception of high-frequency noise generated by structure-borne paths in the cabin. The major types of transmission noise are described as follows with their source and frequency ranges in Figure 1.1.

Gear whine phenomenon

In lightweight transmissions, gear whine is the main contributor of noise [138]. Gear whine phenomenon originates at the gear mesh as a consequence of deviations and imperfections in gear design and manufacturing, along with tooth deflections due to loading. This causes transmission error, the deviation from ideal relative displacement of the gear pair in contact. Even with perfectly manufactured teeth, tooth deflections occur due to flexibility of shafts, bearings and their housing attachment points eventually leading to transmission error.

Gear whine is a tonal disturbance whose frequency is characterised by multiplying the rotational speed by the number of teeth of the pinion of the gear pair. This frequency is called the Gear Mesh Frequency (GMF).

The NVH properties of transmission can be improved at various levels of the gearbox development. To target the structure borne vibrations originating as a consequence of gear-whine, various solutions ranging from gear modification to installing additional support bearings to shafts and active bearings have been proposed [53]. Till date no demonstration of active treatment of vibration control for the housing exists.

NVH evaluation by the transmission manufacturer are conducted at End-of-Line (EOL) of the manufacturing. In this process, an accelerometer is mounted at an agreed position

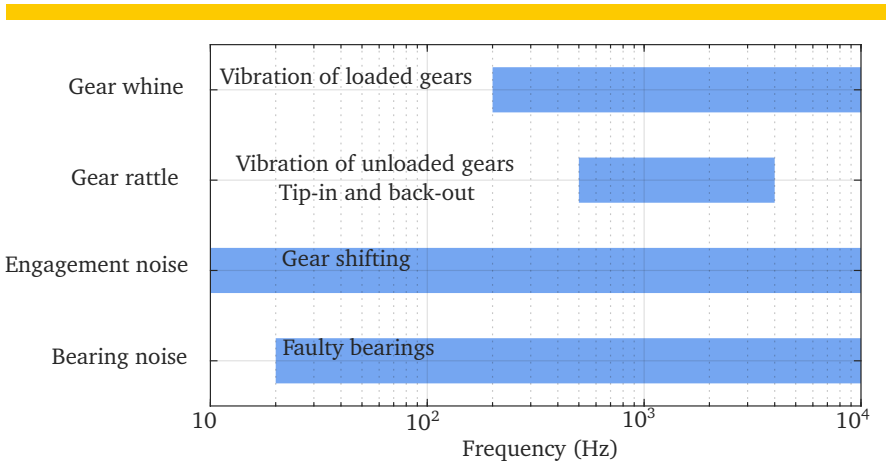


Figure 1.1: Major Sources of vibrations and noise in automotive transmissions [102]

with the Original Equipment Manufacturer (OEM). A ramp up test is performed and the vibration recorded by the accelerometer is placed at a position correlated to the structure borne vibration transfer path into the passenger cabin. A subjective rating of this measured acceleration value [9] is often assigned, that is decided in agreement with the vehicle OEM.

Vibration transfer paths

There are two major paths of vibration transfer in the gearbox, namely, airborne and structure borne paths as depicted in Figure 1.2. The airborne transfer path is directly from the gearbox housing wall into the car cabin. The structure borne vibration transfer of the gear whine originating at the gear mesh takes place via the shafts, bearings, the housing into the car body via the mounting points of the transmission to the car frame. The airborne noise inside the sealed compartment of the gearbox does not possess high energy to exit the gearbox. Structure borne noise plays a significant role in overall transmission noise, primarily propagating through shafts and bearings to the gearbox housing. The bending and torsional vibrations of rotating shafts induce vibrations in the housing structure. When the frequency of excitation is close to the natural frequency of the housing, vibrations are significantly amplified and transmitted into the car body via mounting points [102].

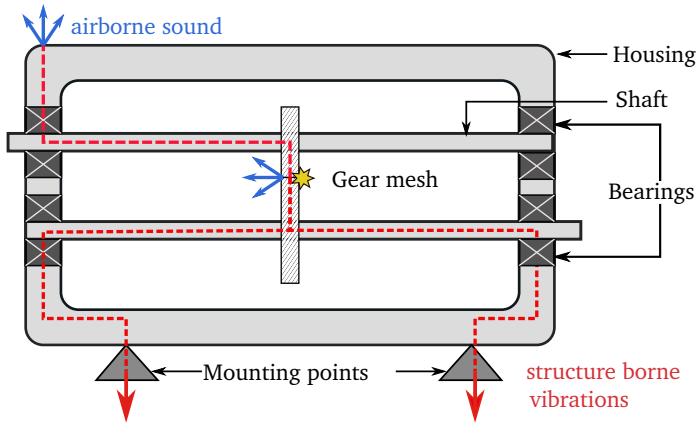


Figure 1.2: Gear whine transfer path of structure borne vibrations and airborne sound

1.1 Aim of research

The main focus of this thesis is to develop an Active Vibration Control (AVC) system for minimizing the structure borne vibration transfer at the mounting points of the gearbox housing due to gear whine.

Passive vibration control approaches such as isolation mounts may in some cases add weight and are not adaptable to different operating conditions of the gearbox. Imposing stringent manufacturing tolerances of transmission components can also increase cost of production, hence the development of an AVC solution is proposed in this thesis. An add-on AVC helps keep the overall costs of production of the lightweight transmission with stricter tolerances under check while still staying in the limits of minimum added weight. An external force is applied via an actuator in an adaptive manner to control the structure borne vibrations at the desired locations. The housing is targeted because an actuator placed farther downstream of the vibration source can be designed to have lower force requirements for the control of vibrations. Also installation of an add-on solution to already serially produced transmissions can be easily realised without major design changes. Lower forces translate to lower power requirements for the actuator.

The system should be easy to implement in a limited computational environment such as microcontrollers in automotive control units. This work deals with the development of the active vibration control approach at a system level design, where each subsystem associated vibration reduction objectives.

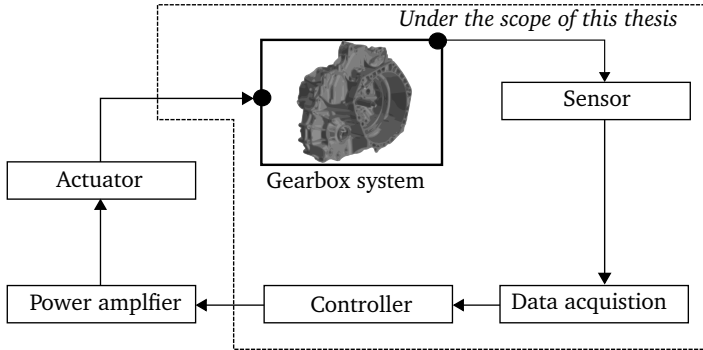


Figure 1.3: Scope of research

System level approach to development

The main elements of the active vibration control system are shown in Figure 1.3. System level model deals with seamless integration of various subsystem coupling for evaluation. For example, the controller, actuator and sensor dynamics can be independently tuned in the overall system model. Different types of sensors and actuators can be "plugged" into the system model for direct evaluation. This type of modular model makes qualified comparison of different concepts in the early phase of the design process affordable. This approach can be easily extended to different gearbox models by replacing the mechanical model in the "Gearbox System" block indicated in Figure 1.3. A detailed description of the system level model is provided in Section 3.3 of Chapter 3.

Once the system level model is established, its optimization of various subsystems can be performed. A study regarding the economic feasibility of implementation of the entire system can be done following the final model. This thesis is organised subsystem-wise, each chapter dealing with development of each of the subsystems.

1.2 Scope of research

The work has been executed in close technical cooperation with researchers within the framework of the H2020 LIVE-I project. A clear demarcation of area of developments of the active vibration control system has been depicted in Figure 1.3. The focus of this thesis lies in dealing with the structure borne vibration transfer via the mounting points of the transmission to the car-body. Vibration of the housing directly transforming into airborne noise is out of scope of this thesis.

Frequency range: In this thesis, the focus is to minimize the structure borne transfer of gear-whine particularly in the frequencies of 1000 - 5000 Hz. Due to lightweight design,

thinner and lighter gears have natural frequencies in the order of a few kHz [102, 138]. When the gear mesh frequency coincides with the resonance of either of the elements in the transfer path, the noise can be amplified finally in the passenger cabin as interior noise. The noise in this frequency range is particularly sensitive to the human ear. The threshold for perception of sound in human ear is reduced particularly in the frequency range of 2000 - 6000 Hz [25], i.e. the ears are more sensitive to noise occurring in this frequency range.

Test-rig mechanical design: To study the system requirements and the transfer path of the gearbox vibration mechanism, an experimental test-setup was constructed in the early phase of the project. The specifics of the construction can be found in [105] and is not addressed in this work. This test-rig served as a pre-cursor study to establish the actuator force requirements. In regards to the extent of transfer path of the structure borne vibration at mounting points, the specific mount design and car compartment dynamics are unknown. This is because these components are usually customised according to OEMs. Hence system is restricted to the mounting points of the gearbox.

Electrical design of actuator: For the actuator design, the derivation of the force requirements is obtained from the developed model of the gearbox described in Chapter 3. The selection of actuating principle, the power requirement optimisation and design (both electrical and mechanical) are not in the scope of this work. This is performed in collaboration with another researcher within the LIVE-I Project [103]. Only the actuator force requirements and post-design evaluation of concept i.e. actuator placement and vibration control capability have been addressed in this work.

1.3 Introduction to the gearboxes

In this work, two sets of gearboxes are studied. One is a simplified version of a Dual Clutch Transmission (DCT) with seven speeds from Magna Powertrain: 7DCT300 gearbox, henceforth referred to as **prototyping gearbox**. It is designed retaining only the loaded 3rd gear pair and the final drive along with the complex housing. The gear pair is excited with a dynamic torque through a piezoelectric exciter shown in Figure 1.6. More detailed description of the construction of the gearbox is given in [105]. The features to note are the free - free boundary conditions imposed by suspending the gearbox from a rigid frame shown in Figure 1.4. This is done to study the modes of the gearbox housing without any external structure influence. The main purpose of having this simplified prototyping gearbox in this study is to establish the modelling and active vibration control design procedures. The aim is to study the transfer paths in a complex geometry housing using a rather simplified excitation to design and validate an appropriate active vibration control system, before they can be extended to real transmission scenarios.

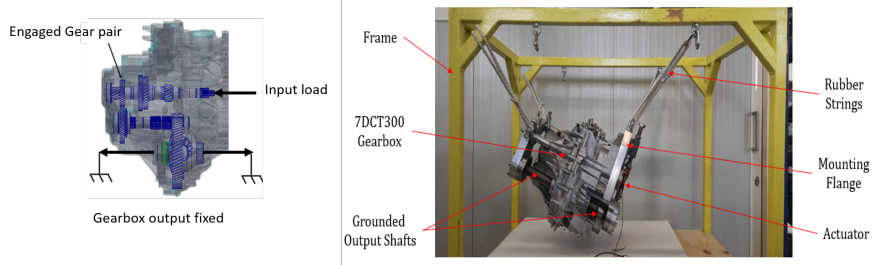


Figure 1.4: Testing prototype of the 7DCT300 gearbox [105]

The second gearbox is a hybridised version of the 7DCT300 known as 7HDT300 [18] henceforth referred to as **demonstration gearbox**. It is a series production transmission, which retains the complete 7-speed gears along with the reverse gear and final drive. The transmission also consists of an electric motor which is not used for the tests in this study. The demonstration gearbox is used for extending and validating the developed AVC system for commercial applications in a realistic rotating scenario on the IMS Connect test-bench [62]. The test bench is depicted in Figure 1.5. The output of the final drive is connected to two identical asynchronous load motors. Each of them is separately capable of a maximum power of 160 kW (maximum 2000 Nm rated torque). On the drive side, one synchronous motor with a maximum power of 240 kW (maximum 500 Nm rated torque) drives the input shafts. The test bench is automated with PUMA Open 2 Software from AVL [12] to realise different test-cycles under various operating conditions and speeds.

Similarities between gearboxes

The gear train present in both the gearboxes is identical, i.e. all seven speed stages have the same number of gear teeth and shaft distances. The only difference is the consideration of the gear-pair in isolation for prototyping purposes of the AVC system in the prototype gearbox set-up. The gearbox housing consists of two cases (enclosure halves) - clutch case (in blue) and transverse case (in grey) as seen in Figure 1.6. The clutch case rigidly attaches to the engine. This condition is depicted by the rigid plate of the Prototyping gearbox. In the demonstration gearbox, the clutch case attaches to the engine plate on the drive motor side on the Connect test bench as indicated in Figure 1.5.



Figure 1.5: Test bench for validating Active vibration control using HDT300

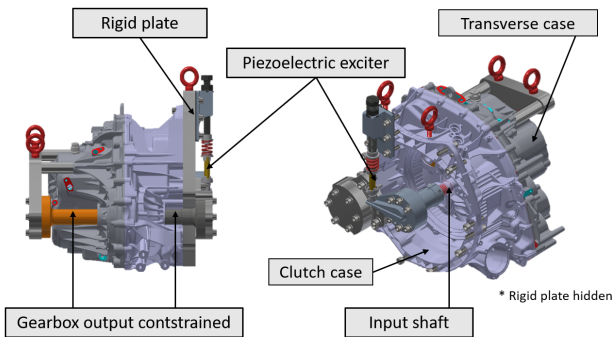


Figure 1.6: Model of the gearbox showing the piezoelectric primary exciter. Detailed operation of the gearbox operation is presented in [105] and Chapter 3

1.4 Research questions

The thesis aims to systematically answer the following research questions (RQ) related to the key elements in development of an AVC system.

1. **RQ 1: Modelling approach:** With what level of accuracy can a model predict the high frequency vibration caused by gear whine? What is the accepted level of model fidelity vs modelling effort for making the system-level decisions for development of active vibration control?

2. **RQ 2: Actuator force requirement:** How much external force needs to be applied to the gearbox housing to minimize the vibration transfer at the mounting points?
3. **RQ 3: Alternate sensing approach:** Can a reliable high-frequency bandwidth sensing architecture be designed? This decision is based on economical vs impact on a system level basis. How can a Data Acquisition (DAQ) system, that can be easily integrated into the existing automotive electronic architecture be developed using low cost hardware? How can this alternative sensing be calibrated with existing industrial standard sensors?
4. **RQ 4: Actuator position:** Where should the actuator be placed on the transmission housing to provide sufficient controllability at all the mounting points? What type of optimal placement strategies can be devised? What is the appropriate number of discrete point actuators required to minimize the vibration?
5. **RQ 5: Control algorithm:** Can a suitable multi-point control algorithm (due to the need for control of multiple mounting points) be implemented on the developed for high-frequency vibrations that can be deployed limited computational hardware?
6. **RQ 6: Economics:** What is the cost, weight and energy consumption of the active vibration reduction system are opposed to the demonstrated benefits?

1.5 Structure of thesis

Each chapter deals with important steps of development of the mechatronic system as illustrated in Figure 1.7. The blue-highlighted arrows indicate the flow of finalised results from one subsystem to another.

To begin with, a systematic review of each subsystem is performed in Chapter 2. Drawing from the review of the existing literature, relevant concepts and tools to design and develop each of the subsystems are decided.

In Chapter 3 the dynamic properties of the system is evaluated by developing a model to predict housing vibrations. The validity of analysis tools to predict high-frequency vibrations in a complex structure like the transmission housing is evaluated. Two separate models are developed, one to derive the actuator force requirement that answers RQ 2 and the second to simulate the dynamic behaviour of the gearbox in response to realistic excitation. A correlation with relevant tests is also provided.

Chapter 4 deals with the development of an alternate sensing system and particularly answers RQ 3. One of the main research objectives is to develop a high frequency bandwidth, reliable sensing architecture. This chapter begins with the introduction of Macro-Fiber Composites (MFCs) and a relevant signal conditioning system to measure high frequency vibrations. A systematic calibration procedure is adopted to use MFCs as a reliable replacement to traditional vibration measuring sensors such as accelerometers.

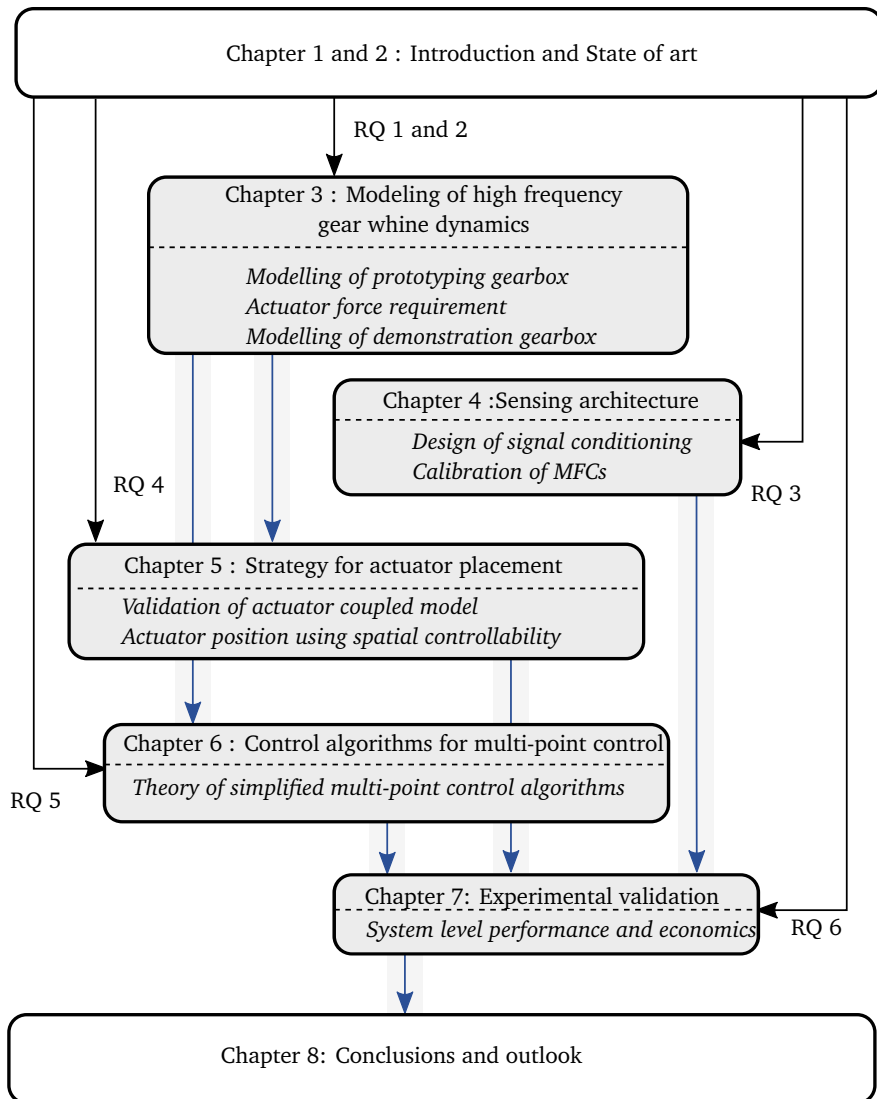


Figure 1.7: Overall structure of thesis

The chapter concludes with the design of the DAQ board that is used in deploying the AVC for experimental investigations.

Upon deciding the actuation principle, a piezoelectric inertial mass actuator is designed described in the work executed in close collaboration within the LIVE-I project [104]. The objective of Chapter 5 to place the actuator based on desired control objectives and controllability of the actuator at all mounting points of the transmission. The first part of the chapter deals with the correlation of the actuator transfer function upon coupling with the gearbox model under real operating conditions. Once this is derived, the logic of spatial and modal controllability is applied to the transfer functions derived using this coupled model. The scores derived from this assessment are used as measures to decide the actuator position.

RQ 5 is dealt with in Chapter 6 where a suitable control algorithm is derived. The chapter deals with the comparison of four different multi-point control variations of the state of art Filtered-x Least Mean Square (FxLMS) algorithm. The first three algorithms namely the Single Output Multi-Output (SIMO), mixed-error and switched-error FxLMS are applied directly from the status quo to the current problem at hand.

In Chapter 7, the proposed control algorithms are validated along with the entire AVC system developed using results from the previous chapters. Using the key aspects from the three algorithms, a Projected FxLMS algorithm is proposed. This algorithm leverages the information of other mounting points from the model and also represents potential sensor number reduction for economical industrial deployment of the AVC system. Recommendations for complete deployment and integration of the system for industrial use are proposed. Economic aspects and weight implications of the add-on system for lightweight transmissions are also discussed.

2 State of the art

Before proceeding with the design of active vibration control for transmissions, it is important to understand the research gaps in the state of the art with respect to the research questions raised in Chapter 1 and develop strategies to address them systematically. The review of relevant concepts and literature is organised sequentially according to each of the subsystems presented in Figure 1.3. A system level review of active vibration control systems is performed, followed by a review of modelling approaches. Of interest here are the methods specifically used to model high frequency ($> 500\text{ Hz}$ to kHz range) with sufficient numerical accuracy and ease of modelling to build a system-level model which are presented in Section 2.3. Additionally, a review of alternative sensing approaches relevant to high frequency vibrations is presented in Section 2.4 with a focus on cost and reliability of measurement. Although the actuator design is outside the scope of this work, its placement is one of the important objectives that is reviewed in Section 2.5.1. A short overview of hardware used to implement the active vibration control system is also presented in Section 2.6 which leads to selection of appropriate hardware for design of the AVC system. Finally, Section 2.7 provides an important overview of the various control algorithms employed in AVC systems, specifically dealing with multi-objective control.

2.1 Vibration behaviour of gearbox housings

The nature of primary excitation in gearbox caused by transmission error is tonal in nature with spectrum of vibration of the gearbox housing operating at steady state speed containing mainly the gear mesh frequencies and their harmonics. For lightweight transmissions, housings have been optimised by reducing the thickness of walls [61, 129, 139] or using lightweight and alternative materials [4, 114, 144]. Lighter housings eventually have larger flexibility, which has a direct impact on the dynamic behaviour of the transmission system leading to increased vibrations.

Vibration in housing structures due to the gear-mesh is transmitted via the bearings through structural waves usually occurring in two types [57]. One of these two types are flexural or bending waves, which are responsible for radiating noise from the structures walls. Second kind are longitudinal or compression waves. At the boundary conditions, these waves are reflected and transmitted to further connecting structures making them the main mode of structure borne vibrations. Of importance in the study of structure-borne vibration transfer in automotive transmission, in the form of longitudinal waves. Mounting points serve as paths for structure borne vibration transfer into the attached part, in this case the chassis and passenger cabin. The vibration in these structures will



propagate eventually into noise. At higher operating speeds, the tonal gear-whine can rise up to the order of several kHz, hence affecting passenger comfort. Mounting brackets are studied in literature independently [87, 88].

In the subsequent sections of this chapter, a review of modelling and active vibration control techniques employed for high frequency gearbox housings is presented.

2.2 General overview of active vibration control

Conventional passive vibration control systems often employ dampers, which involves mounting the gearbox on standard rubber supports and incorporating a substantial mass damper to mitigate high frequency vibrations [3]. The vibration behaviour of the gear mesh is also greatly influenced by compliance of the gearbox housing which alters significantly in the process of lightweight design with geometry and material changes. Therefore this was countered by inclusion of ribs as stiffeners [131] which is also passive model of vibration control. This often only is a solution tuned for a specific frequency. Adaptive passive solutions and semi-active have also been demonstrated using shunted inertial actuators [145].

Several studies use housing vibration as the end goal to design active vibration control solutions for gearbox housings. Early studies in the 1990s included developing actuators for targeting the gear whine vibrations right at the source. For example, Rebecchi et al. [111], proposed magnetostrictive actuators inside the into a double row bearing, which was mounted on the input shaft next to the input pinion to reduce the mounting point vibrations. Additional supports to the shaft was also proposed inside the gearbox to mitigate the vibration transfer to the housing [52]. Until recent times, the ongoing research for example [89] still uses the housing vibration measured by an accelerometer to evaluate the effectiveness of a magnetic bearing.

Active vibration control techniques particularly at the housing are reported in literature proposing the usage of piezoelectric patches [123] directly on the housing surfaces. However it was not experimentally verified. The use of active mounts has also been demonstrated [10, 84]. A full comparison of four actuator concepts at various points in the vibration transfer path was studied [53], where actuator was mounted at gear, shaft and bearing respectively. The end goal in all the four proposed concepts was to suppress housing vibration. The main outcome was that when the actuator was an active bearing, smallest dynamic actuation force above 500 Hz was required to achieve vibration reduction at the housing.

Even though passive solutions are conventionally used for high frequency vibrations, active solutions on the other hand provide adaptability to in the frequency range of the occurrence of gear whine. Studies on high frequency gearbox vibrations began as early as 1994 with Montague et al. [96], to control vibrations on a gearbox housing at 4500 Hz using a single piezo-actuator transmitting force directly to the shaft. In a recent study, inertial mass actuators were developed to control vibrations at the bearing housing also



at frequency range above 4500 Hz [140]. The concept was also experimentally validated, where the AVC was implemented with model-free approaches.

As it can be seen that most of the studies use housing and /or mounting point vibrations as the evaluation metric for the specific active solution proposed, the direct active treatment of the gearbox housing is absent. The status quo collectively demonstrate a prominent focus on using gearbox mounting points and housing vibrations as key targets for active vibration control. There is a prominent need for addressing vibrations at these critical interfaces to the supporting structure. For the automotive transmissions, this means minimizing the impact of gearbox vibrations on overall system performance and user comfort. Developing an active control concept where the actuator could be directly mounted on the housing could also reduce the actuator force requirement, hence leading to a low power and economical system.

2.3 Modelling of high frequency dynamics of gearbox vibrations

It is clear that the effect of compliance of the housing cannot be neglected in studying the vibration characteristics of structure-borne vibration transfer in gearboxes. The aim of this study is to establish an active solution for the transmission housing, where the possible actuator is "added-on" to the housing structure. It is important to model the vibrations getting transferred to the housing, which is done by modelling the gear train and the self-excited gear whine. This is followed by an appropriate modelling technique to capture the high frequency vibrations on the gearbox housing.

Although, argued previously that an accurate model of the gearbox vibrations for high frequency excitations is extremely difficult to achieve [140], the aim in this thesis is to check the limitations of existing computational tools in doing so. Also, this model would help to obtain the force requirements for the selection and design of an appropriate actuator. The model would be useful in determining the actuator position. Gearbox numerical simulations are becoming more popular as the computation power increases as well as numerical methods are improved. Simulations can be used to verify system-level vibration analysis with flexible mechanical components and are also essential to shorten product development cycle.

2.3.1 Modelling of gear-trains

Three different levels of model fidelities of gearbox models are reported literature, which are described in increasing level of complexity in Table 2.1 into three categories: standard, analytical and advanced modelling techniques.

In most standard models, the lumped-mass approach is used, where each element of the gear train is considered as one Degree of Freedom (DOF) [51]. The housing is not included in most of the standard models. The main assumption is that the outer rings of the bearings are rigidly fixed (to ground). The main excitation in the gear-whine phenomenon which is

Table 2.1: Model fidelity levels of gearbox modelling

	Model fidelity	Behaviour of model evaluated	Stiffness of total model	Gear stiffness calculation	Micro-geometry inclusion
1.	Standard	Global	Constant	ISO 6336-1	No
2.	Analytical	Global	Load dependent	ISO 6336-1	Yes
3. Advanced					
3.1.	Advanced Empirical	Local	Non-linear	Discrete curves	Yes
3.2.	Advanced FE	Local	Load dependent	FE-based	Yes

the transmission error is modelled as a force multiplied with the gear mesh stiffness. This mesh stiffness is assumed to be constant and is generally calculated using the ISO-6336-1 [24]. This excitation is applied at the gear mesh along the Line of Action (LOA). The goal of these models is to have a global transmission stiffness. Standard models are easy and can be solved with less computational resources and time.

Analytical models follow the same approach as the standard models, the only difference lies in the stiffness and contact analysis formulation. A load-dependent formulation of the ISO-6336-1 is used. Coulomb friction is also accounted for in the calculations [31]. The contact model takes the bending of the tooth into account. The bearing stiffness are still considered to be linear. The shaft is also a lumped mass at this stage. Model of the housing is neglected at this stage. However without accounting for it, there is little benefit in defining micro-geometry, or using mesh misalignment results, as they will change with the housing deflections. Some studies also include the housing as a super-element, just to account for its stiffness in the overall dynamic behaviour prediction of the gearbox [73].

The modelling of gearboxes can also be with increased fidelity considering the components in much detail using Finite Element (FE) methods. In FE models, a continuous vibrating structure is discretized into numerous vibrating degrees of freedom, typically shell and solid elements. The finite element model helps to capture the complexities of a realistic gearbox. In the advanced empirical formulation, the non linearities are accounted for on a case to case basis. For each operation condition (input load and speed), the load dependent transmission error, bearing stiffness and mesh stiffness are used for further vibration analysis. The shafts are modelled as Timoshenko beam elements. The inclusion of housing is also possible at this stage using a meshed model and connecting them at the bearing points. This method is crucial for system-level simulation of gears where the load-dependent tooth bending and non-linear stiffening cannot be neglected.

A higher-level of model fidelity can be achieved by converting every single element in

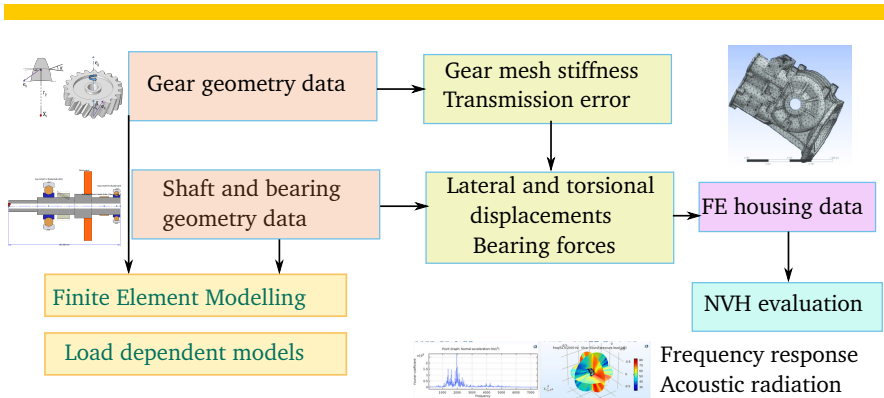


Figure 2.1: General simulation approach for gearbox NVH analysis used by commercial software

the gear train including gears, shafts and bearings into finite elements. The housing is already discretized as in the empirical model. The coupling of FE based tooth stiffness accounting for detailed analysis of gear body deflections is important in the design of lightweight gears. With FE discretization, each node is considered as an individual degree of freedom. The computational complexity of this advanced FE model is very high, and it usually takes about hours to solve. The models of this fidelity are usually implemented with Model Order Reduction (MOR) techniques, which have been reviewed in Section 2.3.2. Including the micro-geometry features for the gear mesh stiffness calculation would be as good as determining from FE calculations considering the actual gear body and relevant contact formulation [46]. This technique is employed in most of the commercial software packages. There exist a variety of commercial software to model gearboxes and their NVH performance which are presented in Table 2.2. These software are compared in the next section and evaluated for a reasonable model fidelity that would be sufficient to achieve the goals for the AVC system design.

Software packages for NVH modelling of gearboxes

A review of commercially available software packages that can simulate the NVH behaviour of transmissions is presented, taking into account all relevant components. Almost all of the software follow a general solution approach to vibration analysis of transmissions shown in Figure 2.1. Depending on the level of model fidelity that needs to be achieved, these packages offer a variety of solutions such as selection of solver for gear mesh stiffness calculation, conversion of elements into FE models and inclusion of housing dynamics.

In software such as Romax, Simcenter 3D, FE models, the design integration is seamless.

Table 2.2: Commercial software packages for gearbox NVH simulations

Feature	ROMAX	AV Excite	KISSsoft	MASTA	Simcenter 3D
Model fidelity	Advanced FE	Analytical	Standard	Advanced FE	Advanced with multiphysics analysis
Design Integration	High external	Low internal	Low internal	Low internal	High external
Acoustic Analysis	Yes	Yes	Basic	Yes advanced	Yes advanced
Optimization option	Yes	Yes includes tuning	Limited	Yes	Yes

Models can be imported from traditional FE packages like ANSYS and Abaqus, which can still be used to study the complex dynamic behaviour of gearbox housings [115]. It is also possible to model in the other way round, where the bearing forces can be imported into standard FE packages to study the dynamic properties of the housing in more detailed.

An important feature of the NVH analysis to note here is that none of these software packages provide a transient-behaviour analysis, i.e. deeper kinematic considerations are not possible. This means, one cannot replicate the time-domain related measurement that would be acquired in an experimental environment. Rather, only a frequency domain analysis can be established. To obtain time-domain response analysis, the model can be taken to multi-body transient analysis such as ADAMS, Abaqus and ANSYS transient which are computationally exhaustive. Or as an alternative, they can be linearised as a state-space model and analysed in MATLAB which is computationally efficient.

Some studies also have demonstrated a co-simulation on the system level model in MATLAB [132]. This is essential for designing the control strategies and inclusion of actuator models. This is offered in Romax with MSC Cosim and MATLAB as well.

Since the housing is of great importance, the gear train is modelled with advanced empirical model fidelity. Load-dependent gear tooth contact and bearing stiffness are included to model the gear mesh excitations that are transmitted to the housing. ROMAX was used in this work to model the dynamics of an operational automotive transmission. The next section provides a brief overview of the gearbox housing models, with a special

focus on capturing high-frequency dynamics.

2.3.2 Modelling of gearbox housing

For modelling the transmitted vibration from the gear train to the housing, sophisticated methods FE methods need to be employed especially for complicated geometries like automotive transmissions. Particularly in the case of frequency range of a few kHz range, the wavelengths of vibrations are of the order of a few millimetres to micrometers. In some papers where the description for frequency range 500Hz -5000 Hz is also categorised as "mid frequency range" [64]. Apart from Finite Element Methods, Boundary Element Methods (BEM) are also used [60, 74, 79]. To counteract the disadvantage of high computational complexity of FE models, BE method reduces the problem to solving only the boundaries of the domain, making it more efficient for problems where only the surface interactions are of primary interest.

Another alternative in the high frequency modelling of structural vibration is the Statistical Energy Analysis (SEA) [85]. This is a common method for analysing structures for acoustics and noise emissions [116]. The main modelling principle is the transfer of energy between these subsystems which represent each mode type. Like any other form of energy transfer, losses are accounted for using coupling loss factor and internal loss factor. The method is rather complicated for complex geometries like an automotive gearbox and is traditionally used for acoustics rather than structural vibrations.

Long-wavelength deformations tend to behave "deterministically" whereas the short-wavelength ones behave "randomly" [76]. The main difference between both methods is that FE methods are deterministic while SEA is probabilistic. The frequency range of interest for the FE study is 1000 - 5000 Hz which is usually characterised as mid frequency range or high frequency range in some studies where both FE and SEA methods could be applied. There are multiple studies performed in this domain using hybrid FE and SEA methods [64, 76]. In the review paper comparing FEM methods with SEA methods [32], it is concluded that for addressing structure-borne sound transmission issues, deterministic methods tend to be more effective, whereas statistical approaches are primarily employed when dealing with air-borne sound transmission problems.

Hence in this thesis work, the FE method is used to obtain the dynamic behaviour of the housing with reasonable accuracy. Several FE packages are available to generate the discretized model of the gearbox housing, for example ANSYS, Abaqus etc. Due to availability of academic license, ANSYS was chosen for this study.

Two main classes of models that are used to represent FE models are the nodal and modal form. In nodal form, each of the equations are written in terms of each of the physical discretized points in the geometry and are characterized by mass and stiffness. Modal models are characterised by the eigen characteristics (natural frequencies and mode shapes). The modal models, the mass and stiffness matrices are diagonalised, making it computationally easier. In the original formulation from FE, the size of modal and nodal models are the same, just the representation is interchangeable. Model reduction



techniques need to be employed for generating usable models for assessing the structural dynamics in a more computationally easier way.

Model reduction techniques

For large FE models, large number of nodes exists which directly translate to large number of differential equations that need to be solved. Hence, a lower-order approximation is needed which can still retain the behaviour the original formulation with certain degree of accuracy that can be correlated with tests. Computationally efficient models that are able to reproduce experimental behaviour should be the focus of any reduced order modelling.

For structural dynamics, the goal is to have a model that is able to capture the eigen frequencies and dynamic response of the system to a sufficient accuracy. Component Mode Synthesis (CMS) [27] is the most commonly used model order reduction technique. This method involves selecting the important /significant vibration modes and retaining this for further dynamic analysis. As described in Section 2.3.2, nodal models are easily able to achieve this. The unnecessary modes and associated mode shapes are not considered for further analysis hence reducing the model order. In CMS method, the Degrees of Freedom are separated into interface and internal DOFs. The interface DOFs are retained and reduction is performed on the internal ones. CMS Methods have been in usage since the 1960s and are widely used in commercial Finite Element packages, making them an industry standard practical for engineering applications.

In the work of Janssen et al. [63] provide a modular approach for selecting important eigen modes using a relative mode importance measure. The system is divided into the component level (also known as sub-structuring), before combining them into an overall assembly. Model order is reduced on each of the individual components and then combined on a system level. In the case of a gearbox, this would mean separating the source of vibration, i.e. the gear-train and the receiver, the housing.

Another class of model reduction techniques in structural dynamics are the Krylov subspace methods which often lead to much smaller models than modal truncation methods [13]. The focus is to retain the input-output behaviour of the system with reduced degrees of freedom. Variation of this method include the Lancos [117] and Arnoldi algorithms [1].

For design of efficient control systems, usually the balanced reduction is recommended [7]. The balanced reduction is a two step process - first realisation of a balanced and then the reduction is performed using Hankel singular values. The balanced model order reduction generally offers excellent accuracy with the added benefit of error bounds and stability preservation.

Besselink et al. [14], provide a detailed comparison of various model order reduction for two different end goals - namely structural dynamics and control design. As a comparison of model order reduction techniques of both the end goals, it was reported that the balanced reduction is more computationally intensive than the CMS method.



In this thesis, the main focus is to have a model which can predict the dynamic behaviour of the model with reasonable accuracy. This is useful in identifying the actuator force and position, hence having a good correlation of the input-output structural dynamic behaviour is of greater importance. Design of feedback control is not the main focus and this is reviewed in more detail in Section 2.7. Although the reduced order model is represented in state-space (Linear Time Invariant - LTI) form, to generate a suitable control strategy. Hence, the model order reduction based on FE and CMS is adopted.

2.4 Review of sensors and actuators

2.4.1 Sensing

Traditionally there are multiple sensor concepts for vibration measurement. When a structure is subject to vibrating loads, the surface undergoes cyclic local deformation. Vibration can be quantified with these local deformations using displacement and strain sensors. Velocity of the vibrating surface is usually characterised by laser vibrometers. The most common way to characterise vibration is to use accelerometers.

Among accelerometers, the ones that use piezoelectric elements are part of standard industry practice of vibration measurement and condition monitoring. Piezoelectric materials generate charges due to deformation. The measure of acceleration is always scaled to the square of frequency. At high frequencies, displacements become very small and harder to measure accurately with displacement sensors, due small local displacements at high frequencies. Hence, the measurement with accelerometer provides a better measurable quantity.

Accelerometers usually can operate from 2 to 5000 Hz and can sense vibrations in all three axes (tri-axial). The main problem with using sophisticated sensors such as accelerometers to integrate in the current active vibration control system is the cost and mass-loading effects. For example, for the validation of the demonstration gearbox, PCB356A16 accelerometers were used. These accelerometers are tri-axial and directly produce voltage corresponding to the vibration sensed. This principle is referred to as ICP (Integrated Circuit Piezoelectric) and often comes with an expensive add-on signal acquisition hardware that has inbuilt electronics to power the integrated charge amplifier in the sensor. Typical cost for such accelerometer lies in the range of 100 - 200€ per piece and requires dedicated signal acquisition instrumentation and real-time data acquisition that has an add-on cost of its own.

This is why a cost-effective sensor with simple integration capabilities was essential. In studies several economic alternatives to piezoelectric accelerometers can be found. For example capacitive MEMS accelerometers, piezoresistive accelerometers and polymeric piezoelectric accelerometers. MEMS capacitive accelerometers are lightweight, cost-effective, and suitable for low-frequency measurements but have limited bandwidth and sensitivity to temperature. Piezoresistive accelerometers offer a wide bandwidth and can measure static acceleration but are more expensive and temperature-sensitive.

Piezoelectric accelerometers excel in high-frequency response and sensitivity but cannot measure static acceleration and require a charge amplifier. Polymeric accelerometers are flexible and potentially low-cost but have lower sensitivity and limited frequency range. Selecting an accelerometer involves a fundamental trade-off between size and sensitivity. Compact accelerometers offer several advantages: they are easier to deploy, capable of detecting higher frequency vibrations, and minimize mass loading effects on the structure being measured. However, their diminutive size comes at the cost of reduced sensitivity.

Polyvinylidene Fluoride (PVDF) film-based piezoelectric sensors offer a cost-effective alternative to crystal-based accelerometers for vibration measurement. These sensors detect local displacements of vibrating structures. Vibration can also be quantified through strain measurement, as vibrating structures experience cyclic surface strains. Two main types of strain sensors are used for this purpose: conventional resistive strain gauges and PVDF film sensors. Another emerging technology in the field of sensing and actuating technologies, are smart composites comprising of alternating layers of piezoelectric matrix and metallic electrodes. Macro-fiber Composites (MFCs) acts as a sensitive yet effective strain sensor. MFCs measure strain proportional in contrast to accelerometers that measure the strain multiplied by the square of the frequency. Currently MFCs are widely used as acoustic emission sensors [42]. Many studies have used MFCs for vibration detection [35, 121] for structural health monitoring using impedance based monitoring and lamb wave detection [90]. A brief overview of the construction of strain sensors is shown in Figure 2.2.

It is interesting to note how the difference in construction of piezoelectric materials in PVDF and MFCs can differ in measuring vibration of structures. Sohn et al. [122] investigated both the PVDF and MFC sensing principles on an aluminium plate under sine sweep excitation in the frequency range 0 - 5000 Hz . The outcome of this study is important to this thesis as the frequency of interest coincides. It was concluded that PVDF and MFC have comparable sensitivities and vibration measurement capabilities. So the only deciding factor for the use in the active vibration control system being developed in this thesis would be the cost.

The actuating capabilities of MFCs are also reported in literature [80], but they are generally suitable for thin beams and plates and most importantly in energy harvesting applications.

2.4.2 Actuation

In some studies, the actuator design and its placement are undertaken simultaneously [36, 38]. In this thesis, the scope is to derive actuator force requirements rather than the design itself. This has been usually done in past research through simulation techniques [43, 72] for other dynamic systems such as beams and machine tools, but can be easily extended to gearbox system. Li et al. [81] demonstrated the derivation of piezoelectric stack requirements for gearbox.

It is very important to consider the coupled nature of actuator dynamics with the

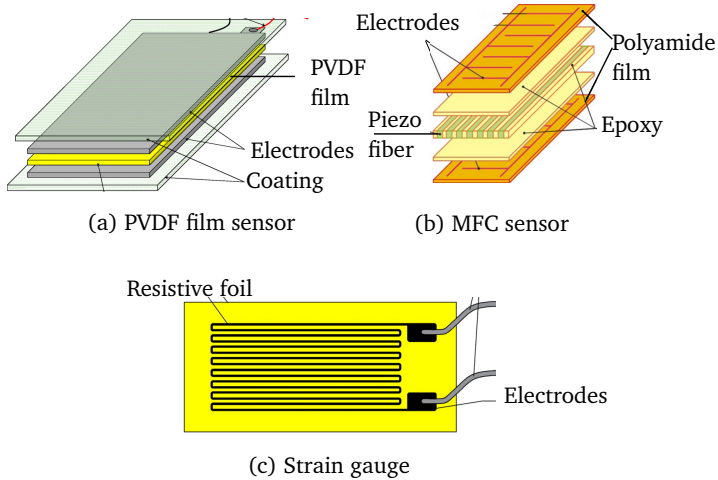


Figure 2.2: Construction of three film shaped sensors, (a) PVDF film sensor (b) MFC and (c) Strain gauge

structure that is needed to be controlled [148]. The coupling of the dynamics of the actuators alter the nature of the effect the externally provided actuator has on the targeted point to be controlled.

2.5 Review of actuator placement techniques

The performance of AVC not only depends upon the control law but also on the placement of piezoelectric sensors and actuators. To understand the further concepts in the controller and actuator position the definition of secondary path transfer function is introduced. The transfer path of force from a control actuator aptly positioned on the gearbox housing to reduce the vibrations at targeted locations on the gearbox housing is called the secondary path. Both the control algorithm and the actuator position depend upon the nature of the secondary path transfer function. Control algorithm mostly depends on the phase of the secondary path transfer function, while the actuator position is determined by the magnitude of the transfer function.

From control design standpoint, it is advantageous to collocate the actuator and sensor, i.e. to position them at same location or close enough that they lie in the same side of a mode shape [110]. This ensures stability in the control loop. In real operating conditions, perfect collocation cannot be achieved due to several design constraints. The secondary path transfer functions are very position sensitive at frequencies, and have mode shapes

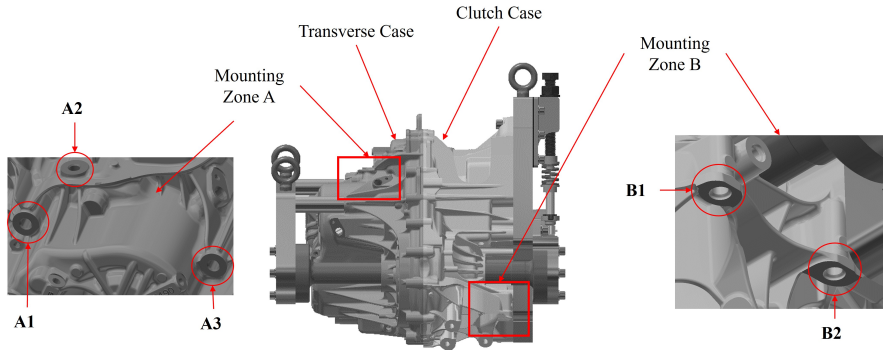


Figure 2.3: Multiple mounting points on prototype gearbox used in this thesis

with small wavelengths. This causes the vibration characteristics to change even with a minor variation in actuator position. In addition, in an automotive gearbox, there are multiple mounting locations (shown in Figure 2.3) making it a financial decision to optimise the number of actuators used in the final active vibration control solution.

In some studies, placement of the actuator and the optimal controller design are dealt with simultaneously in the works of Haase [55], Zhu et al. [147] and Hiramoto [34, 59]. The main optimization is the placement of actuator and the control parameter optimization is embedded in the main optimization problem as a sub-routine. This is usually done when a feedback controller needs to be designed to derive the optimal feedback gains. For feedforward control, no literature on inclusion of controller with the actuator positioning has been reported in literature. Another approach is to treat the problem of actuator independently from the controller design. After a suitable actuator layout is derived, a variety of control algorithms can be explored to deploy on the system. In this thesis, the latter approach is adopted. First the position and number of actuators is derived and then a suitable control algorithm is applied to the system to minimize the vibrations.

The optimal placement of actuators for active vibration control depends on the optimization criterion. The boundary conditions must be properly understood for the problem before establishing an optimization criterion. In general linear time invariant systems, the effectiveness of an actuator is judged by the measure of controllability. The most common criteria for optimizing the actuator position is to maximise its controllability. This means that the actuator is positioned at a location where the magnitude of the secondary path transfer function for a particular frequency of control is high. This intrinsically minimizes the control effort or energy required by the actuator. For a flexible dynamic system represented by a state-space model with matrices \mathbf{A} , \mathbf{B} , \mathbf{C} and \mathbf{D} , the controllability

matrix is given by :

$$\mathcal{C} = [\mathbf{B} \quad | \quad \mathbf{AB} \quad | \quad \mathbf{A}^2\mathbf{B} \quad \dots \quad | \quad \mathbf{A}^{N-1}\mathbf{B}] \quad (2.1)$$

where N is the dimension of the state matrix \mathbf{A} equal to the number of states modelled in the system. The qualitative measure of controllability is given by the rank of the matrix in Equation 2.2. The system is controllable only if the matrix has a full rank of N . The major drawback of controllability is that it is a qualitative measure. It only gives an insight if an actuator placement point in the system is controllable or not. It is also not possible to compare multiple actuator arrangement points against one another just using the controllability matrix. Analogous to the controllability matrix, the quantitative measure of controllability is derived by its Grammian which is given by :

$$W_c = \int_0^{\infty} e^{\mathbf{A}t} \mathbf{B} \mathbf{B}^T e^{\mathbf{A}^T t} dt \quad (2.2)$$

A system is controllable if W_c is positive definite. Diagonal elements of W_c represent the energy going into the modal states. The aim would be to maximise the Grammian norm or to maximise the trace of W_c so that minimal control effort is needed to generate maximum output. Similar to the controllability matrix and its Grammian, the observability matrix and its Grammian is constructed using the \mathbf{A} and \mathbf{C} matrices. The observability counterparts are used for sensor location optimisation. In this work, the position of sensors is fixed at the mounting points and hence this is not discussed.

The controllability Grammian/measure is valid only for a small number of modes, in the order of 10s. But as the number of modes increase for example in a complicated geometry, even with reduced order model would be of order ~ 1000 . The controllability Grammian would be undefined due to the term \mathbf{A}^{N-1} . Hence, a proper criterion for a the actuator position needs to be established keeping in mind the high frequency dynamics and modal density.

Actuator placement problem has two aspects: selection of a proper optimization criterion and then employing a suitable optimization technique (or search algorithm) to obtain the desired actuator locations. Hence, the review of this section is dealt in two parts: first an overview of all the optimization criteria applied to vibration control problems and then a review of all the optimization algorithms used is presented.

2.5.1 Review of optimization criteria for actuator placement

A summary of the different optimization criteria used in actuator placement strategies is presented in Table 2.3.

Table 2.3: Common criteria used in actuator location optimization [54]

Criteria maximised	Criteria minimised
Degree of controllability	Spillover
Control force applied by actuator	Control effort (power) of actuator
Deflection of host structure	

Year	Author	Placement criteria	Optimization technique	Dynamic system
1993	Hać and Liu [56]	PI based on energy in mode	Continuous	Simply supported beam & plate
1993	Maghami and Joshi [86]	Hankel singular values & Pole modification	Non-linear programming	
1997	Lim [82]	Hankel singular values	Discrete search	Generic system
1997	Gawronski [50]	Hankel singular values	Discrete search	Truss
2000	Bin et al. [16]	Maximise modal force	Discrete search	Plate
2000	Hiramoto et al. [59]	\mathcal{H}_2 - norm	Gradient descent	Beam
2002	Zhu et al. [147]	Maximise modal force	Topology optimization	Plate
2003	Kessissoglou et al. [69]	Maximise modal force	-	Plate
2004	Demetrious and Moghani [33]	\mathcal{H}_∞	Continuous	Plate
2005	Bruant [21]	Maximise control force Minimize control energy	-	Beam and Plate

2009	Bruant et al. [22]	Maximise control force Minimize control energy	Genetic algorithm	Beam and plate
2009	Dhuri and Seshu [38]	Maximise control force	Genetic algorithm	Beam
2010	Morris and Demetrious [97]	\mathcal{H}_2	Continuous	Beam
2011	Kashinathan and Morris [67]	\mathcal{H}_∞	Continuous	Beam
2012	Darivandi et al. [30]	LQ optimal	Gradient-based	Beam and plate
2012	Späh et al [124]	PI based on energy	Continuous	plate
2012	Ambrosio [5]	\mathcal{H}_2 - norm	Continuous	plate
2013	Kashinathan and Morris [68]	\mathcal{H}_∞	Continuous	Beam
2014	Summers and Lygeros [125]	Controllability	Combinatorial	Electric grid
2015	Tzoumas [130]	Controllability with minimum control effort	Combinatorial	Network structure
2015	Morris & Yang [98]	\mathcal{H}_2 vs - \mathcal{H}_∞ vs LQ vs Controllability	Continuous	Beam and plate
2015	Hasse [55]	Controllability	Genetic algorithm	Plate

Table 2.4: Literature on actuator placement problems based on traditional criteria of controllability

Table 2.5: Literature on spatial controllability applied to complex systems

Year	Author	Placement criteria	Optimization technique	Dynamic system
2006	Aramaou and Demetrious [8]	Spatial \mathcal{H}_2	Continuous	Parabolic system
2007	Demetrious [34]	Spatial \mathcal{H}_2	Continuous	Parabolic system
2015	Biglar [15]	Spatial Controllability	Genetic Algorithm	Plate
2021	Ding et al. [40]	Spatial \mathcal{H}_2 -norm	Genetic Algorithm	Plate
2017	Giovanni et al. [77]	PI based on Energy	Combinatorial-Discrete	Truss
2019	Kessler et al. [70]	Maximise Modal Force	Combinatorial-Discrete	Planetary gearbox

Until the early 2000s the Hankel singular values were used to decide the controllability of actuators. Hankel singular values are the square root of the product of diagonal elements of the controllability and observability Grammians. They are related to the energies of the system. Later the works diverged into various criteria such as maximising modal force, and the norms of the secondary path functions. In the work of Morris et al. [98] comparing \mathcal{H}_2 , \mathcal{H}_∞ and LQ approaches for a simple beam, it was concluded that, the optimal actuator locations are not related to points of maximum controllability.

The \mathcal{H}_2 -norm of the secondary path transfer functions can be used directly instead of using the controllability matrix. The \mathcal{H}_2 and \mathcal{H}_∞ norms are defined for the complex valued secondary path transfer function \hat{H} as:

$$\begin{aligned}\|\hat{H}\|_2^2 &= \frac{1}{2\pi} \int_0^\infty \text{tr}\{\hat{H}(s_1, P_1, \omega) \hat{H}^*(s_1, P_1, \omega)\} d\omega \\ \|\hat{H}\|_\infty &= \sup_\omega \|\hat{H}(s_1, P_1, \omega)\|_2\end{aligned}\tag{2.3}$$

where s_1 is the location of the target position for control, P_1 is the location of the actuator, ω is the frequency of operation. Let all the spatially distributed target control points belong to set \mathcal{B}^* . The term $\hat{H}^*(s_1, P_1, \omega)$ represents the complex conjugate. \mathcal{H}_2 -norm

gives an average measure of secondary path amplification in the given frequency range, while the \mathcal{H}_∞ norm gives the maximum possible secondary path amplification.

The \mathcal{H}_2 -norm is basically just a weighted trace of the controllability matrix [125] and can be re-written as

$$\begin{aligned}\|\hat{H}\|_2^2 &= \text{tr}\left\{\mathbf{C} \int_0^\infty e^{\mathbf{A}t} \mathbf{B} \mathbf{B}^T e^{\mathbf{A}^T t} dt \mathbf{C}^T\right\} \\ &= \text{tr}\{\mathbf{C} \mathbf{W}_c \mathbf{C}^T\}\end{aligned}\quad (2.4)$$

Spatial methods started gaining momentum in early 2000s [95] to facilitate actuator placement in large flexible structures. Large complex geometry like a gearbox housing is a spatially distributed degrees of freedom, where vibration of each point is dynamically related to another. But such a continuous system has to be dealt with discrete (point) actuators. Hence, the formulation of controllability needs to be modified to include the spatially distributed nature of the dynamic system. This is done by integrating the norms shown in Eq. 2.3 across the spatial domain of control of the structure as:

$$\begin{aligned}\|\hat{H}\|_{2,sp}^2 &= \frac{1}{2\pi} \int_{\mathcal{B}^s} \int_0^\infty \text{tr}\{\hat{H}(s_1, P_1, \omega) \hat{H}^*(s_1, P_1, \omega)\} d\omega ds \\ \|\hat{H}\|_{\infty,sp} &= \sup_{\omega} \|\hat{H}(s_1, P_1, \omega)\|_2\end{aligned}\quad (2.5)$$

Now, the integration incorporates the spatial influence of the actuator over various points on the body to be controlled. The details of the formulation tailored to the positioning of the developed actuator is presented in Chapter 5.

Another strong finding of the actuator placement literature is that most research is on simple structures like beams and plates. Kessler et al. [70] demonstrated actuator positioning on planetary gearboxes using operational modal analysis. The classical approaches of controllability are seldom used for flexible structures with complex geometry. It is also interesting to note that the problem of actuator placement is not just restricted to vibration control problems but also to problems like electric grid networks [125] or general network like systems [8, 130].

For simple structures like beam and plate, a continuous function of the placement criteria against the actuator location can be easily obtained. Hence, the position of actuator can be easily obtained. But for large complex structures, a redefinition of the placement criteria would be necessary. Custom scoring measures were also derived to compare the performance of different actuator positions from a system level, such as a performance index (PI) based on mode shapes [78].

Since actuators are the cost-determining components in the overall system, spatial influence of the actuator needs to be maximized by appropriate placement. Nevertheless, the number of actuators finally used in the system also need to be optimised. Bruant and Proslie [21] proposed a measure based on the degree of controllability which is compared for different number of actuators. The degree of controllability is a measure

constructed by the authors using relative controllability Grammian measures.

2.5.2 Review of optimization algorithms

For analytical problems, like beams and plates, the continuous functions for the placement criteria of an actuator can be derived as a function of its position. These functions can be subjected to traditional function optimization techniques. This can be observed in majority of the state of art as the object under study is always a beam or a plate [9, 56, 98].

For complex geometries, where a number of discrete actuator positions are required, detailed optimization techniques were being used. The most common optimization algorithm used is the genetic algorithm. In the case of a discrete possibility of actuator positions where a single actuator is required, a direct comparison of the user-defined criteria/indices is used. For discrete number of actuators are to be placed, the most common optimization technique used is a combinatorial optimization [70, 125] to compare different possible actuator layout with one another. As computational power is easily available, sophisticated methods using machine learning [137] and pattern search [107] started to evolve.

In Chapter 5, discrete possible points for actuator mounting is presented to simplify the problem due to the complex geometry. Then a scoring method is devised based on the spatial controllability concept that helps in comparing various actuator positions against one another. A discrete combination of actuator position is also presented.

2.6 Review of hardware for control system deployment

Typical laboratory testing for vibration control applications involves the use of real-time operating systems like Speedgoat and d-space. The motivation for this exploration is to remain close to the final outcome, i.e. to design an economical solution. But for designing an add-on active vibration control system for automotive production, a much more simple yet powerful system is required [135].

Until the early 2000s processors like DSP320C6713 Processor [71] and TM were used.

There are many option available in the market regarding the choices of controller hardware. Single board computers like Raspberry pi, microcontrollers and Field programmable gate arrays (FPGAs). A Raspberry Pi board is single board computer (SBC) is a small scale computer on a single chip. The most famous option in the market as of 2024 is the Raspberry Pi 4. Although sophisticated, implementing simple codes in an SBC can be cumbersome in comparison to a microcontroller. IT can also run a real time operating system. It has been used in active vibration control applications, but mostly for low frequency vibration with proportional controller [135]. Field-Programmable Gate Arrays (FPGAs) are advanced integrated circuits that can be customized through programming. They consist of an array of configurable logic blocks, such as AND and OR gates, which



can be interconnected as needed. FPGAs are optimized for parallel processing, offering significant speed advantages and the ability to handle multiple input/output operations simultaneously without relying on interrupts, unlike single-core microcontroller units (MCUs). This makes them ideal for complex computations and real-time data processing. FPGAs consume more power compared to microcontrollers and SBCs due to their parallel processing demands. They are complex and time consuming to develop due to customisation. FPGA programming is done via hardware description languages such as Verilog. FPGA is good for a production worthy product. This will also be discussed in the summary of this thesis where suggestions to implement a production worthy product are presented. A microcontroller can be programmed faster than an FPGA and is also cheaper. The disadvantage would be the lower speed. Several options for microcontroller development boards are available in the market - STM32 [143], Arduino, Teensy, etc. Microcontrollers offer a high level of integration, where all necessary components are present on a single chip. It is also possible to enable fast prototyping. They consume low power and are easily programmable via C++.

MCUs perform best at real-time control and data acquisition. SBCs are well suited for processing operations and running software. If the goal is to keep the cost and complexity of the system low, then using a microcontroller is the best choice. For vehicles, microcontrollers are the most used control units. FlexRay, Controller Area Network (CAN), and Local Interconnect Network (LIN) are three of the most often used vehicle communication within various control units in the vehicle. These features are offered on almost all MCU development boards, FPGAs and SBCs.

One of the requirements on electronic systems is real-time capability. This means that control procedures must react to input signals within an extremely short time which is related to the processing speeds of these hardware. Among MCU boards, Arduino has a maximum processing speed of up to a few 100 MHz. STM32 and Teensy 4.1 are both based ARM cortex M7 clocking up to 400 MHz and 600 MHz respectively, making them the fastest on the market. A summary of the benefits and decision making factors for hardware selection is shown in Figure 2.4.

For this study, the active vibration control system is realised in hardware with the help of the Teensy 4.1 microcontroller development board due to its speed and cost benefits. Although it is a high-speed microcontroller, it is also used to acquire data simultaneously along with calculation of the control output in real-time. Hence, the computational complexity of the resulting algorithm plays a crucial role.

2.7 Review of relevant control algorithms

In the case of active vibration control, where vibration is caused by a tonal disturbance such as gear whine, its frequency is correlated to input speed of the gearbox. The idea to explore here is if a feedforward controller can achieve significant vibration reduction compared to simple feedback control algorithms for dynamic system like a gearbox. This

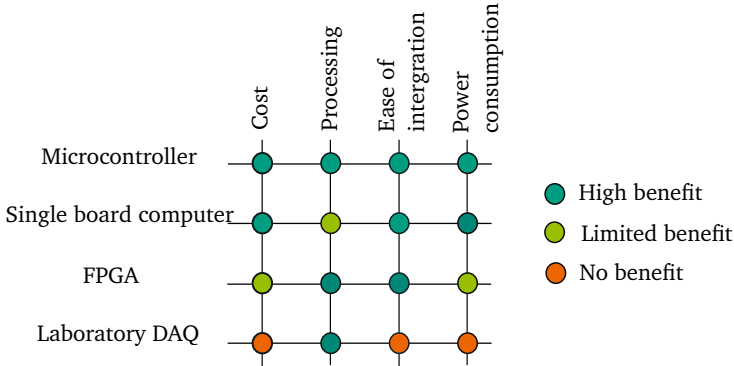


Figure 2.4: Benefits and decision making factors for vibration control electronic hardware

has been studied by Sun et al. [127], where a comparison of the PID (Proportional-Integral-Differential) algorithm with the feedforward FxLMS (filtered-Least-means squares) using co-simulations of the gearbox with control is made. The conclusion of their study is that although both algorithms effectively suppress gearbox vibrations, FxLMS is more efficient in targeting harmonic vibrations. Also in case of steady state vibrations, adaptive feedforward algorithm keeps the level of force required to cancel the vibration constant whereas the feedback would reduce the control output as the vibration reduces.

As discussed in Section 2.2, here a brief overview of control algorithms is presented. Montague et al. [96], used the phase adjusted feedforward approach by just modifying phase of the control signal to the actuator for a single frequency of 4500Hz using the identified transfer path. The amplitude was manually adjusted, hence this approach is only feedforward but not adaptive. Since this study, a lot of advancement has been achieved in the field of adaptive feedforward control using gradient descent approaches. Only applications relevant to gearboxes from the year 2010 onwards have been discussed here.

Apart from the FxLMS algorithm, several other algorithms have been explored for gearbox applications such as FxRLS [118, 126], Adaptive Fuzzy PID [133]. Although not directly applied to solving the gearbox vibration problem, many other variations of FxLMS can be found in literature like FULMS [146], Delayless FxLMS [112] and many more.

High frequency vibrations of gearboxes with model free algorithms has been dealt in the work of Zech [141]. Also in his thesis [140], Zech explored and compared various model-free algorithms such as simultaneous equations approach [47], direct search and simultaneous perturbations [65] for vibration control of planetary gearbox vibration in the range of 4500Hz. As attractive as this sounds, the usage of model-free algorithm is only beneficial when the actuator position is already fixed. The online adjustment of the phase



can be used with model free approaches due to the uncertainties relating to the phase delays at high frequencies.

The stability of FxLMS algorithm depends on the accuracy of the phase delay of the estimated secondary path [19]. The estimated phase delay and the phase delay in experiment varies due to mechanical and electrical factors such as damping and time delays in electrical circuits.

As seen in Figure 2.3, multiple mounting points need to be controlled with discretely placed actuators on the gearbox housing. Depending on the number of actuators, the objective of the control is a Multi-Input-Multi-Output (MIMO). Several MIMO algorithms have been introduced in literature, from the year 1987 [44, 94]. A brief overview of algorithms applied specially in the case of gearboxes, its casings and any form of complex enclosures is presented in this section. Multi-point (channel) FxLMS was applied in a frequency range of 0- 3500 Hz [142].

An adaptive algorithm dealing with direct active control of actuators placed on the housing is absent in literature. The active vibration control for enclosures is mostly dealt in literature from the noise control point of view. Noise is a consequence of vibration, hence the concepts used in active noise control can be easily translated to active vibration control on the gearbox housing. Another advantage of directly using active noise control concepts is the frequency range of application. As there are a lot of active noise control studies for the casings [136].

For reducing the complexity of implementation of MIMO algorithms, several simplifications have been proposed in literature for active control of noise in casings. For example switching error algorithm [92] and mixed error approaches [99]. Unfortunately such simplifications were not found for active control of vibration. Hence, each of these algorithms is studied in great detail in this thesis in Chapter 6 in the context of gearbox housings. Experimental validation on the gearbox with real operating conditions is also successfully demonstrated.



3 Modelling of high frequency gear whine dynamics

For the development of an Active Vibration Control (AVC) system, the complete understanding of the transfer path of vibrations is necessary. A well validated model helps in predicting the force requirements for a potential actuator to be designed for vibration control as well as helps in determining the appropriate position for maximum controllability.

In this case, the need is to specifically have a model that can predict the vibration response of the mounting points of the gearbox housing in frequency range of 500 - 5000 Hz with a reasonable accuracy so that the actuator forces can be derived for the design of the AVC system.

As introduced in Section 1.3 the modelling of both the prototyping and demonstration gearboxes are undertaken in this chapter. Each of the models is described in detail in Sections 3.1 and 3.2. A clear description of assumptions are presented for each of the modelling approaches. A validation and identification of important model parameters is also presented using experimental setups. Finally, a system level model is introduced in Section 3.3 for further development of the active vibration control system. The overall organisation of the modelling work is shown in Figure 3.1. The blue arrows indicate the flow of derived results from each of the models.

Modelling requirements for the gearboxes

Each of the gearbox models is divided into two sub-models: the gear train (source of excitation) and the gearbox housing (receiver). The two gearboxes had different modelling needs for the gear train. In the prototyping gearbox, the geartrain is excited with only a dynamic force without any rotation of the gear, hence no detailed consideration of micro geometry issues was required. In the demonstration gearbox, it is necessary to consider the oscillatory nature of gear-mesh excitation due to rotation of the gear on the shaft during operation. The housings of both the gearboxes is modelled using finite elements and attached to the geartrain at relevant bearing and attachment points.

The prototyping gearbox has a non-rotating gear train, hence the gear whine is directly imposed via the piezo-mechanism and thus the main focus was on modelling the structure borne vibration transfer paths in the gearbox housing, studying different parameters that affect the vibration transfer and deriving actuator requirements for active vibration control. Since no transient movements of the bodies in the model occur, the modal analysis using a finite element approach using ANSYS was employed. The forces generated by this gear train is transferred to the housing substructure via appropriate connecting elements for

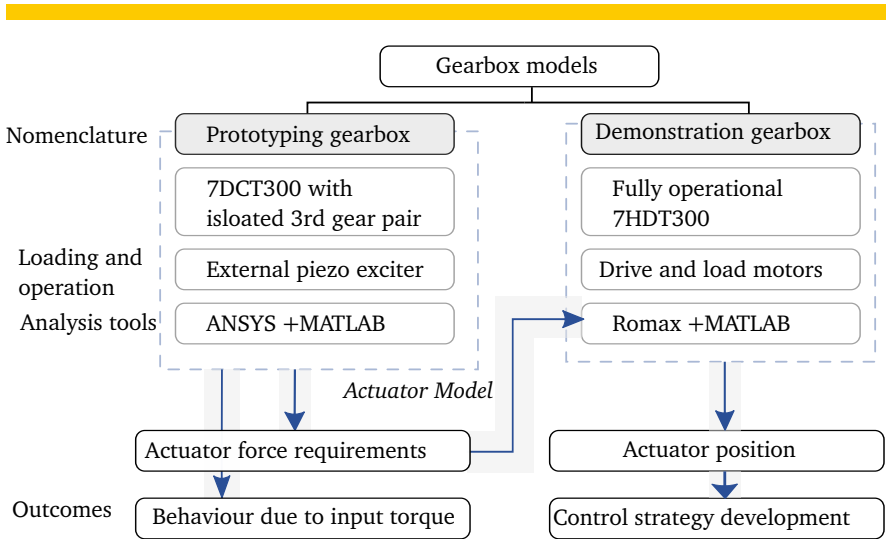


Figure 3.1: Summary of gearboxes for AVC development

the bearings and the test-rig fixture. The modelling approach for the prototyping gearbox is explained in detail the Section 3.1.

For the demonstration gearbox, the challenge is also to consider the rotating nature of the excitation. From the survey performed in Section 2.3.1, it was concluded to use Romax Spectrum module, which has the ability to model gears with appropriate micro-geometry and realistic manufacturing deviations, also including realistic database of bearings. The FE model of the gearbox housing discretized in ANSYS can be imported as a sub-structure. This includes its flexibility and hence captures the effect of gear whine on the housing in real rotational conditions. The end goal of this model would be to develop and extend the actuator design principle to design a placement strategy to apply in the real operating conditions.

3.1 Model of the prototyping gearbox

The main goal of this study is to characterise the dynamic vibration behaviour of the gearbox housing and to use this information to develop a relevant active vibration control strategy. The entire gearbox model is divided into two sub-models:

1. Gear train model: This sub-model comprises of the load generating mechanism with which the gearbox is excited. It also consists of all elements of the gear

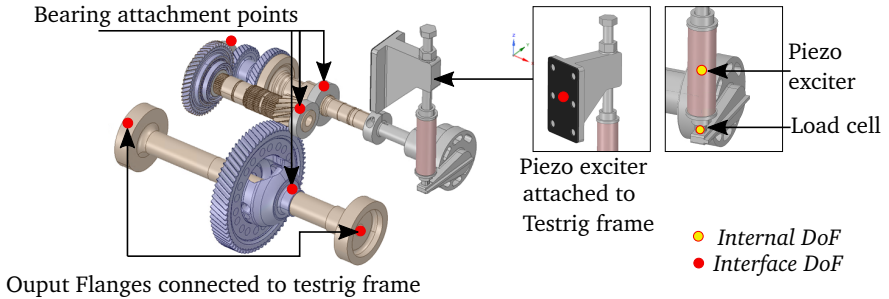


Figure 3.2: Geartrain model Degrees of Freedom

train including the main gear pair and the final drive gear pair which is locked for static condition. The locking is achieved by connecting the output shafts from the geartrain to the flanges that are rigidly attached to the housing.

2. Housing model: The second part of the gearbox model consists of the gearbox housing and the test rig frame. The connection between the gear train model is made via the bearing attachment points indicated by red dots in Figure 3.3 and the differential locking outputs.

The motivation behind dividing the model into two models is the load dependent parameters explored in [101] of this project. The effect of load on the primary path resonances (from piezo exciter to vibration measured on housing) have been proven to vary under different input torques in the geartrain, but the secondary path (from a force imposed on a point on the housing to vibration measured on housing) is negligible. It is easier to model the load changing parameters in the gear train model at the loading mechanism and bearings as the gearbox housing remains unaffected with imposed load.

Each of the sub-models of the prototyping gearbox is simulated in ANSYS. A state-space formulation of the relevant DOFs for each of the models is created. For the gear train, the DOFs are the bearing connection points, the output flanges and the points where the piezo exciter attaches to the plate of the gearbox housing indicated in Figure 3.2. For the gearbox housing model, the relevant interface DOFs are located in the same position as described in the gear train model shown in Figure 3.3. In addition, spatially distributed points across the housing are also included to study the vibration behaviour of relevant points as seen in Figure 3.5.

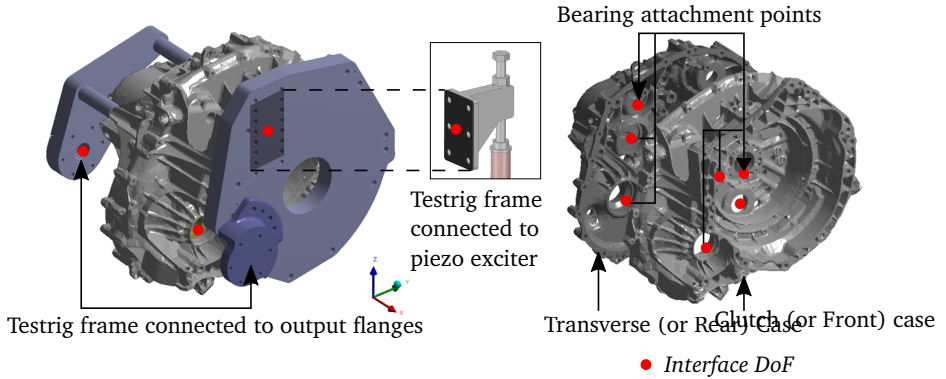


Figure 3.3: Internal and interface DOFs for gearbox housing model

3.1.1 Assumptions of model

The following assumptions were made while developing the model to predict the gear whine vibration response on a gearbox housing structure that was analysed using ANSYS:

1. The system is assumed to be Linear-Time-Invariant (LTI) so that it can be easily analysed in the frequency domain with superposition principle of transfer functions.
2. The system response is linearised for a particular static load. Since the secondary path i.e. load paths in the housing are unaffected by the static load imposed, it is considered a logical assumption to derive a linearised model.
3. The piezoelectric stack actuator in the piezo exciter is not modelled as an electro-mechanical component in ANSYS. Only the equivalent force measured by the load cell in the test setup is directly used as force excitation in the system along with its equivalent mechanical properties.

The modal analysis is a first step in extracting the state space matrices for the finite element model of the gearbox. The contacts between components and materials are set to be linear and the boundary conditions are set to be free-free. The main objective is to study the local modes of the gearbox housing, which remain unaffected with this free-free condition compared to the as-installed condition in the car. The gear contacts are defined with bonded elements (linear connections). The finite element model serves as a directional guide to select the most susceptible positions on the gearbox housing for actuator positioning. For connecting two models via state-space, two kinds of degrees of freedom (DOFs) are defined: Internal DOFs and Interface DOFs as shown in Figure

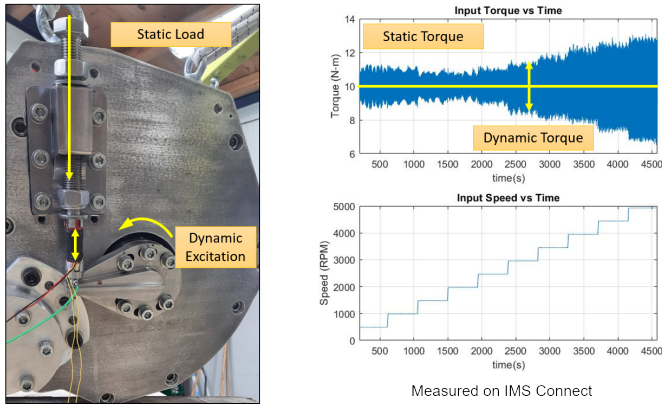


Figure 3.4: Geartrain loading compared with a rotational set-up

3.2. Internal DOFs consist of the gear pairs and the piezoelectric exciter. The first kind of interface DOFs are used to connect the two models, via a stiffness parameter as in bearings, where the relative motion is allowed. The second kind of interface DOFs are rigid connection points as in the flange and exciter attachment points, where the relative motion is constrained. These points are connected to each other via acceleration mapping, which is described further. The models are simultaneously correlated with experimental data to identify relevant parameters like damping and bearing stiffness.

3.1.2 Geartrain model

The first sub-model consisting of the gear-train with the piezo-exciter is evaluated to model the loading mechanism as realistically as possible. The loading mechanism is shown in Figure 3.4. The piezoelectric stack actuator is required to simulate a realistic torque profile of gearbox in rotating condition. On the right side of Figure 3.4, is the torque profile measured on IMS Connect with the full 7DCT300 installed for experimental study prior to development of the prototyping gearbox [104]. The static torque is imposed with the loading screw, this simulates the input torque to the transmission. The dynamic variation in the load occurs due to the speed, which is achieved using the piezoelectric exciter with sine signals. The actual load going into the test-rig is measured with a load cell placed below the piezoelectric stack actuator.

Remote points are extracted from ANSYS as a group of nodes that would connect from one sub-model to another. The remote points for the fully constrained output flanges are connected to the test rig frame test-rig frame defined in the Gearbox housing model also

shown in Figure 3.3. These attachment points would be connected to their counter points in the gearbox housing model via acceleration mapping constraints. The main parameters to be correlated in this model is the modal damping using the load cell reading of dynamic force transferred to the gearbox prototype.

The mesh is generated using a combination of HEX20 (for simple shapes) and TET10 elements for complex shapes with an average mesh size of 3 mm. There are six bearing attachment points in the geartrain. The geartrain is analysed in free-free condition as well to extract the state-space modal model using ANSYS in the frequency range 500 - 5000 Hz. The modal state-space model for of the geartrain can be extracted with ANSYS SPMWRITE command specifying both the internal and interface DOFs as follows:

$$\begin{aligned} \{\dot{x}_{gt}\} &= [A_{gt}]\{x_{gt}\} + [B_{gt}]\{u_{gt}\} \\ \{y_{gt}\} &= [C_{gt}]\{x_{gt}\} + [D_{gt}]\{u_{gt}\}, \end{aligned} \quad (3.1)$$

where x_{gt} and y_{gt} represent the state and output vectors of the DOFs comprising only of the geartrain model. $[A_{gt}]$, $[B_{gt}]$, $[C_{gt}]$ and $[D_{gt}]$ are the corresponding matrices that make up the state-space representation of the geartrain model. $\{u_{gt}\}$ represents the loads imposed on the geartrain, for example, the load from the piezo-exciter.

Modal formulation is preferred for a complicated system. Mass and stiffness matrices of complicated models like the geartrain and gearbox are generally dense and unstructured leading to large calculation times. Modal models pose an advantage of decoupling of individual modes and the mass and stiffness matrices are diagonalised making it computationally efficient.

Gearbox housing model

The housing of the prototyping gearbox is discretization into 700,000 elements using the TET10 (quadratic tetrahedral) mesh due to its complicated geometry. The nominal mesh size used for the housing is in the range 5 - 7 mm to capture the complex details of the gearbox housing. A directional value for the mesh size to capture structural vibrations is given by the equation of longitudinal wave velocity in aluminium up to a frequency range of 10kHz. Other studies have also reported performing Modal analysis on structures made out of aluminium in the range of 5 - 10 mm for the similar frequency range in this study [6].

The interface and internal DOFs are indicated in Figure 3.3 and 3.5. The connection points of the test rig frame indicated by the output shaft and piezo exciter points are connected to this model at the test-rig frame. The corresponding bearing attachment point in the geartrain connect to the housing at the bearing seats at the location in the right part of the Figure 3.5. The internal DOFs are dominated by the spatially distributed points on the gearbox housing. These points are selected based on the modal strains occurring in the mode shapes of the gearbox housing across the frequency of interest upto 5000 Hz.

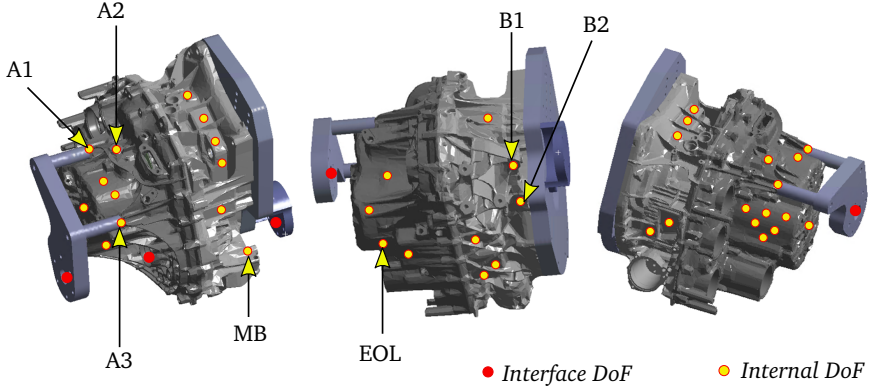


Figure 3.5: Internal and interface DOFs for Gearbox housing model

To extract the modal state space model of this gearbox housing, it is also analysed similar to the geartrain using ANSYS and the modal state space matrix is extracted with the interface and internal DOFs as follows:

$$\begin{aligned} \{\dot{x}_{gb}\} &= [A_{gb}]\{x_{gb}\} + [B_{gb}]\{u_{gb}\} \\ \{y_{gb}\} &= [C_{gb}]\{x_{gb}\} + [D_{gb}]\{u_{gb}\}, \end{aligned} \quad (3.2)$$

where x_{gb} and y_{gb} represent the state and output vectors of the DOFs comprising only of the gearbox housing model including the points on the housing and bearing connection points. $[A_{gb}]$, $[B_{gb}]$, $[C_{gb}]$ and $[D_{gb}]$ are the corresponding matrices that make up the state-space representation of the gearbox housing model. $\{u_{gb}\}$ represents the loads imposed on the housing via the bearings and the test-rig frame.

Properties of modal model

In each of the extracted modal models, the state matrix A that contains the physical parameters of the structure such as stiffness and damping in a diagonal form given by

$$\mathbf{A} = \begin{bmatrix} [0] & [I] \\ [\Gamma_1] & [\Gamma_2] \end{bmatrix} \quad (3.3)$$

The terms Γ_1 , Γ_2 are given by:

$$\begin{aligned} [\Gamma_1] &= \begin{bmatrix} -\omega_1^2 & 0 & \dots & 0 \\ 0 & -\omega_2^2 & \dots & 0 \\ 0 & \dots & \dots & 0 \\ 0 & 0 & \dots & -\omega_N^2 \end{bmatrix} \\ [\Gamma_2] &= \begin{bmatrix} -2\zeta_1\omega_1 & 0 & \dots & 0 \\ 0 & -2\zeta_2\omega_2 & \dots & 0 \\ 0 & \dots & \dots & 0 \\ 0 & 0 & \dots & -2\zeta_N\omega_N \end{bmatrix} \end{aligned} \quad (3.4)$$

The ω_n represents the natural frequency of the model. When the modal model is exported from ANSYS, no damping is present. While creating the initial modal models, a 2% damping ratio, i.e. $\zeta = 0.02$ is assumed. In next step of combining the two sub-models, the modal damping would play an important role to stabilize the overall system. Since the damping ratios occur in a vector form that can be easily represented as a diagonal matrix, it is very convenient to identify the relevant modal damping ratio with experimental data. The diagonal terms in Γ_2 are iteratively updated using the Levenberg-Marquardt optimization algorithm. The objective is to minimize the difference between vibration responses calculated at housing locations using the model and the experimentally measured values. The experimental value of vibration used for correlation are obtained by exciting the piezoelectric stack with a sine sweep voltage and measuring with an accelerometer. The Frequency Response Functions (FRFs) are derived for the measured accelerations with reference the load cell values as a reference.

The general representation of the geartrain and gearbox housing modal models can be written as a block-diagonal form as follows:

$$\begin{aligned} \begin{Bmatrix} \dot{x}_{gt} \\ x_{gb} \end{Bmatrix} &= \begin{bmatrix} A_{gt} & \\ & A_{gb} \end{bmatrix} \begin{Bmatrix} x_{gt} \\ x_{gb} \end{Bmatrix} + \begin{bmatrix} B_{gt} & \\ & B_{gb} \end{bmatrix} \begin{Bmatrix} u_{gt} \\ u_{gb} \end{Bmatrix} \\ \begin{Bmatrix} y_{gt} \\ y_{gb} \end{Bmatrix} &= \begin{bmatrix} C_{gt} & \\ & C_{gb} \end{bmatrix} \begin{Bmatrix} x_{gt} \\ x_{gb} \end{Bmatrix} + \begin{bmatrix} D_{gt} & \\ & D_{gb} \end{bmatrix} \begin{Bmatrix} u_{gt} \\ u_{gb} \end{Bmatrix} \end{aligned} \quad (3.5)$$

Let the above equivalent system be a state space model with \mathbf{A}_d , \mathbf{B}_d , \mathbf{C}_d and \mathbf{D}_d as its matrices. It is to be noted that at this stage the sub-models are not yet connected via the various constraints and bearing elements. This is presented in the next section.

3.1.3 Combining state space models

The acceleration measured on the housing can take multiple structure-borne vibration paths from the geartrain to the gearbox housing. One is via the bearing attachment points using the relative displacement multiplied by the respective bearing stiffness. The other structural vibration path in the given test-rig is via the structure. Since the gearbox is

artificially excited externally using the piezo exciter in contrast to implicit parametric excitation in a real gearbox, the structure-borne vibration transfer via the test-rig frame should not be neglected. Since a LTI formulation is considered the vibration at the desired location A2 on the gearbox denoted by $Y_{gt,A2}$ on the gearbox, as a linear superimposition of the effects of the two transfer paths from the imposed excitation F_{piezo} in frequency domain.

$$Y_{gt,A2}(s) = H_{bea,A2}F_{piezo}(s) + H_{fix,A2}F_{piezo}(s) \quad (3.6)$$

where $s = j\omega$ and $j = \sqrt{-1}$. $H_{bea,A2}$ is the transfer function from piezo exciter to point A2 on the gearbox housing via the bearing connection point. $H_{fix,A2}$ is the transfer function from piezo exciter to point A2 on the gearbox housing via the test-rig frame (fixture).

Bearing connection transfer path

To combine two state-space models via the bearing connection points, the interface forces are calculated at the bearing attachment points using the relative displacement of the corresponding DOFs in two radial directions of the bearings and their bearing stiffness values. The displacement outputs of each of the sub-models is fed-through the bearing coupling matrix K_b ; which is a bearing stiffness mapping matrix, having positive bearing stiffness in the DOFs at the gear train model and negative value of the same stiffness at the DOFs at the gearbox housing model. The equal and opposite feedback bearing forces are fed to corresponding DOFs in the geartrain and gearbox models.

$$\begin{aligned} \{\dot{x}\} &= [A_d]\{x\} + [B_d](\{u\} + [K_b]\{y\}) \\ \{y\} &= [C_d]\{x\} + [D_d](\{u\} + [K_b]\{y\}) \end{aligned} \quad (3.7)$$

where $\{x\}$ and $\{y\}$ are the stacked states and output DOFs from the block diagonal representation in Equation 3.5. Rearranging terms in Equation 3.7 to form an equivalent state space representation gives:

$$\begin{aligned} \{\dot{x}\} &= [A_d + K_b(I - D_d K_b)^{-1} C_d]\{x\} + [B_d + (I - D_d K_b)^{-1} D_d]\{u\} \\ \{y\} &= [(I - D_d K_b)^{-1} C_d]\{x\} + [(I - D_d K_b)^{-1} D_d]\{u\} \end{aligned} \quad (3.8)$$

All the transfer functions calculated from the piezo exciter to the desired location on the gearbox housing using this transfer path is represented as H_{bea} as in Equation 3.6. Bearing stiffness values are load-dependent. The non-linear behaviour in rolling bearings arises from factors like non-linear stiffness, Hertzian contact stresses, and clearance. Hence it is approximated by a linearised behaviour near the operational load. Hence, from a short analysis of the gear train presented in Appendix B, the linearised bearing stiffness values for the particular static input torque is taken.

Fixture connection transfer path

For the fixture transfer paths, the two sub-models are joined via constraint equations at the corresponding interface DOFs at the test rig frame. This means the displacements, velocities and accelerations are equal at the interface points on either of the models. The joining of two sub-models using constraints has been simplified using the Lagrange State-space sub-structuring in a recent paper [39]. The simplification proposed here is just by using the acceleration outputs of the state-space models and simultaneously mapping back the interface forces. Only using the acceleration outputs, means using only part of the \mathbf{C}_d and \mathbf{D}_d matrices connecting the acceleration outputs of the sub-models, henceforth represented as $\mathbf{C}_{d,ac}$ and $\mathbf{D}_{d,ac}$.

To constrain the sub-models, a constraint mapping square matrix of size of total number of combined outputs is created called $[Q_f]$. For each pair of interface DOFs, the related coefficients of matrix $[Q_f]$ must have an absolute value of 1 and be opposite in sign. Without calculating the interface forces, the combined state space model to derive the H_{fix} transfer path is given by:

$$\begin{aligned}\{\dot{x}\} &= [A_f]\{x\} + [B_f]\{u\} \\ \{y\} &= [C_f]\{x\} + [D_f]\{u\}\end{aligned}\quad (3.9)$$

where

$$\begin{aligned}[A_f] &= \mathbf{A}_d - \mathbf{B}_d \mathbf{Q}_f^T (\mathbf{Q}_f \mathbf{D}_d \mathbf{Q}_f^T)^{-1} \mathbf{Q}_f \mathbf{C}_d \\ [B_f] &= \mathbf{B}_d - \mathbf{B}_d \mathbf{Q}_f^T (\mathbf{Q}_f \mathbf{D}_d \mathbf{Q}_f^T)^{-1} \mathbf{Q}_f \mathbf{D}_d \\ [C_f] &= \mathbf{C}_d - \mathbf{D}_d \mathbf{Q}_f^T (\mathbf{Q}_f \mathbf{D}_d \mathbf{Q}_f^T)^{-1} \mathbf{Q}_f \mathbf{C}_d \\ [D_f] &= \mathbf{D}_d - \mathbf{D}_d \mathbf{Q}_f^T (\mathbf{Q}_f \mathbf{D}_d \mathbf{Q}_f^T)^{-1} \mathbf{Q}_f \mathbf{D}_d\end{aligned}\quad (3.10)$$

Usually, modal or viscous damping approaches are applied in gear simulation for the analysis of resonances up to the higher frequency range [41]. Romax despite providing an option to change each modal damping quantity, this is reported to be performed by manual inspection with test responses.

Although Rayleigh damping would be an easier model to tune, because of the only two parameters α and β , it would insufficiently capture the high frequency dynamics. Hence modal damping, where each individual damping ratio of the resonance frequencies observed is tuned is preferred for such models.

Model correlation of the gear train

The modal damping of the gear train sub-model is first correlated with the load cell measurements from a particular load case. The experiment is performed by providing a sine sweep voltage at a particular sine amplitude to excite all the resonances in the prototyping gearbox. The force recorded by the load cell in a sweep test is imposed on the

DOF corresponding to the DOF of the piezo exciter and the resulting acceleration of the DOF at the load cell is directly compared against the value of the experimentally recorded value.

One might assume, that the imposed load would be straight forwardly be transferred directly to the load cell DOF, but as seen in Figure 3.6, when assuming a constant damping (here 5%) over the whole frequency range vs an optimally tuned modal damping ratio, how the high frequency dynamics can affect the accuracy of prediction in the FE model.

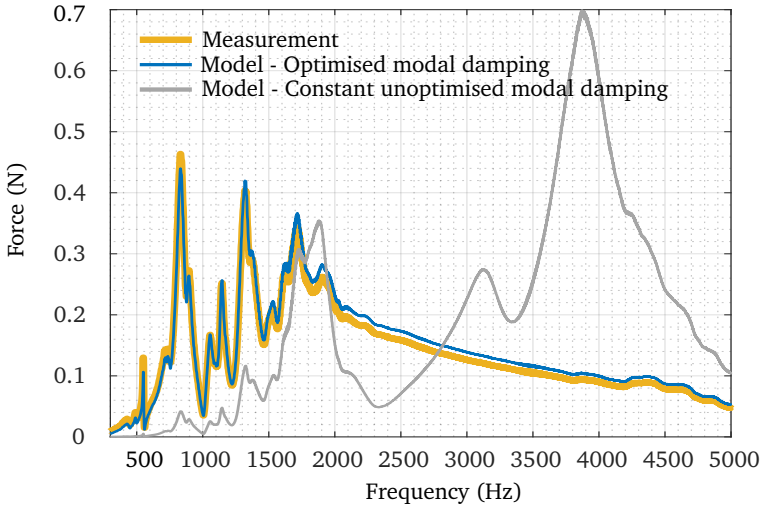


Figure 3.6: Load cell measurement used to tune damping of FE model

Model correlation of combined model

Once the geartrain model is fully identified, modal damping of the gearbox housing is tuned in the combined model response. The damping vector for the gearbox housing model is first altered in each iteration and then the combined model response is generated to compare against acceleration FRF of three internal DOFs indicated in Figure 3.5. the load case used for this study is the 40 Nm input torque with the corresponding bearing stiffness values (Refer Appendix B). Applying input torque greater than 40 Nm caused a slight bend in the exciter mechanism which would induce extra deviations into the operation of the piezo exciter operation and load application. The points used for correlation are EOL: End Of Line correlation point used by the manufacturer, A2: mounting point on transverse

case and MB: mounting point on the clutch case as seen in Figure 3.5.

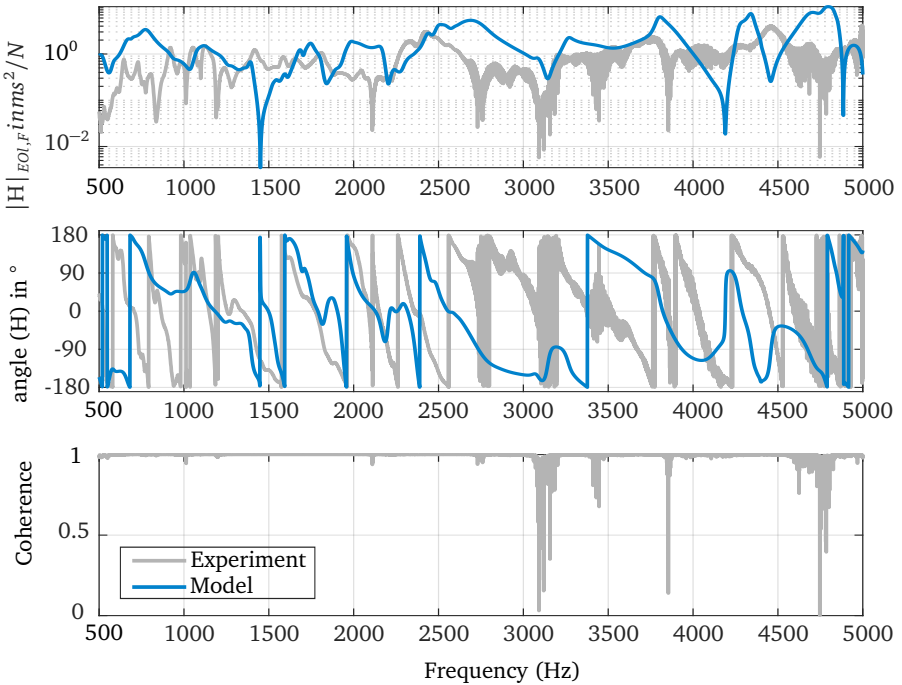


Figure 3.7: Prediction of vibration behaviour for unit force from piezo exciter $H_{bea,EOL}(s) + H_{fix}(s)$ at EOL measurement point

In general from all the three correlation Figures 3.7, 3.8 and 3.9 the model is able to predict the transfer behaviour of vibration from the piezo exciter to the points on the housing with reasonable accuracy. The third subplot in each of the figures represents the coherence of the experimentally obtained data, indicating how much of the vibration produced is directly correlated to the excitation and hence confirms the validity of the performed experiments.

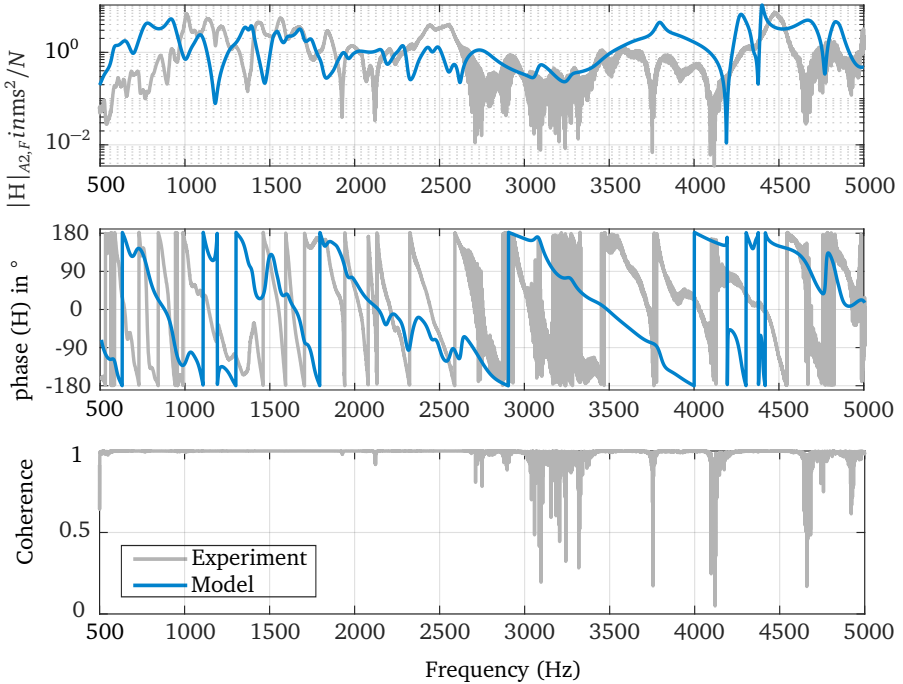


Figure 3.8: Prediction of vibration behaviour for unit force from piezo exciter $H_{bea,A2}(s) + H_{fix,A2}(s)$ at mounting point A2

There is good correlation of the level of vibration especially in the region of 1000 - 2800 Hz. The constraints imposed on the DOF attachment points treating them as completely rigid contacts could also be affecting the slight deviations in the frequency range 500 - 1000 Hz for the measurement points on the transverse case and between 800 - 1300 Hz at the measurement point on the clutch case. However no general conclusion can be derived. Despite the differences in the magnitudes of vibration transfer behaviour from the piezo exciter, resonance peaks align in this frequency range.

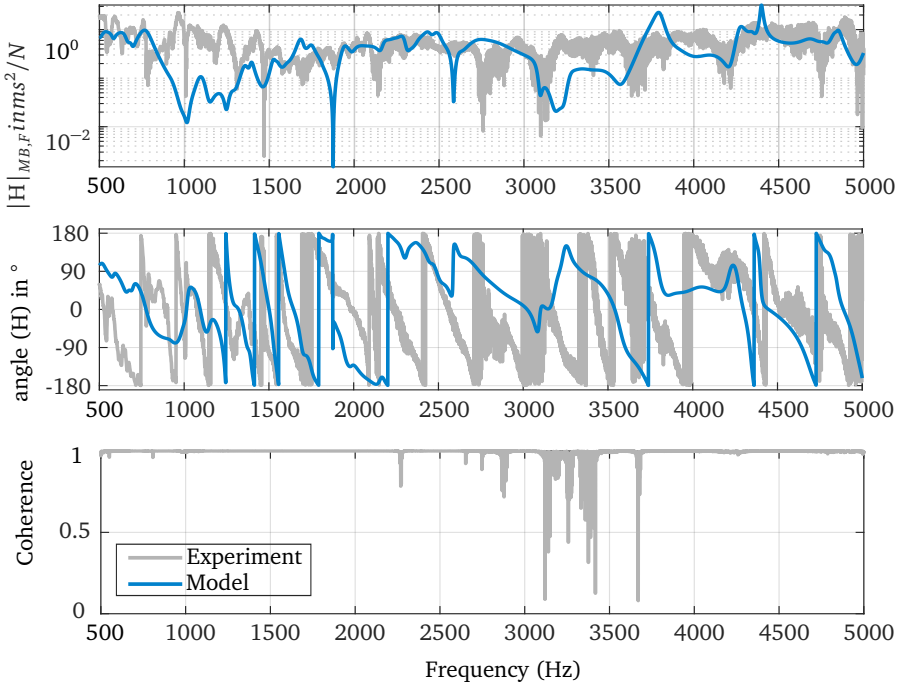


Figure 3.9: Prediction of vibration behaviour for unit force from piezo exciter $H_{bea,MB}(s) + H_{fix,MB}(s)$ at mounting point MB

Overall the differences between the vibration behaviour predicted by the model and the measurement can be attributed to the assumptions related to the linearised connections in the model. Assumption of the linearised contact between the two cases which in reality is joined via several bolts that could affect the high frequency vibration transfer paths. Even at the interface DOFs indicated in red in Figure 3.3, the test rig attachment points are condensed to one remote point per attachment. This is a significant simplification performed to reduce the model size and complexity when combining the models, rather than considering each individual bolt as a DOF. This simplification could possibly explain the fewer resonances observed above 3000Hz. However, despite these simplifications, there is no substantial loss in the transfer of vibration magnitude from the piezo exciter.

Effect of fixture

A comparison of the H_{bea} and H_{fix} is presented for all the three correlation points in Figure 3.10. It can be observed that the vibrations in the lower end of the desired frequency range transfer via the bearings mostly up to 1600Hz, while the fixture contributes to the high frequency dynamics. This is the trade off given the simpler non-rotating setup compared to a fully operational rotating test set up. The vibrations produced by the non-rotating simplified test-rig were validated against the fully operational 7DCT300 with a laser vibrometer [104] and various loads and speeds by tuning the frequency of voltage to the piezo exciter. Despite causing vibrations in the high frequency region via the fixture and not the bearings, the test-rig imposed an excitation into the system that would produce an equivalent vibration as that of an operational gearbox. Hence, gear whine vibrations can be artificially imposed on the housing without the need of complicated testing equipment.

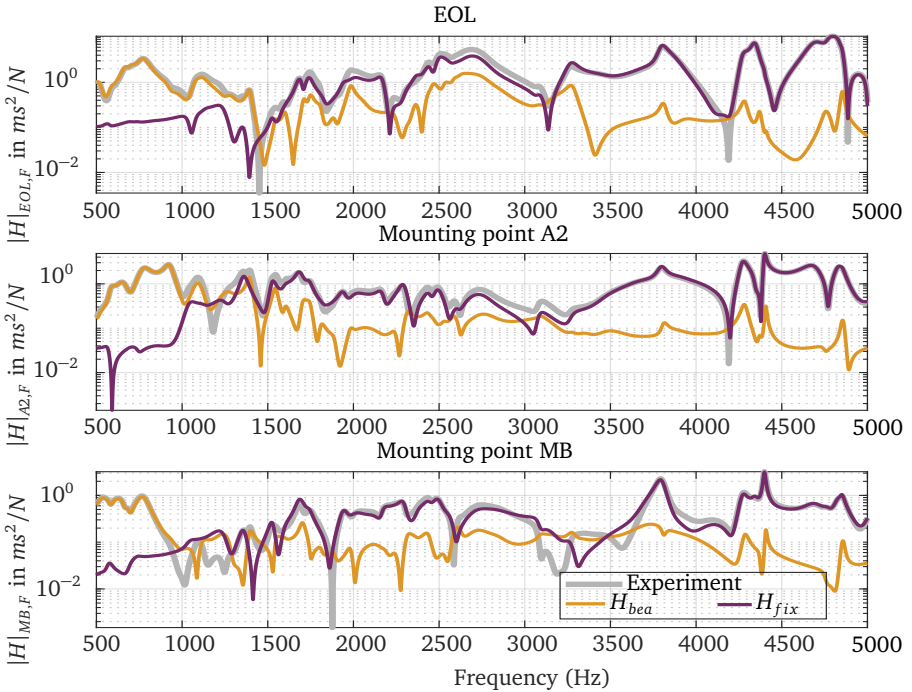


Figure 3.10: Comparison of vibration transfer paths in the Prototyping gearbox

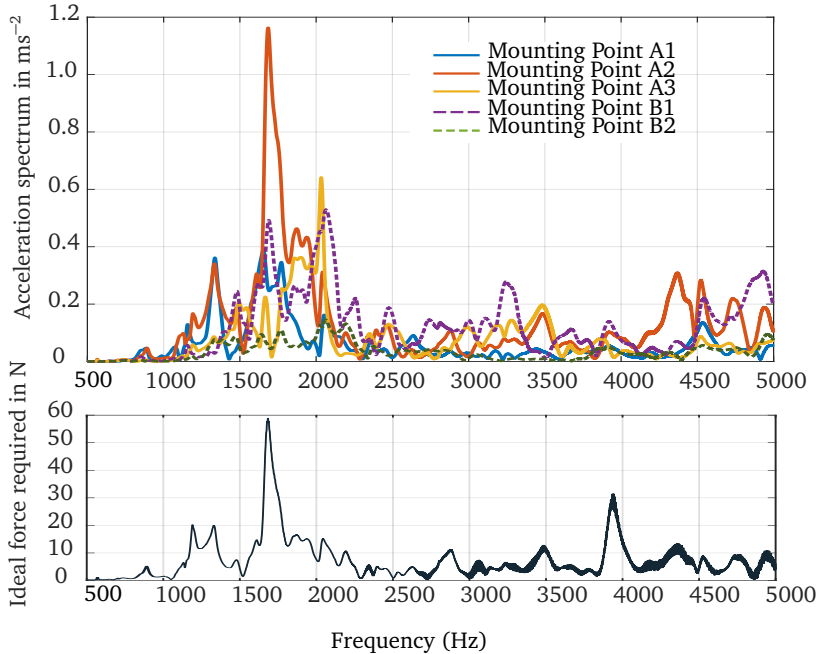


Figure 3.11: Derivation of actuator force

3.1.4 Actuator force requirement

The vibration behaviour of the secondary path i.e for a force imposed on one of the internal DOFs on the gearbox housing to the desired control location i.e. a mounting point does not change with load. This has been established experimentally for the given test-rig [101]. Hence, a single model derived in the previous section for only one load case is sufficient for further development of the actuator requirements. The vibration levels in response to sine sweep voltage for the piezo exciter for the five mounting points shown in Figure 2.3 is analysed from the model. It can be seen that mounting point A2 on the transverse case has the highest vibration among the five points. Mounting points on the clutch case are on a comparatively rigid part of the gearbox housing, hence the vibration is lower. Hence the vibration of the point A2 can be used as a baseline to derive the force requirements. The vibration also has the highest magnitude in the frequency range 1000 - 2500 Hz.

The force spectrum is derived for each frequency point using the formula by dividing the acceleration in frequency domain with the secondary path transfer function of a suitable



point on the housing, here using a point on a clutch case as the force transmissibility is lower compared to a point on the transverse case. To derive the worst-case scenario, i.e maximum force needed, The transfer function (acceleration per unit force) from an internal DOF point on the clutch case is used. After doing so the force derived is shown in Figure 3.11. Therefore accounting for safety margins due to unexplored spatial points, a 100N force has been set for the design requirement in the frequency range 500 - 5000 Hz.

3.2 Model of the demonstration gearbox

The main difference between the model of the prototyping gearbox and the demonstration gearbox is the ability to model the excitation according to the gear meshing phenomenon using appropriate contact models. In the prototyping gearbox the gear-mesh excitation is artificially introduced and can be easily quantified by correlating it to the voltage of the piezoelectric exciter, hence it is measurable. In reality, the gear-mesh is a parametric internal excitation, which cannot be measured directly. Hence, the correlation methods applied for validating the vibration obtained from the model would differ. The demonstration gearbox also is a multi-stage gearbox with seven speeds compared to a two-stage simplified version presented in the previous section. The model can be studied for different speeds and gear-engagement ratios.

As discussed in Section 2.3, it is necessary to first set the bounds on the model fidelity needed to be achieved for the gear train model and choose a modelling software accordingly. The focus here is to accurately model the gear excitations and not really to study the gear deformation as a consequence of lightweight and manufacturing deviations. Therefore, the Advanced Empirical model fidelity has been chosen. The model of the demonstration gearbox, which is a series production 7HDT300 is performed in Romax software using the Spectrum module.

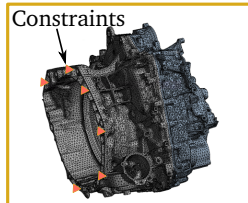
Assumptions of the model

Before proceeding to the model building using Romax, a few assumptions of the modelling procedure are stated as follows:

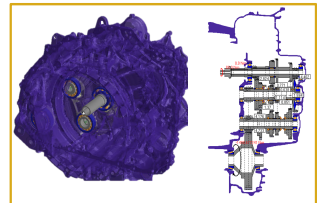
1. Shafts are modelled as Timoshenko beams.
2. Gear micro geometry for all gears are assumed nominally after discussion with the manufacturer and ISO norms summarised in Table 3.1
3. Stiffness of the bearings is load-dependent, i.e. the non-linear nature of these contact models is linearised for each operating load case similar to the model of the gearbox prototype. But here, Romax performs this automatically.
4. For the gear-mesh contact, the disk model according to ISO 6336-1 [24] and a more detailed disk model with Hertzian contact calculation according to Weber and Banaschek [108, 134] are stored in the quasi-static simulation.



Geartrain model with bearings



Meshed housing model import



Housing with connections and boundary conditions

Figure 3.12: Model development workflow in Romax

5. Multiple power flows in transmissions is performed by synchronisers which are complex in geometry. In the model these are simplified a concept clutch (on /off switch) and hence the inertia of synchronisers, fork shifters and gear shifting motors is neglected.
6. The dynamics of the test-bench and the impending mounts that would be used in the car chassis are not considered in this model.
7. The electric motor in the hybrid transmission is not modelled, as the focus was only on modelling the gear whine vibration under driving conditions using the internal combustion engine side and not the electric motor side.

Microgeometry parameter	Symbol	Nominal Value
Lead Slope	$C_{H\beta}$	20 μm
Lead Crowning	C_{β}	20 μm
Involute Slope	$C_{H\alpha}$	15 μm
Involute Slope	$C_{H\alpha}$	15 μm

Table 3.1: Microgeometry parameters using recommended values from gearbox manufacturer

3.2.1 Model development in Romax

The modelling of the gearbox in Romax can be described in three major steps, also depicted in Figure 3.12:

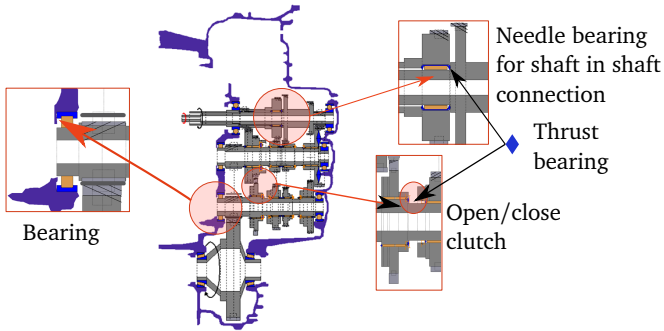


Figure 3.13: Elements of Romax model and simplifications performed

Step 1: Model of gear-shaft-bearing system

Gears are modelled according to the data sheet of the manufacturer. Nominal values of the basic micro-geometry deviations. Gear blanks are modelled as shafts to include the torsional and bending stiffness, which would facilitate a better mesh misalignment solution.

There are two types of gears in the transmission - gears that are machined on the shaft also known as integral gears and the ones that are mounted on the shaft through synchronisers - also known as synchronised gears.

The model developed in Romax does not consider gear shifts dynamics, such as the synchronization of the speeds and the coupling between the axial and rotational dynamics of the synchronizer parts. Instead, a concept clutch is used to represent synchronised gears in the transmission. They impose torsional constraints on the shafts engaged in power transfer. Synchronised gears in the real transmission are mounted on bearings which contribute to the mesh misalignment. Synchronised gears are modelled with gears mounted on additional short shafts that approximate the synchroniser. The short shaft is then mounted with needle bearings are also modelled in Romax to account for the mesh misalignment calculation. However, caution is taken for the axial constraints of the gears on the needle bearings using thrust bearings shown in blue diamonds in Figure 3.13. For concept clutches, care has to be taken about the status of the clutch, either open or closed, so that the additional shafts defined for gears are not left unconstrained. In the absence of proper constraints the static analysis would fail.

Bearings are included from the standard catalogue in Romax. they are modelled detailed 6-DOF non-linear components. The non-linearity arises from the change in stiffness due to operational loading conditions. This load-dependent stiffness is calculated at the static analysis stage for a particular applied load on the gearbox and is assumed to be linearly

valid for the entire speed range in the given load - hence quasi-static linear. Shafts are pressed into the inner seat of the bearing, which is modelled with the press-fit option in Romax with nominal tolerances provided by the manufacturer.

Taper-roller bearings are assembled in the transmission with preload. The study performed by Kanase et al. [66] revealed that the preload of the bearings did not affect the gear whine vibrations measured on the housing. Therefore, the preload is modelled as a constant nominal value provided by the manufacturer.

Step 2: Model of FE housing import and connections

The CAD Model of the housing is meshed in ANSYS, following the guidelines of the mesh size presented in Section 3.1.2. This model is directly imported into Romax and connected to the relevant bearings in the geartrain using RBE3 elements. Bearings are pressed into their bearing seats in the housing. The RBE3 is a powerful tool to efficiently distribute loads and masses in an FE model. Unlike the RBE2 element, the RBE3 does not add additional rigidity to the structure.

Before proceeding to the condensation of the housing, Eight additional points (response nodes for correlation), related to the EOL and mounting points need to be defined. A total of 8 bearings are the connection points between the geartrain and the housing. Once the points are chosen a dynamic condensation using the CMS technique described in Section 2.3.2 is performed. As a rule of thumb the frequency for condensation is least 1.5 times the maximum frequency of interest, so frequencies up to 8000 Hz have been used in this model.

Step 3: Boundary conditions and loading

The nodes connected to the engine plate are constrained in all 6 DOFs in space upon import as shown in the centre image in Figure 3.12. The input torque is imposed on the internal shaft for the odd gear arrangement and on the outer shaft is engaged for even gear arrangements (Figure 3.14).

Dynamic analysis in Romax

To analyse the gear whine responses, the romax model undergoes analysis in three stages:

1. Static Analysis for each operating condition
2. GBTE Analysis: Romax provides an option to perform single gear-pair transmission error analysis, but this is done by just isolating the gear-pair. In a complex gearbox like the 7HDT300, gear meshing in one gear pair would definitely affect the other stages and hence the vibration is not just a simple causal phenomenon. The interest in this thesis is to understand the system level influence of gear-whine phenomenon, hence the Gearbox Transmission Error (GBTE) Analysis is performed.

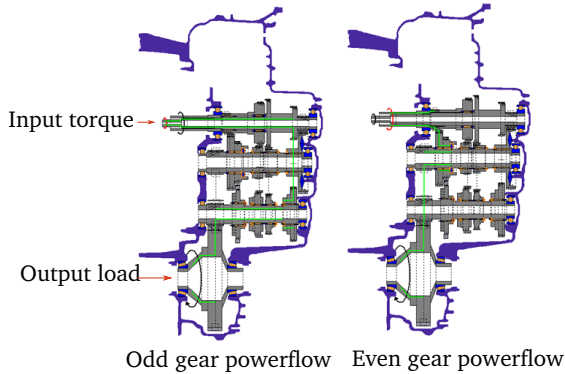


Figure 3.14: Powerflow in odd and even gear arrangements

3. Response analysis for the housing

The modal model of the 7HDT300 gearbox can be extracted from Romax into MATLAB for model update using the preliminary run-up tests described in the next section. All the important degrees of freedom including the gear bodies are imported which is then converted to a modal model for updating the damping of the model.

3.2.2 Run-up test for correlation

Once the model is set-up a correlation between the testing environment and the model needs to be established to prove if the model can represent the gearbox whine phenomenon for the operational conditions sufficiently. Since the excitation in the case of a real operational gearbox i.e. the transmission error cannot be measured directly, operational modal analysis approach is undertaken instead of the experimental modal analysis approach in the previous case of the simplified test-rig. The main parameters to identify are the damping ratios in the given frequency range.

Industrial use cases of Romax [28, 66, 109] have efficiently demonstrated the correlation transmission models with tests. They report good correlation of housing acceleration levels with Romax simulations but no quantitative data has been published. The variation of vibration levels with changing input torque was also reported. None of these studies have clearly described their model updating strategy or values for damping in the system.

The test data used for correlation was generated by running the 7HDT300 transmission on the IMS Connect test rig as described in the beginning of Section 3.2. The measurement of vibration was performed using a single axis piezoelectric accelerometer (Kistler 8640A5T). The data of this sensor is given in Appendix A.1. The sampling frequency

was chosen to be 25.6 kHz which is almost 2.5 times the Nyquist frequency to capture vibrations until 5000 Hz reliably.

Run-up experiments are performed as they will excite a range of resonances of the housing in the desired frequency range as opposed to exciting isolated frequencies when run at single speeds. The speed limit for the ramp up is set from 0 - 5000 RPM which is decided after consulting the maximum speed limits for each engaged gear for the vehicle transmission. In a speed ramp test, the drive speed is varied at constant torque, this will give a constant relative displacement between the teeth with varying frequency [120]. Which means, the constant amplitude of gear mesh excitation is swept at different frequencies.

The measurement point for vibration correlation was obtained at three different points, EOL, mounting point on the front of the gearbox and mounting point on the transverse case of the gearbox shown in Figure 3.15. The model is validated for different operating points and gear engagement ratios as shown in Table 3.2.

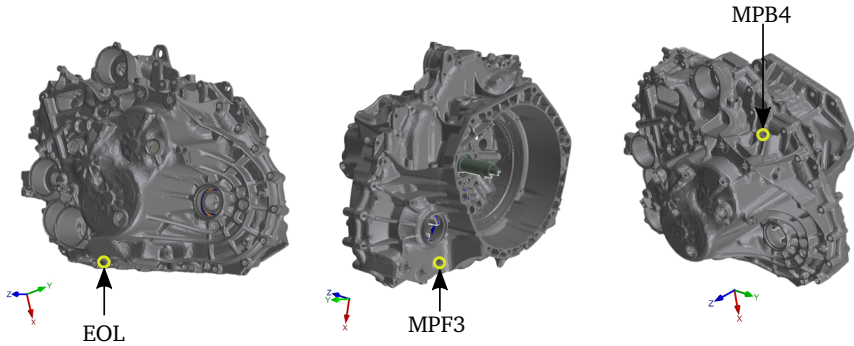


Figure 3.15: Measured points for correlation of Romax model

Experiment Number	Gear Engaged	Input torque (Nm)
1G.20		20
1G.100	1 st	100
3G.20		20
3G.100	3 rd	100

Table 3.2: Test matrix for correlation of Romax model. Speed condition in all cases: ramp from 0 - 5000 RPM

3.2.3 Model updating strategy

Similar to the model of the prototyping gearbox, the modal damping of the demonstration gearbox needs to be identified. In Romax, there is an option to use three different kinds of damping models: constant damping for all modes, Rayleigh damping model and Rayleigh Distributed damping (for lower and higher frequency range). Once again the modal damping approach is chosen owing to ease of implementing in modal models.

The main difference in the model updating strategy for the prototyping gearbox and the demonstration gearbox is the ability to measure the excitation. In the prototyping gearbox, the excitation was easily measurable using the load cell, hence all the FRFs were calculated using this signal as a reference. In the demonstration gearbox, the gear-mesh excitation cannot be measured. Although the input torque can be considered as a swept input (due to speed ramp) with constant amplitude, the sensor on the IMS Connect setup recording the signal had a bandwidth of only 1000 Hz. This does not satisfy the need to generate FRFs up to 5000 Hz according to the Nyquist sampling law. Hence no reliable input signal to the system is available for the demonstration gearbox. In this case an output-only model updating strategy based on operational modal analysis is used.

Operational modal analysis approach is used for updating the models where the excitation forces cannot be measured. This is usually done for big structures like aircraft, bridges, vehicle suspension tests etc. [37]. The main principle involved is to obtain correlation spectra or transmissibility functions to correlate experiments with models using one of the measured outputs as a reference. In context of the 7HDT300 gearbox, the EOL position can be used as a reference for the other two measuring points: MPF3 and MPB4. In the Romax model of the demonstration gearbox, the option to obtain the transmissibility function is readily available in contrast to correlation spectrum. Therefore the transmissibility function is used as the objective to minimize the difference between model and experimental values for update using the Levenberg-Marquardt algorithm of the transmissibility function for 4096 frequency points from 0 - 5000 Hz.

The strategy to update the modal damping coefficients of the Romax model is presented in Figure 3.16 The bearing forces in each operating condition is derived from Romax at all the connection points to the housing for a speed ramp condition that can be simulated. The mass and stiffness matrices for the condensed nodes on the housing, bearing DOFs and gear meshes are exported from the Romax model to MATLAB. The mass and stiffness matrices are converted into a modal state space model, after which it is simulated with the bearing forces at the connection points. The resulting simulated transmissibility function with respect to EOL response node is entered into the optimisation routine.

The first step in model correlation is to identify the resonance frequencies for which the modal damping needs to be tuned. This is done by first analysing the experimental responses using peak-picking method. These frequency points are then compared with the resonances of the model built in Romax. Only the modal damping values for the identifiable resonance frequencies are tuned.

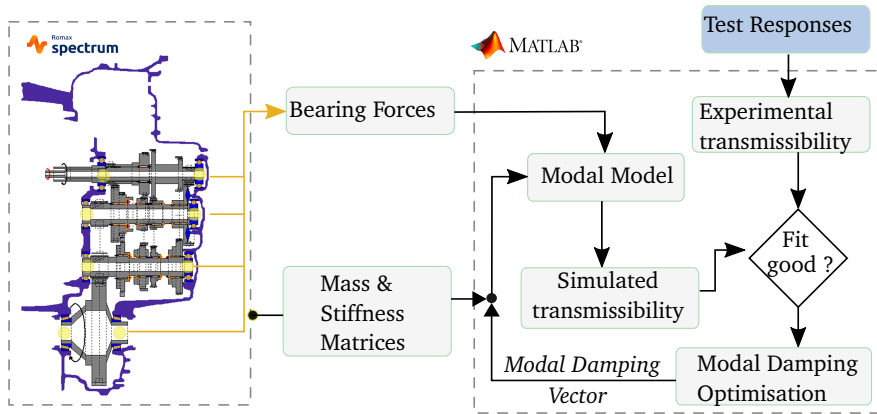


Figure 3.16: Romax model update strategy for the demonstration gearbox

3.2.4 Results of model correlation

Observation of resonances

The measurements for the load case 3G.20 is shown at 3 positions that were highlighted in Figure 3.15. From the three graphs shown in Figure 3.17 it can be observed that in the lower frequency range, upto 2000, the resonance frequencies observed in test are in good agreement with the model. All the three points show deviations in the model predicted values in the higher frequency range. This is a consequence of modelling high frequency dynamics using standard FEA procedures. The uncertainty in the estimated natural frequencies increases in higher frequency range due to overestimated stiffness in contacts and/or bearing connection points due to conservative modelling.

The number of frequencies observed at each of the points do not differ by a great extent. (EOL = 58; MPB4 = 60; MPF3 = 61).

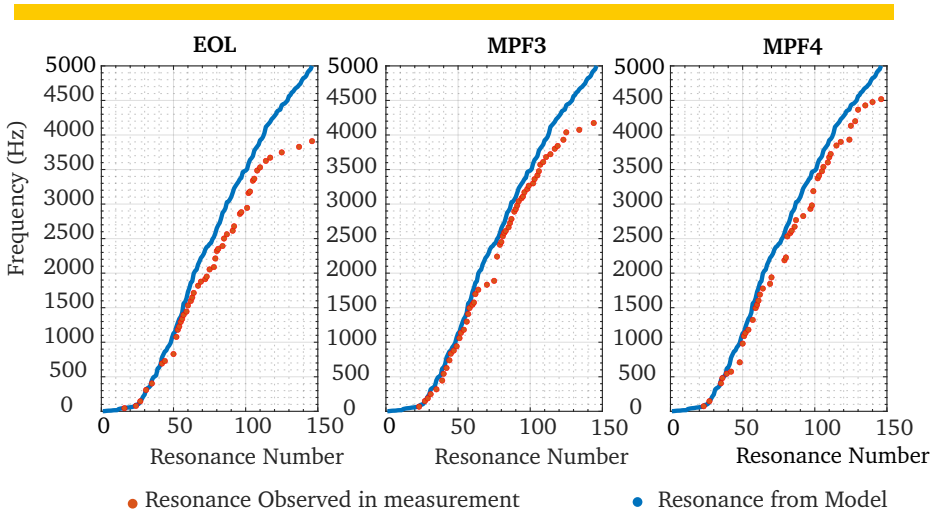


Figure 3.17: Resonance frequencies of 7HDT300 gearbox vs resonances of Romax model

Extraction of transmissibility from experimental data

The run-up consists of first setting the static torque. This is done in the first 10 s of the test, then the speed ramp begins. The input speed of the transmission is ramped from 0 - 5000RPM for a period of 60s. After 5s of achieving the steady state speed, it is then ramped down do zero in the next 15 s. Total test time is 90s. The data important for correlation is the ramp of the speed and is extracted within the appropriate time frame as shown in Figure 3.18. This data corresponds to the EOL position measurement. Similar behaviour is seen for other measurement points.

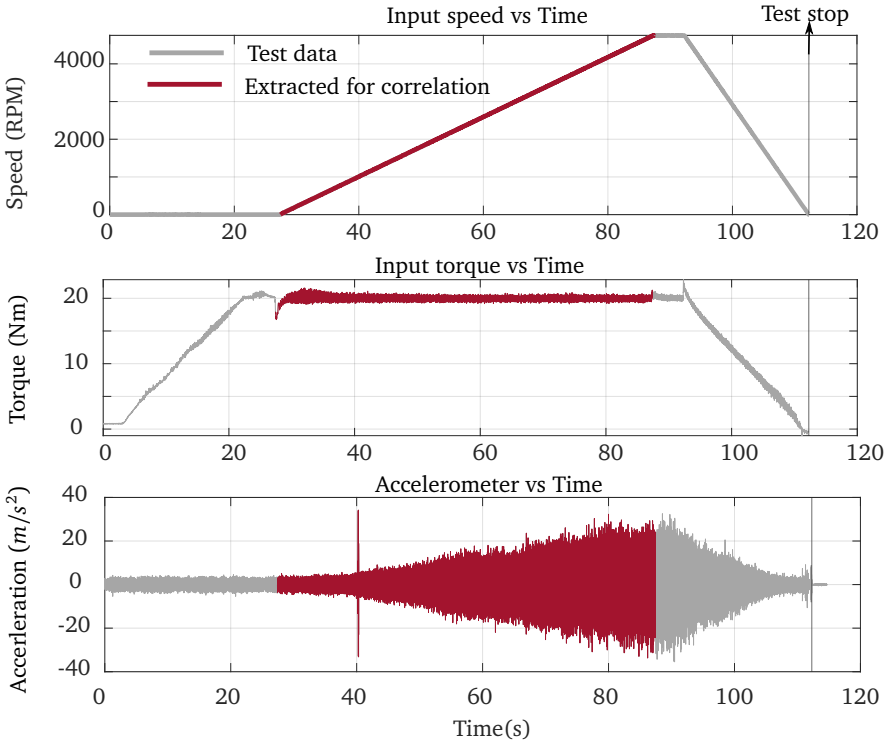


Figure 3.18: Experimental data extraction from run-up test

It can be seen in Figure 3.18 that as speed of the input shaft of the transmission increases, peak to peak acceleration recorded on the housing also increases. This can be attributed to the peak to peak increase in the dynamic torque at the input shaft which is clearly represented in earlier Figure 3.4 in a more clear way. Acceleration responses from EOL, MPB4 and MPF3 can be extracted to calculate the transmissibility of MPB4 and MPF3 with respect to EOL for correlation.

Updated FE model

Since MPF3 point observed most of the resonance frequencies, the model is tuned for these values. As observed from Figure 3.17, the resonance peaks align with the experiment values. The general trend in modal damping has been identified: for the observed modes

within 2000Hz, the damping ratio converged to values in the range of 0.1 - 1 %. For high frequency modes above 3000Hz, the damping was even lower. The optimization routine aimed to fit the transmissibility both at the sensors MPB4 and MPF3 hence the damping values obtained reveal a general trend. It is reported in literature that there is always a 5 - 20 % uncertainty in the predicted damping [20].

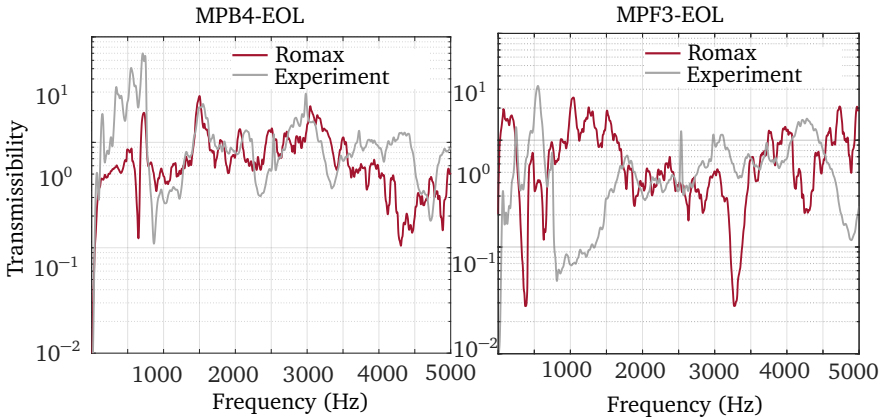


Figure 3.19: Romax model vs experimental transmissibility for 3rd gear 20Nm

The results of the updated model that can predict the transmissibility of gear whine vibration at from EOL point to mounting point on clutch case MPF3 and mounting point on the transverse case MPB4 are shown in Figures 3.19 - 3.22. As a general remark in all the graphs, the peaks corresponding to the resonances can be seen to be easily identifiable in the transmissibility functions of both the mounting points with reference to the EOL position. The peaks are clearly observable and aligned until 3000Hz, which are in agreement with the picked resonances depicted in Figure 3.17 within the same frequency range. Above 3000Hz, fewer resonance peaks can be identified from the test data which is also depicted by the smoother nature of the experimentally determined transmissibility (grey lines) in all the graphs.

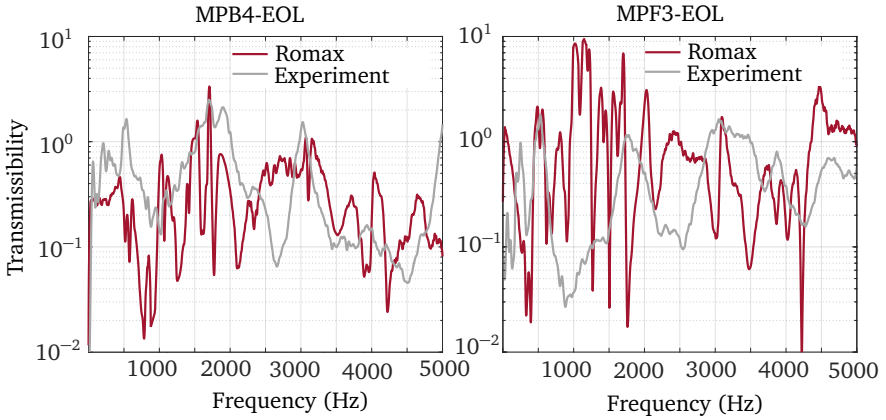


Figure 3.20: Romax model vs experimental transmissibility for 1st gear 20 Nm

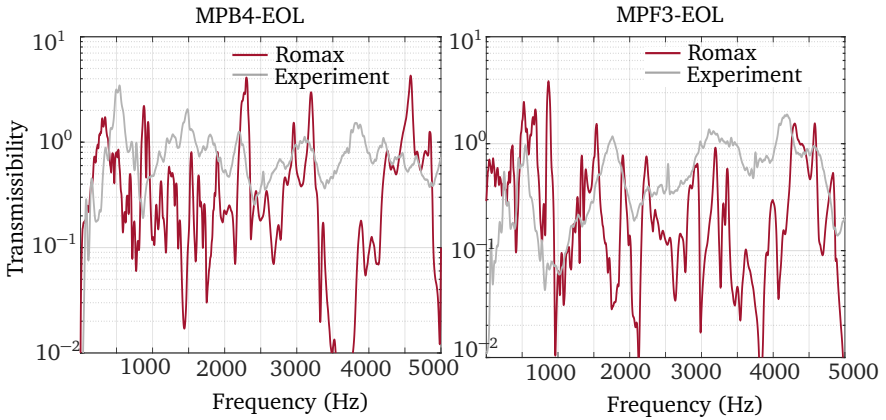


Figure 3.21: Romax model vs experimental transmissibility for 3rd gear 100 Nm

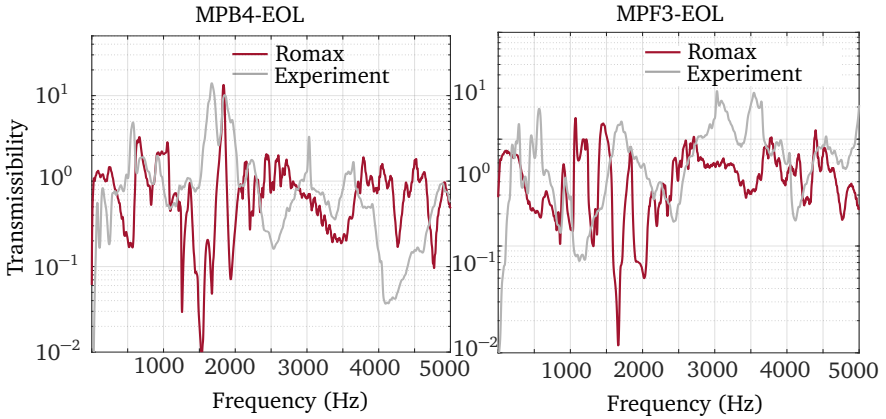


Figure 3.22: Romax model vs experimental transmissibility for 1st gear 100Nm

Apart from the alignment of the responses in peaks there are disagreements in the magnitude of predicted vibration behaviour. This can be attributed back to the assumptions made while building this model. Only four main manufacturing deviations in the gears were addressed with nominal values as well as negligence of many components inside the gearbox could be the possible reason for the mismatch in magnitude at many frequency points. These components could have been source of additional vibration transfer paths contributing to overall increase in vibration especially in the 100N m input torque cases for the frequencies 1000 - 2000Hz and 3000- 4000Hz. Hence predicting the gear whine response from the Romax model for a complicated transmission comes with a lot of uncertainties.

Another reason why despite the fit of the damping the level of magnitudes do not match is because in each iteration of the damping update, the bearing forces are not updated. They are kept at the same level initialised at the optimisation routine when extracted from Romax with all initial constant damping ratios. Correction of this in every iteration of the model update is computationally expensive.

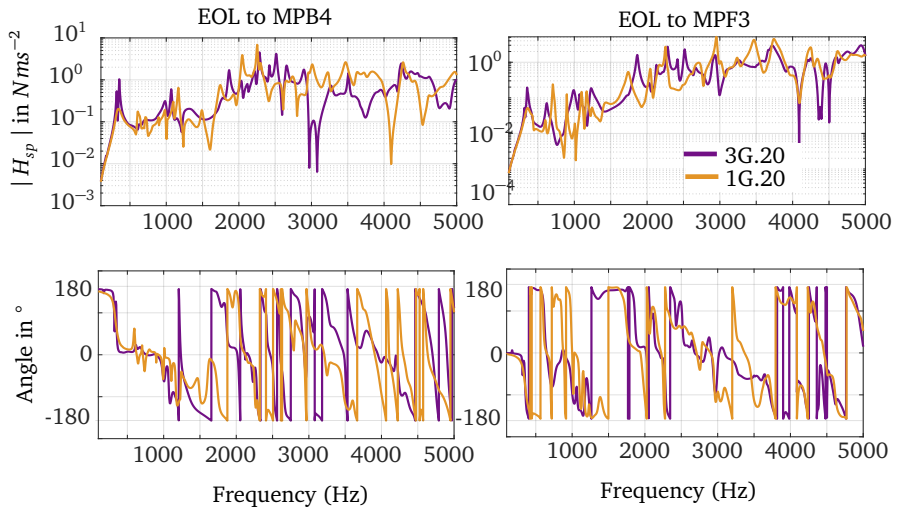


Figure 3.23: Secondary path responses between two different gearbox conditions 3rd gear 100Nm and 1st gear 20Nm

One strong benefit from developing the model especially for the development of an AVC is the invariance of the secondary path responses. The secondary path response is the vibration response obtained from a force input from one point on the gearbox to the mounting point where the vibration needs to be reduced which represents the actuator force transfer path. The force required for such an arrangement was already derived in Section 3.1.4. In the context of the prototyping gearbox only the load was the variation. However in a real operating gearbox the internal gear engagement is another variation. In Figure 3.23, the secondary path response is derived from say EOL point to both mounting point on transverse case MPB4 (left) and mounting point on the clutch case MPF3 (right). The response is plotted for two gear engagement conditions. It can be seen that there are minor deviations over the entire frequency range. Also the response of force applied by the actuator on transverse side produces lower response on the clutch side. This aspect is

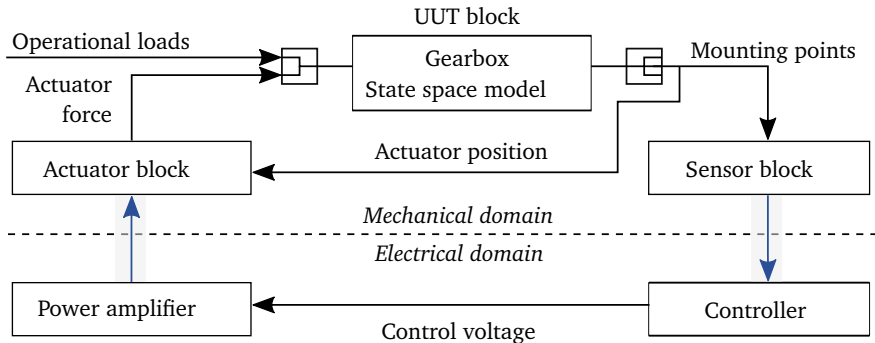


Figure 3.24: System Level model for evaluation of active vibration control system

further discussed in Chapter 5. The main takeaway here is that a single Romax model of the gearbox is sufficient to develop the AVC for the further steps.

3.3 System Level Simulation model

Once the model of the demonstration gearbox is established a System level Simulation (SLS) model as per the schematic shown in Figure 3.24 is developed. The SLS model enables one to verify performance against requirements and to optimize tunable parameters.

The preferred tool to implement this model is MATLAB owing to its wide variety of control simulation integration. A description of each of the blocks in the SLS model is provided below:

1. UUT block: Unit under Test - The state-space model of the gearbox, linearised for each operating condition is incorporated here.
2. Sensor block: This block converts the physical outputs of the model into sensor quantities. The sensor transfer functions can be incorporated here. The development of this block is presented in Chapter 4
3. Controller block: Various control strategies can be tested in this subsystem using the model outputs. This subsystem is useful for checking the influence of various tunable parameters of the implemented control algorithm for active vibration control.
4. Power amplifier block: In this thesis, the amplifier is modelled as simple gain. Power amplifiers are generally prone to electrical non-linearities, but these have not been studied as part of this thesis. A standard power amplifier, E-617 IVPZT

power amplifier from PI is used for the rest of this thesis. This amplifier possesses reasonable bandwidth the frequency range up to 5000Hz, hence a linear gain assumption would be sufficient.

5. Actuator block: Depending on the type of actuator employed, the dynamic behaviour of the actuator is modelled in this block. In Chapter 5, the developed model in the demonstration gearbox would be used in conjunction with the actuator model to derive a suitable location for it on the gearbox housing.

4 Sensor architecture

Sensors measure vibrations at the key locations of the object under study and keep track of the vibrations reduced. Sensing helps in calculating and evaluating the effectiveness of control system developed. From the review of various sensing principles presented in Section 2.4, alternative principles of vibration sensing as compared to accelerometers were identified. It was concluded that PVDFs and MFCs have comparable sensitivities, provide similar benefits like high contact area with the object under test, high flexibility and negligible mass loading effects. The MFCs were an economical option compared to PVDF. Hence, the development of the sensing architecture is based on MFCs as sensing elements. In this chapter the design of an economical sensing architecture for the active vibration control system along with the relevant signal electronics and calibration functions. Before proceeding to the details of the sensor design a sensing scheme describing the nature and positions of the gearbox vibration measurement is presented in the next section.

4.1 Sensing scheme for gearbox

It was assumed during the development of the model of the demonstration gearbox that the mounting points, that connect the transmission to the car body are not modelled in the study. A pragmatic approach needs to be taken to impose the limits on the extent of the system to be considered for vibration analysis due to economic aspects of testing.

The source of vibration here is the gearbox and the receiver is the mount as visualised in Figure 4.1. The force due to vibration transferred from the gearbox to the mount via the bolting interfaces is indicated by F_{mount} . One way of estimating this force is via the "blocked force" approach, by considering ideal rigid or free boundary condition at the connection interface of the transmission. The force estimated through this approach is independent of the receiver and is a characteristic of the source system itself. In NVH studies of automotive gearboxes, the blocked force approach was previously applied [26], and justifies the negligence of the fixtures and mounting components for vibration analysis. Another formulation in Transfer Path Analysis (TPA) called the "contact force" method exists, which is applicable only for specific fixtures and mounts. The estimated force is dependant on stiffness of the receiver (K_{mount}). Given the context of this work, the blocked force concept is the best choice given the conditions that a generic active vibration control concept independent of the car body dynamics is developed.

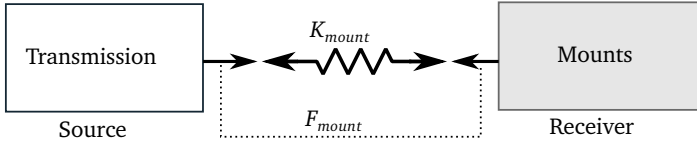


Figure 4.1: Source and receiver nomenclature for TPA of gearbox

Blocked force is estimated in two ways, by fixing the output points at the receiver end rigidly or by letting them free as shown in Figure 4.2. The free condition is much favoured over the rigid condition due to cost constraints and ease of implementation without manufacturing any additional fixtures. The blocking force in the free condition is evaluated by obtaining the transfer function at the mounting point location on the transmission H_{mount} multiplied with the free acceleration measured at the same position \ddot{x}_{mount} . Reduction in \ddot{x}_{mount} using the active vibration control system would directly reduce the force transferred to the impending mount at the attachment points, without having to obtain the FRF H_{mount} . Hence the sensors would be installed at the mounting positions directly to evaluate the free acceleration \ddot{x}_{mount} , which is the main objective for vibration reduction for the rest of this study.

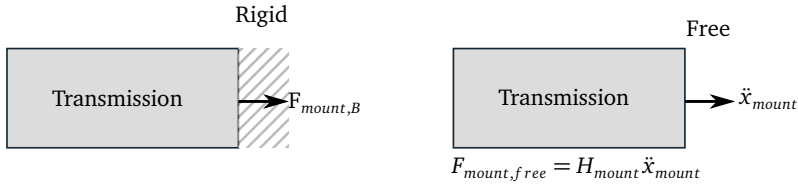


Figure 4.2: Rigid vs free boundary condition: Blocked force evaluation for TPA

4.2 Principle of operation of MFC

MFCs consist of alternating layers of PZT and epoxy layers in a single plane shown in Figure 4.3. This plane is sandwiched between a layer of interdigitated (equally spaced) metallic electrodes. It can function both as a sensor (direct piezoelectric effect) and as an actuator (inverse piezoelectric effect). For this study the MFCs are used as sensors, to effectively sense the vibration of the gearbox at the mounting points. Depending upon the polarization of the electrode layer, the MFCs can be classified into two major types: P1 and P2 as seen in Figure 4.4. The main difference between P1 and P2 type MFCs is the direction of polarization on the electrodes. In P1 MFCs the electrodes are polarized alternatively in the same plane, thus generating the polarization in the direction

of in-plane deformation. The P1 elements use the d33 effect, i.e the deformation is along the polarization of the active component. In contrast P2 MFCs operate on the d31 effect. They have the electrodes polarized normal to the direction of the thickness of sensor. As the in-plane deformation occurs, a voltage is produced across the composite.

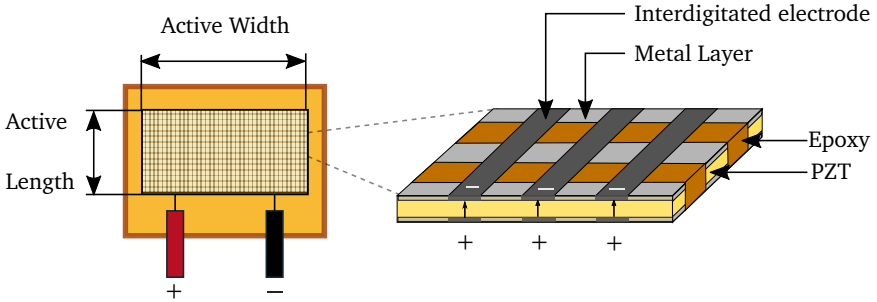


Figure 4.3: Schematic of an MFC adapted from [119]

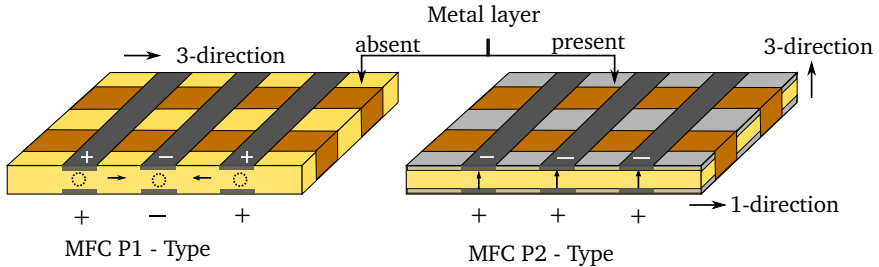


Figure 4.4: P1 vs P2 MFC schematic for sensing application. Cartesian coordinates local to each sensor are shown with 1 and 3

The physical behaviour of the direct piezoelectric effect can be written as follows

$$D_p = d_{pq}^T T_q + \epsilon_T E_q \quad (4.1)$$

where, p and q represent Cartesian directions in the composite, 1 and 3 indicated in Figure 4.4. D_p is the electrical displacement density (charge per unit area, expressed in C/m^2), d_{pq} is the piezoelectric constant that denotes charge generated per unit area in p -direction (expressed in C/N), per unit stress in q -direction denoted by T_q (expressed

in N/m^2). ϵ_T is the dielectric constant (permittivity) under constant stress T in the p -direction and E is the electric field expressed in V/m ; in the case of a sensor this is zero;

One must note that the directions in the piezo-composites of P1 and P2 type differ. In MFC type P1, the 3-direction is denoted by the piezoelectric fibre direction, which is also the direction of electrodes with alternating polarity. On the other hand the P2 MFC is polarized across its thickness which is the 3-direction for this MFC. The strain experienced by the sensors is in the planar direction (or plane strain condition); hence the d_{33} effect is active for the P1 MFC and d_{31} effect for the P2 MFC.

The vibration signal is normal to the surface causing local bending of the surface that transforms into in-plane strains of the plate-like MFC structure causing a voltage output. The charge sensitivity, i.e. the amount of charge produced per area for each of the MFC type can be calculated using the following formulae substituting $E_3 = 0$:

$$\begin{aligned} D_3^{P1} &= d_{33} T_3 \\ &= d_{33} (Y_3 S_3) \\ D_3^{P2} &= d_{31} T_1 \\ &= d_{31} (Y_1 S_1) \end{aligned} \tag{4.2}$$

where, Y_3 and Y_1 represents the Young's modulus in the fibre direction for P1 and P2 MFC respectively. For charge density per unit strain S_1 and S_3 , can be substituted as 1. The table of properties and calculated charge densities are given below for the smallest size offering of MFCs from the Smart-Material catalogue. The company Physik Instrumente (PI) also offers only one particular MFC model in their product line. The P878 sensor from PI is of P1 type with dimensions 27 mm. The cost is almost three times higher compared to similar offerings from Smart Material MFCs. Hence, for further analysis, the MFCs from Smart materials have been considered.

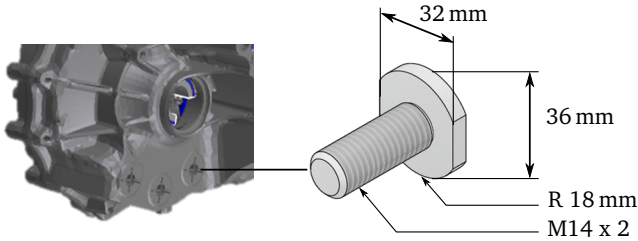


Figure 4.5: Mounting cap on demonstration gearbox for sensor mounting

The sensors would be assembled on the mounting cap shown in Figure 4.5 on the demonstration gearbox. The vibration at the mounting point is transmitted through the mounting screw which is a standard M14 screw. Hence, the MFCs with dimensions of

Table 4.1: Comparison of P1 and P2 type MFCs

Property	MFC type P1	MFC type P2
Market Name	M2814P1	M0714P2
d_{33}	400 pC/N	-
d_{31}	-	170 pC/N
Young's Modulus	Y_3	Y_1
	30.3 GPa	
Active length (l_{MFC})	25 mm	14 mm
Active width (b_{MFC})	14 mm	7 mm
MFC length	38 mm	16 mm
MFC Width	20 mm	16 mm
Charge Density per unit area per unit strain	D_3^{P1}	D_3^{P2}
	0.012 $\mu\text{C}/\text{m}^2$	0.005 $\mu\text{C}/\text{m}^2$

14 mm are compared against each other. Unfortunately, same length of MFCs are not available. Hence, the 28 mm M2814P1 MFC is chosen for comparison.

Using the values charge density per unit strain from Table 4.2 it is clear that the charge produced by P2 even for the same active area would be 57.5% lesser than the P1 type MFC. The size of the mounting point area is also important to consider. The MFC M0714P2 would be ideal to use given the dimension is perfect for the mounting screws installed on the gearbox shown in Figure 4.5. Smaller area of the MFC can also lower the strain averaging across the MFC and capture localized vibration. No P1 MFC in the required dimension of the mounting point screw is readily available. Custom order of P1 sensors for the given dimension of the application in this thesis would have incurred extra costs, hence P2 was used for the rest of this study.

The reduced charge density from choosing the P2 compared to a similar dimension of P1 sensor can be mitigated by carefully designing an appropriate signal conditioning unit, which described in the following section.

4.3 Design of the signal conditioning for MFCs

The nominal surface displacement produced by a vibrating complex structure such as the gearbox at high frequencies are typically in the range of a few micrometers [104] which would produce a small charge on the MFC electrodes for measurement. Hence, a signal-conditioning unit needs to be built to convert the charge into a measurable quantity to measure the high frequency vibrations produced in the gearbox.

An electrical model of the MFC can be assumed to be a strain dependent charge source which is in parallel with a capacitance as seen in Figure 4.6. This capacitance is that of the piezoelectric element in the sensor and let this capacitance be called C_s . To avoid any

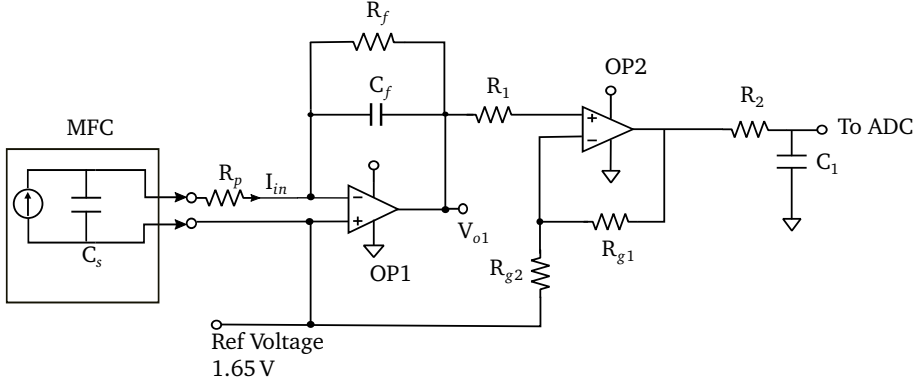


Figure 4.6: Circuit of signal conditioning unit

high frequency noise a resistance R_p can be placed in series with it to generate a high-pass filter with cut-off frequency $f_{ch} = \frac{1}{2\pi R_p C_s}$.

The signal conditioning circuit has two amplifying stages which are implemented using Operational Amplifiers (Op-Amps). The first one is a charge amplifier OP1 in combination with capacitor C_f and feedback resistance R_f . In the absence of a feedback resistance, the capacitance C_f produces an output voltage proportional to the instantaneous current coming through OP1.

$$V_{o1} = \frac{1}{C_f} \int -I_{in} dt \quad (4.3)$$

In this ideal case shown in Equation 4.3 the input bias current I_{in} charges up the capacitor which eventually saturates OP1. To avoid this, the feedback resistor R_f is added to provide a discharge path for the current. Adding a feedback resistance in parallel also acts as a low pass filter for the signal conditioning circuit with cut-off frequency $f_{cl} = \frac{1}{2\pi R_f C_f}$.

The final output of the signal conditioning is fed to a microcontroller for data acquisition and processing. Since negative inputs cannot be handled by the Analog-to-Digital Converter (ADC), the zero is shifted to 1.65 V as shown in Figure 4.6. The final output voltage from OP1 is given by:

$$V_{o1} = 1.65 - \frac{1}{C_f} \int I_{in} dt \quad (4.4)$$

The second Op-Amp is a non-inverting voltage amplifier with gain that is adjusted by

the two resistances R_{g1} and R_{g2} . The gain of this stage is given by:

$$G_{OP2} = 1 + \frac{R_{g1}}{R_{g2}} \quad (4.5)$$

The choice of R_{g1} and R_{g2} depends on the amount of gain required to have a measurable signal in the given ADC output range. In this case 0 - 2.5V. The final output at the ADC is obtained by $V_{o1} \times G_{OP2}$.

4.4 Calculation of parameters of signal conditioning

The capacitance of the MFC0714P2 sensor is 11 nF. The R_p is chosen in such a way that it has similar high frequency impedance ($1/\omega C_s$) up to 12000Hz which is equivalent to 1 k Ω . The high-pass frequency f_{ch} for the given values is 14.5 kHz.

The sensitivity of the MFC sensor can be derived by expanding the charge density D_1^{P2} given in Equation 4.2. Multiplying the charge density with the active area of the MFC0714P2 based on the dimensions given in Table 4.2 gives the charge generated q_{MFC} per unit strain ($S_1 = 1$), the quantity can be called as charge density.

$$\begin{aligned} D_1^{P2} &= d_{31} Y_1 \\ q_{MFC} &= (l_{MFC} b_{MFC}) d_{31} Y_1 \\ V_{sens} &= \frac{l_{MFC} b_{MFC} d_{31} Y_1}{C_s} \end{aligned} \quad (4.6)$$

In the above equation, the charge sensitivity of MFC is converted to voltage sensitivity by dividing the charge by capacitance of the sensor C_s . Substituting the respective quantities, the voltage sensitivity is 505 pC/ppm. Here *ppm* is measure of strain on a scale of 10^{-6} .

The output voltage swing is defined as the positive and negative voltage range with respect to the reference voltage, here 1.65V. In the given set-up the ADC used is a 12-bit AD7928 from Analog Devices. It has a maximum voltage readout of 2.5V. The positive voltage swing, ΔV_{pos} is $2.5V - 1.65V = 0.8V$. The negative voltage swing, ΔV_{neg} is $1.65V - 0V = 1.65V$. The limit of the positive voltage swing can be used to calculate the feedback capacitance C_f using the voltage sensitivity as follows:

$$C_f = V_{sens} \frac{\Delta S}{\min(\Delta V_{neg}, \Delta V_{pos})} \quad (4.7)$$

The range of strain for which the MFC needs to be designed is denoted by ΔS . The modal strain ranges for aluminium structures about 3 mm thick would range in the order of 1 ppm. ΔV is the minimum value of the output voltage swing here: 0.8V. The calculated value of C_f is 500 pF.

The value of feedback resistance is determined by the desired low cut-off frequency f_{cl}

as described in the previous section. For this sensing scheme, 100 Hz has been chosen as the low-pass frequency to eliminate the electrical noises of 50 Hz and its second harmonic. Using this value and low pass frequency, the value of C_f , the feedback resistance R_f is 20 M Ω .

The choice of the combination of R_{g1} and R_{g2} is determined by the gain required at the output to remain within 0 - 2.5 V as this was the readable voltage limit for the ADC. The value of gain of 4/3 was set for G_{OP2} , with the choice of $R_{g1} = 10$ k Ω and $R_{g2} = 30$ k Ω .

The R2 /C1 filter at the sensor output restricts the bandwidth of the sensor output to 12.5 kHz with $R_2 = 3$ k Ω and $C_1 = 4.7$ nF. The sampling of the data in this work would be performed at 20 kHz, hence this low pass filter serves as an anti-aliasing filter at 10 kHz.

Table 4.2: Summary of electrical quantities of the signal conditioning unit

C_s	R_p	R_f	C_f	R_1	R_{g1}	R_{g2}	R_2	C_1
11 nF	1 k Ω	20 M Ω	500 pF	270 Ω	10 k Ω	30 k Ω	3 k Ω	4.7 nF

The data with the MFC sensor is collected with the help of an integrated microcontroller board designed in conjunction with the signal conditioning circuit described and is shown in Figure A.1 in Appendix A.2. The Teensy 4.1 microcontroller development board is integrated into the DAQ board that is responsible for data acquisition and also implementing the control algorithm. The control algorithm aspect is discussed in detail in Chapter 6.

4.5 Calibration of the MFC sensor

The output of sensor at the end of the signal conditioning circuit is a voltage as a consequence of the local strain experienced by the sensor due to vibration of the gearbox. A meaningful physical quantity needs to be associated with the acquired voltage. As seen in the review of the literature of vibration sensors, accelerometers are widely used in quantifying the vibration in structures. The aim of this section is to establish a relationship of the MFC sensor voltage with a standard accelerometer output so that voltage read out in the signal conditioning unit can be quantified in terms of local acceleration as a direct measure of vibration.

The calibration of sensors is done according to the ISO-16063-21 standard [93], using the method of comparison with a reference transducer. One aspect of this calibration procedure is the excitation itself, which is done with a sine wave. The standard is valid for frequency range 0.4 Hz to 10 kHz. In the case of using MFCs for quantifying gearbox vibration, the calibration needs to be done over the frequency range of interest i.e. 0 - 5000 Hz so that the quality of the vibration signal is preserved for the design of an AVC system.

Calibration of non-standard sensors such as MEMS is performed in the past, for example [23], using the standard calibration procedure but with non-standard excitation like multi-sinusoidal input. Hence, it is proven that the calibration can be done over a wide variety of excitations.

The calibration of MFCs by comparison with an accelerometer involves generating a transfer function between the voltage obtained by accelerometer and that of MFC. The calibration is performed directly on the 7HDT300 gearbox mounted in the IMS Connect set-up discussed in the previous chapter. The obtained transfer function is then studied for deviation with the nominal sensitivity.

To understand the nature of transfer function obtained between accelerometer and MFC signals, the dynamics and electromechanical relations are theoretically derived. The schematic of a standard piezoelectric accelerometer is shown in Figure 4.7. The accelerometer compared here is Kistler 8640A5T as described in Appendix A, and which was already used in Chapter 3 for the correlation experiments. It is an IEPE (Integrated Electronics Piezoelectric) Accelerometer that has the signal conditioning electronics built into the accelerometer housing and hence can directly provide with voltage output when powered with a signal amplifier.

The local deformation of the object of study (here, the gearbox), is denoted by x_g . x_{ac} denotes the movement of the seismic mass m_{ac} . It is assumed that the accelerometer is rigidly attached to the test-object neglecting the effects of the glue or any attachment mechanism. Hence x_g is considered directly as the displacement of the accelerometer base. The movement of mass, m_{ac} relative to the base causing a charge to be generated across the piezoelectric element following the direct piezoelectric effect given by Equation 4.1. Standard IEPE sensors have integrated electronics directly converting this to a readable voltage output. The accelerometer internal characteristics such as stiffness k_{ac} and damping c_{ac} determine the bandwidth of operation.

The equations of motion of the accelerometer are given by the following equation:

$$\ddot{x}_{ac} + \frac{c_{ac}}{m_{ac}}(\dot{x}_{ac} - \dot{x}_g) + \frac{k_{ac}}{m_{ac}}(x_{ac} - x_g) = 0 \quad (4.8)$$

A variable u is introduced, denoting the relative displacement of the combination of accelerometer attached to the gearbox i.e. $u = x_{ac} - x_g$. The Equation 4.8 can be re-written by subtracting \ddot{x}_g on both sides as:

$$\ddot{u} + \frac{c_{ac}}{m_{ac}}(\dot{u}) + \frac{k_{ac}}{m_{ac}}(u) = -\ddot{x}_g \quad (4.9)$$

The charge generated by the piezoelectric element in the accelerometer is proportional to the relative displacement u . S_{qac} denotes the nominal sensitivity of the accelerometer. It includes the transfer behaviour between the charge output to the final voltage readout $V_{acc}(s)$, where $s = j\omega$ and $j = \sqrt{-1}$. This sensitivity also includes the transfer behaviour of the IEPE electronics in the accelerometer. typically for commercial accelerometers

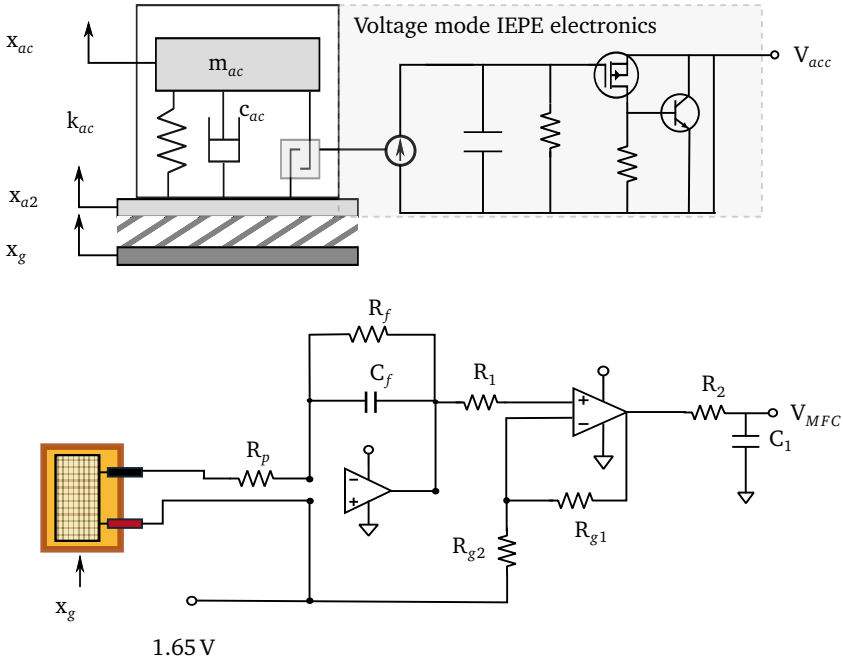


Figure 4.7: Schematic depicting the measured quantities of accelerometer (top) vs MFC (bottom)

this is constant over the frequency range of interest, therefore it is treated as a constant here. Hence, Equation 4.9 rewritten in frequency domain including the sensitivity transfer function as:

$$\begin{aligned}
 (s^2 + P_a s + Q_a)U(s) &= -s^2 X_g(s) \\
 (s^2 + P_a s + Q_a) \frac{V_{acc}(s)}{S_{qac}} &= -s^2 X_g(s) \\
 V_{acc}(s) &= \frac{-s^2 X_g(s) S_{qac}}{s^2 + P_a s + Q_a}
 \end{aligned} \tag{4.10}$$

The mass, stiffness and damping coefficients are absorbed into unknown parameters P_a and Q_a , which are identified via calibration.

Next for the derivation of equations of motion for MFC, Equation 4.2 serves as a starting point. The voltage generated at the sensor output before connecting to signal conditioning

for strain S_1 is transformed frequency domain by applying the Laplace transformation on both sides. The strain is directly related to local displacement of the object on which the MFC is attached, here x_g . Additionally the final voltage output read by the MFC involves the transformation of the voltage to a read-out voltage through the signal conditioning unit. Let H_{sc} represent the electrical transfer function of the signal conditioner. Hence, the Equation 4.6 it can be rewritten as:

$$V_{MFC}(s) = \frac{l_{MFC} b_{MFC} d_{31} Y_1}{C_s} H_{sc}(s) X_g(s) \quad (4.11)$$

By using equations 4.10 and 4.11, one can formulate a transfer function that predicts the voltage generated by the accelerometer using the MFC voltages in frequency domain by the following equation:

$$V_{acc}(s) = \frac{G_s s^2}{H_{sc}(s)(s^2 + P_a s + Q_a)} V_{MFC}(s) \quad (4.12)$$

The transfer function $H_{sc}(s)$ is approximated to the a single pole low-pass filter output of the gain OP2 in the signal conditioning circuit. Hence a cubic order in the numerator occurs as

$$V_{acc} = \frac{G_s (s^3 + L_m s^2 + M_m s + N_m)}{s^2 + P_a s + Q_a} V_{MFC} \quad (4.13)$$

The second order dynamics in the denominator is due to the accelerometer seismic mass. The parameters of the transfer function are identified using experimental data and is describe in the following section.

Identification using gearbox vibrations

For this calibration study, the demonstration gearbox is the object under study to measure the vibration at first the reference EOL position and mounting point MPF3 as indicated previously in Figure 3.15. The demonstration gearbox was ramped up in speed from 0 - 5000 RPM for the calibration process to identify the transfer function in Equation 4.12. This experiment is repeated by installing the MFC in place of the accelerometer for both of the measurement positions to perform system identification between the measured sensor voltage signals. The accelerometer data was sampled at 25.6 kHz, using a standard data acquisition system, here Soundbook MK2. While the MFC data is acquired at 20 kHz due to performance limits in the microcontroller.

In total 24 speed ramp cases were used in deriving the fitting function. Measurement at 2 points, 3 different gear engagements and 4 torque levels. This is done to obtain a transfer behaviour of the accelerometer invariant to the point at which the vibration is measured and the loading conditions. For validation, steady state data i.e. single torque and speed data is used to check if the gear mesh frequencies can be predicted using the calibrated MFC.

Table 4.3: Testing matrix for MFC calibration study

Gear engaged	Input torque (Nm)	Measurement point
1	0	EOL
2	20	
	50	MPF3
3	100	
Total 24 experiments used for identification		

The voltage output of both the sensors (accelerometer and MFC) is used to identify transfer function, that fit the data as described in Equation 4.12. The identification of parameters in Equation 4.13 is performed in frequency domain. The summary of identified parameters in Equation 4.13 is shown in Table 4.4.

Table 4.4: Summary of parameters MFC Calibration

G_s	P_a	Q_a	L_m	M_m	N_m
0.018	6054.06	474.41	8017.97	535.03	486.51

The prediction accuracy at both points EOL and MPF3 for 3rd gear are shown as in Figure 4.8. It can be seen that the identified transfer function can help predict the relevant peaks (resonances) of the housing structure using the speed ramp experiments.

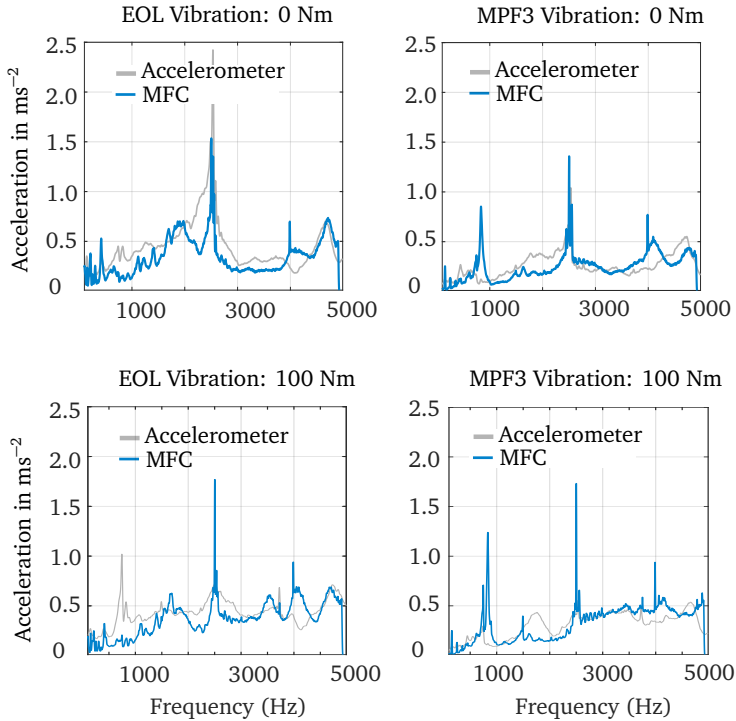


Figure 4.8: Predicted acceleration from MFC values for 3rd gear; 0Nm (top); 100Nm (bottom)

Same trends are observed at even the 2nd gear. The trend of increasing vibrations with speed are appropriately captured. There are slight uncertainties in the EOL vibration prediction around 500 - 1000Hz.

Relevant gear mesh frequencies can be accurately measured using the MFC sensors at both locations when the gearbox is run under steady state at constant input load and speed. For example as shown in for 1st gear 3000RPM and 100Nm input torque, gear mesh frequencies 608Hz, 1216Hz, 1824Hz.. and so on can be easily identified.

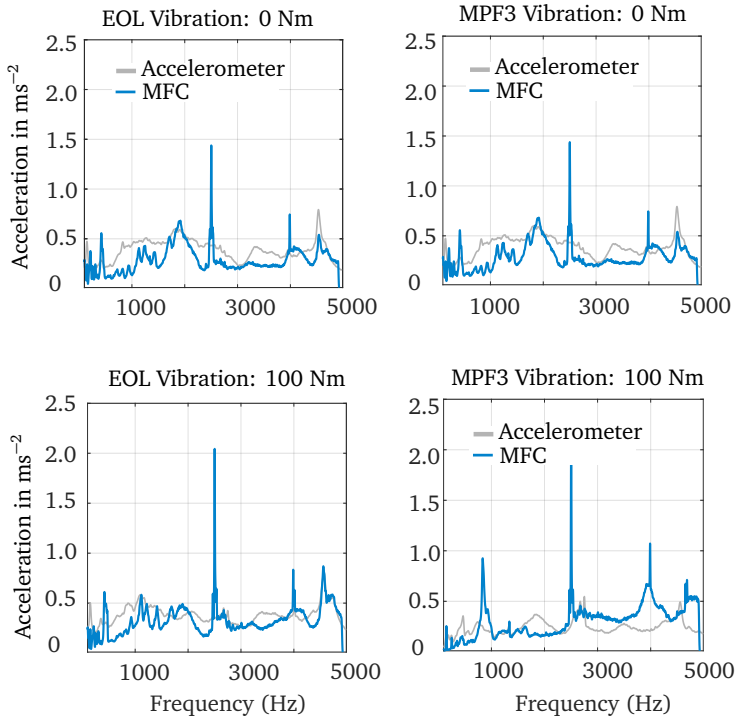


Figure 4.9: Predicted acceleration from MFC values for 2nd gear; 0Nm (top); 100Nm (bottom)

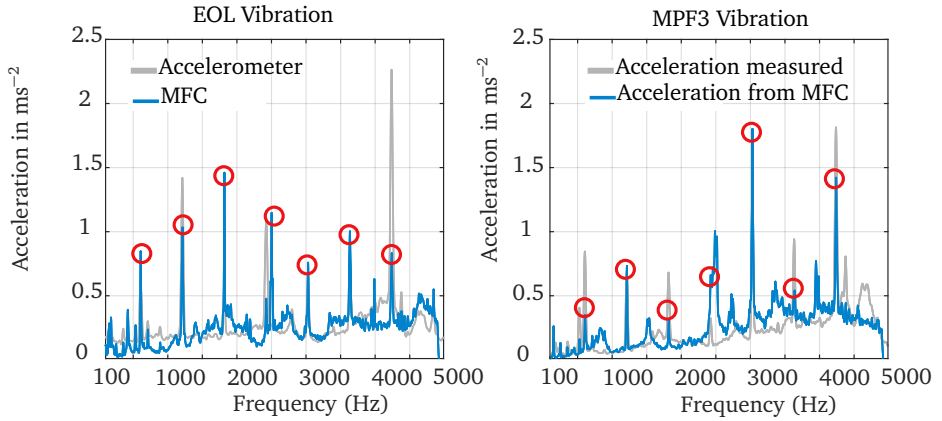


Figure 4.10: Predicting gear mesh frequencies at steady state - 1st gear 3000 RPM and 100Nm input torque

Hence the identified transfer function to convert the MFC voltage into acceleration which is sufficiently accurate to capture the vibration behaviour of the gearbox housing. This transfer function is invariant to position of the sensor, gear engagement and operating conditions of the gearbox.

The transfer function identified for the MFC sensor is used to identify the secondary path transfer functions for the demonstration gearbox in the next chapter. Seven mounting points (shown in Figure 4.11 and Figure 4.12 on the demonstration gearbox) were equipped with MFCs. The mounting positions on the clutch case are coded as MPF and those on the transverse case are coded as MPB. These sensors record the actuator influence to derive a suitable actuator position as described in the next chapter. The installation of MFCs is carefully done using Kapton tape and high strength glue at the desired locations on the mounting caps shown in Figure 4.5. Coaxial cables are used to minimise data corruption.

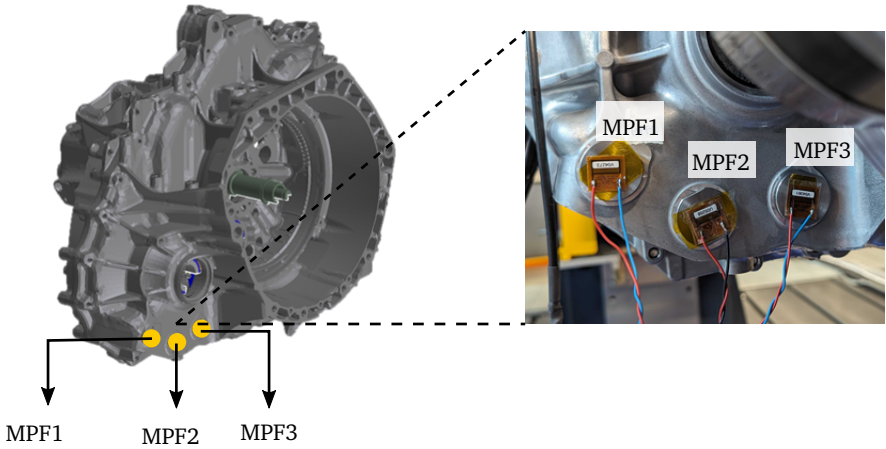


Figure 4.11: Mounting positions with MFCs on the clutch case (coded as MPF) of 7HDT300

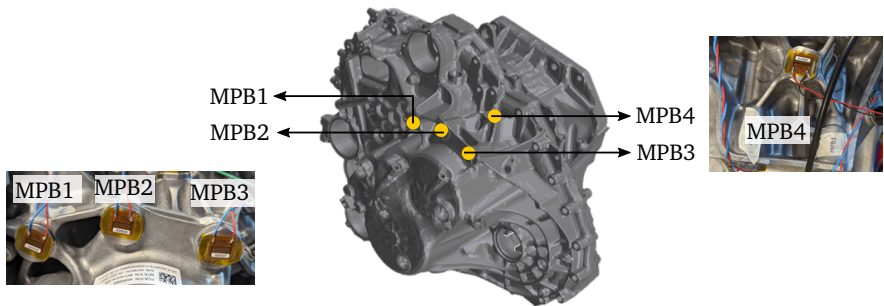


Figure 4.12: Mounting positions with MFCs on the transverse case (coded as MPB) of 7HDT300

5 Strategy for actuator placement

With the conclusion of the actuating principle and the force requirement from Section 3.1.4 for the active vibration control system, an inertial mass actuator shown in Figure 5.1 was designed. The details of the design are presented in the publication of Okda et al. [104] and the actuator specifications can be referred in Appendix A.1. The actuator has a dimension of $\phi 25 \text{ mm} \times 20 \text{ mm}$ and weighs 59.6 g. The concept of the inertial mass actuator on the gearbox housing for vibration control of one mounting location on the rear case was validated. The ability of the actuator to cancel the vibration at the desired location is defined in a frequency range termed as controllability. This concept was introduced in Section 2.5.1.

In the prototype gear gearbox, the sensitivity of the actuator position was discovered. Due to the operation at high frequency range, the controllability of the actuator varied highly from one point to another. The location of the actuator was decided based on the modal controllability concept proposed in Section 5.2. Misplaced actuators can lead to a lack of controllability, hence a careful optimisation of the position is required. The goal is to control the vibration at the mounting locations of the gearbox. In Figures 4.11 and 4.12, it can be seen that a total of two mounting frame locations exist, one on each side of the housing. In total seven mounting points are indicated. To obtain maximum cancellation of vibration, each of the points can be equipped with an actuator also termed as a collocated system. But from a system-level point of view, the actuator and its associated power amplifier are the most cost intensive components and equipping each individual mounting point would increase the cost of the system by seven-fold. This is further discussed in

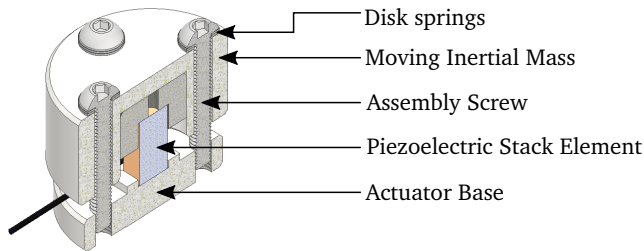


Figure 5.1: Inertial mass actuator designed for gearbox housing vibration control [104]

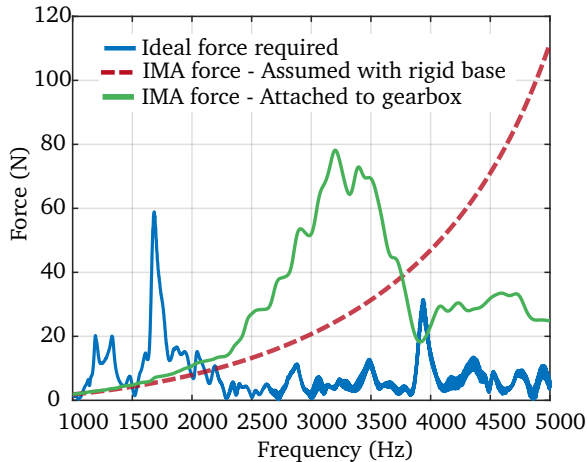


Figure 5.2: Effective force of IMA Ideal rigid base vs mounted on gearbox [104]

Chapter 8. Hence, there is a strong need to minimize the number of actuators, and place them at suitable position on the gearbox to achieve maximum vibration controllability at the mounting points. In this chapter, a suitable placement criteria to obtain actuator position is derived. Then based on the needs of current active vibration control system a decision about the optimal actuator location and the total number of actuators for the gearbox in operation i.e. the demonstration gearbox is proposed.

Before proceeding to the actuator placement strategy, it is important to understand the need to consider the coupling of actuator dynamics with the object on which it is mounted. The designed inertial mass actuator when mounted on a rigid base produces an inertial force (for max 120V power supplied) similar to that of a 2-DOF system, represented by the red dotted line in Figure 5.2. When the same force is derived by replacing the base with the gearbox housing, dynamics of the housing get coupled modifying the force response. This force response varies with the position of actuator on the gearbox housing across the frequency range. For example, there is a decreased effective force from the ideal force response in the region > 3800 Hz, where more power to the actuator is needed or simply no further reduction is possible due to limitation on power supplied from the amplifier.

This figure summarizes the main reason why the actuator dynamics should be taken into account for optimising its location. There is no specific order followed in literature related to the design of the actuator and then the position optimization or vice versa. Many studies have reported fixing the actuator position first and then designing the suitable

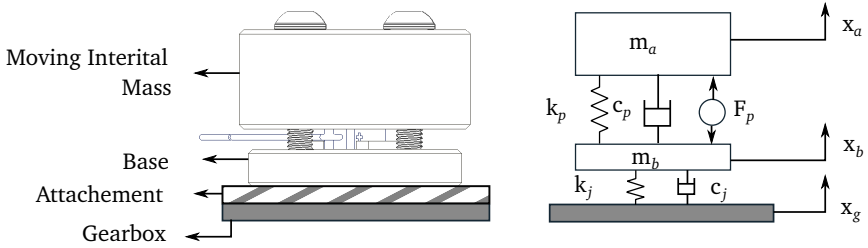


Figure 5.3: Two DOF schematic of the designed IMA

actuator. In this thesis, the goal was to have a modular design for an actuator that can be used on various improvements to the series production gearbox. For example, the gearbox housing geometry of the 7HDT300 has minor modifications from its predecessor 7DCT300. Hence, a new design of the actuator is not required, rather only an alternate position or altering the number of actuators would be sufficient to easily upgrade the active vibration control for the next generation product.

5.1 Coupling of actuator dynamics with gearbox housing

In the system level simulation model of the Demonstration gearbox introduced in Section 3.3, the block for actuator model is now used to couple the actuator dynamics with the position of attachment on the gearbox housing. The output velocity and displacement DoF is attached to the relevant point on the gearbox housing.

The model of the inertial mass actuator is a 2-DOF model shown in Figure 5.3. Each each DOF is related to the two masses present i.e. the top moving mass, m_a and the base, m_b respectively. The stiffness k_p is the piezoelectric stack element stiffness and the c_p is its associated damping. The stiffness at the attachment point between the IMA base and the gearbox is represented with k_j and c_j . The equation of motion for the IMA can be given as follows:

$$\begin{aligned}
 m_a \ddot{x}_a + c_p(\dot{x}_a - \dot{x}_b) + k_p(x_a - x_b) &= F_p \\
 m_b \ddot{x}_b + c_j(\dot{x}_b - \dot{x}_g) + k_j(x_b - x_g) &= -F_p + c_p(\dot{x}_a - \dot{x}_b) + k_p(x_a - x_b) \\
 &= -m_a \ddot{x}_a
 \end{aligned} \tag{5.1}$$

The force generated by the piezoelectric stack element in response to an external voltage V_{IMA} supplied by a power amplifier is denoted by F_p . It is a function of the piezoelectric

constants and dimensions of the actuator given by:

$$F_p = \frac{d_{33} n_A A_A}{l_A s_{33}} V_{IMA}, \quad (5.2)$$

Where A_A is the actuator cross-sectional area, n_A is the number of piezoceramic layers, l_A is length of the actuator, d_{33} is the piezoelectric charge constant for the longitudinal direction, and s_{33} is the mechanical compliance in the longitudinal direction. The constant K_e is used to denote the fraction $\frac{d_{33} n_A A_A}{l_A s_{33}}$. The reaction force of the IMA is represented by F_a , which is the resultant control force that would be used to counteract the vibration at the desired point in the gearbox housing. Rearranging the equations in 5.1, the reaction force is given by:

$$\begin{aligned} F_a &= -c_j(\dot{x}_b - \dot{x}_g) - k_j(x_b - x_g) \\ &= m_a \ddot{x}_a + m_b \ddot{x}_b \end{aligned} \quad (5.3)$$

It can be seen that the effective control force to the gearbox from IMA depends on the motion of the attachment point. Hence the control force of the actuator is coupled and not independent from the dynamics of the gearbox. This explains the deviation of force response from the ideal behaviour as indicated in Figure 5.2.

To validate the dynamic behaviour of the IMA with the demonstration gearbox, the coupled model is built for candidate points shown in Figure. 5.4. The gearbox housing DoFs are coupled in the system level model using the equations presented above to obtain the coupled secondary path transfer responses of the IMA. The response of the secondary path is the FRF obtained between the voltage supplied to the power amplifier to the resultant vibration produced at the mounting point sensors of the gearbox housing. Vibration is quantified with acceleration measured using the calibrated MFCs.

The system level coupling is validated experimentally by mounting the designed IMA at various possible mounting points. The IMA is then supplied with a sine sweep voltage with frequency varying from 100 Hz – 5000 Hz from the power amplifier. The secondary path responses are recorded at the seven mounting points of the demonstration gearbox on the clutch and transverse case previously indicated in Figures 4.11 and 4.12. The maximum voltage that can be supplied to the IMA is 150 V.

A quick check on linearity in the secondary path dynamics is performed by exciting the IMA with different voltage levels and checking the FRFs at different mounting points. The voltage supplied over time t to the IMA is given by:

$$\begin{aligned} V_{IMA} &= V_{DC} + \frac{V_{PP}}{2} \sin(2\pi\omega t), \omega \in [100 \text{ Hz}, 5000 \text{ Hz}] \\ V_{DC} &= \frac{V_{PP}}{2} \end{aligned} \quad (5.4)$$

In Equation 5.4, V_{DC} , is the DC offset voltage supplied to IMA for operation and is adjusted with the operational peak - peak voltage. The power amplifier is modelled as a simple

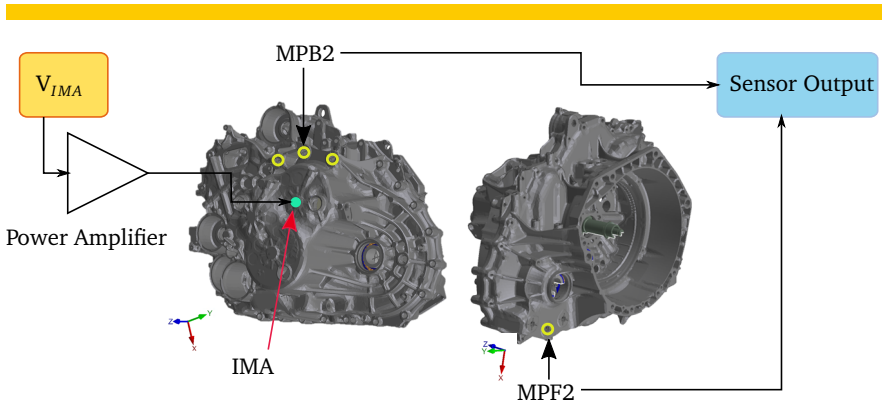


Figure 5.4: Transfer function schematic of the actuator coupled model - Blue dot indicates Position 4

gain and accounts also for the conversion of voltage to required force F_p .

As seen in Figure 5.4, the secondary path is measured by mounting the IMA on a point on the rear case of the housing and the responses are measured on the front and back mounting points. With the increase in voltage supplied to actuator, the FRF remains fairly unchanged in terms of phase indicating that the linearity of the secondary path is a valid assumption in the given voltage and frequency range of operation. This is useful for the control development as the secondary path phase is an important parameter in the FxLMS algorithm as discussed in Section 2.7. A decrease in the response at high voltage supply i.e. 120V is due to the decrease in the d_{33} due to increasing DC offset as given by Equation 5.4. This effect has been reported as a general behaviour for piezoelectric materials [11, 83]. The slight drop in the output response is compensated by the controller to set a suitable voltage level. Since the phase is unchanged for various voltage levels, the 40 V response is used for further actuator placement evaluations in this chapter.

From Chapter 3, it was shown that for secondary path modelling, a single model is sufficient which is not affected by the gear engagement and loading condition of the transmission. Hence this model can be used for correlating the actuator coupled dynamics to get a suitable actuator position.

For the correlation of actuator coupled model, the displacement, velocities of the connecting DOF is coupled to the IMA via k_j and c_j in the system level model in Figure 3.24. Eleven points shown in Figure 5.6, are shortlisted to explore an actuator position based on two criteria. The first criteria is the physical proximity of the IMA position to the mounting points. This would ensure the secondary path response would be sufficiently high compared to an IMA placed far away from the desired control location. The second criteria is the ease of integrating it to the housing structure at flat bases congruent to the

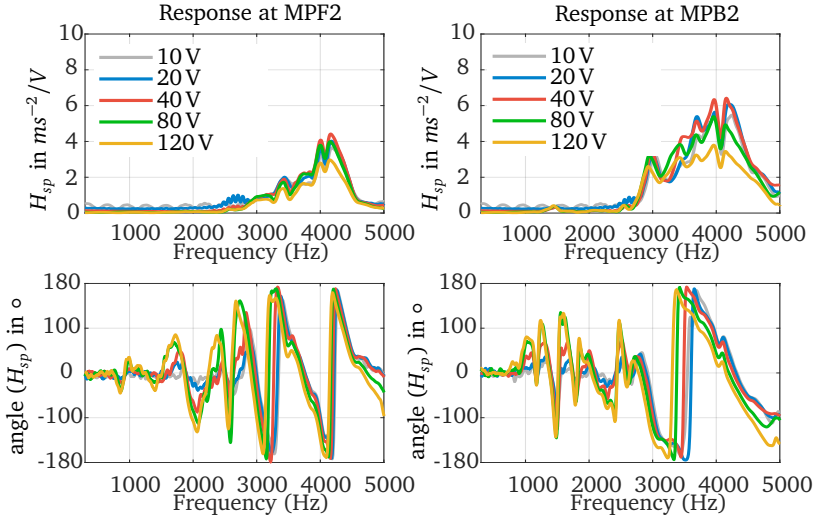


Figure 5.5: Linearity check for secondary path response of designed actuator on demonstration gearbox

base of the IMA.

The correlation of responses between experiment and simulated values for the secondary path responses was performed using the correlated model with identified damping values of the demonstration gearbox from Romax. Two additional parameters influence the prediction of the secondary path responses here, the joint stiffness k_j and the damping ratio c_j at the attachment point. The value of K_e is calculated to be 5 N/V and is kept constant through out the identification and for different voltage levels despite the slight deviations observed in d_{33} as mentioned before due to the nature of DC bias provided.

The joint stiffness and damping ratio has been generalised in the range of both the cases (clutch and transverse) of the gearbox. A general trend observed was that lower joint stiffness values provided better fits to the secondary path responses for the IMA positioned on the clutch case compared to the transverse case. The values considered for the identification procedure are given in Table 5.1.

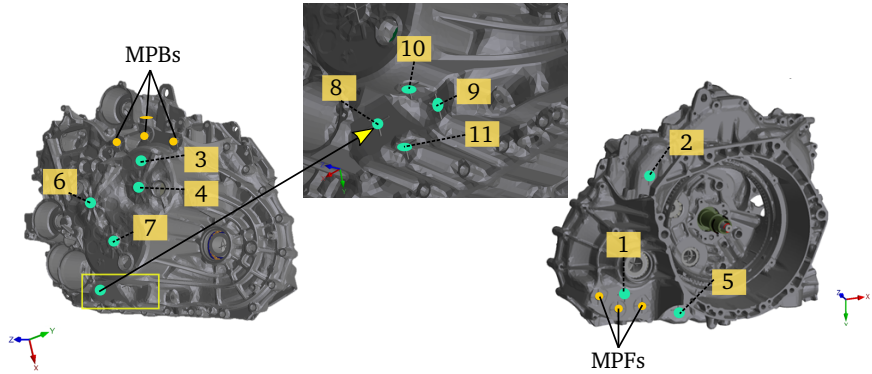


Figure 5.6: Positions of IMA location search on the gearbox indicated by blue circles; Yellow dots indicate the sensor positions MPFs- Mounting points on front side (clutch case); MPBs - mounting points on back side (transverse case)

Table 5.1: Summary of parameters IMA coupling

Parameters	k_j	c_j	K_e
Clutch case	3×10^7 N/m	500 Ns/m	5 N/V
Transverse case	3×10^{10} N/m	500 - 1000 Ns/m	

It is to be noted that there will be some change in modal damping values tuned from the Romax model due to the coupled dynamics, but overall the modal damping ratios remained fairly the same. The joint stiffness and the damping ratios were more sensitive to set the level of predicted responses from the coupled model.

It can be observed in Figure 5.7 that due to coupling of the actuator dynamics, all frequencies cannot be controlled to equal degree even with maximum power supplied to the actuator. Hence, a suitable position for the actuator is required, so that the secondary path transfer function can have good magnitude in the required frequencies at which maximum structure-borne transfer at the mounting points occurs. For this it is necessary to first establish a placement criteria, which will serve as the objective for finding a suitable position for the actuator.

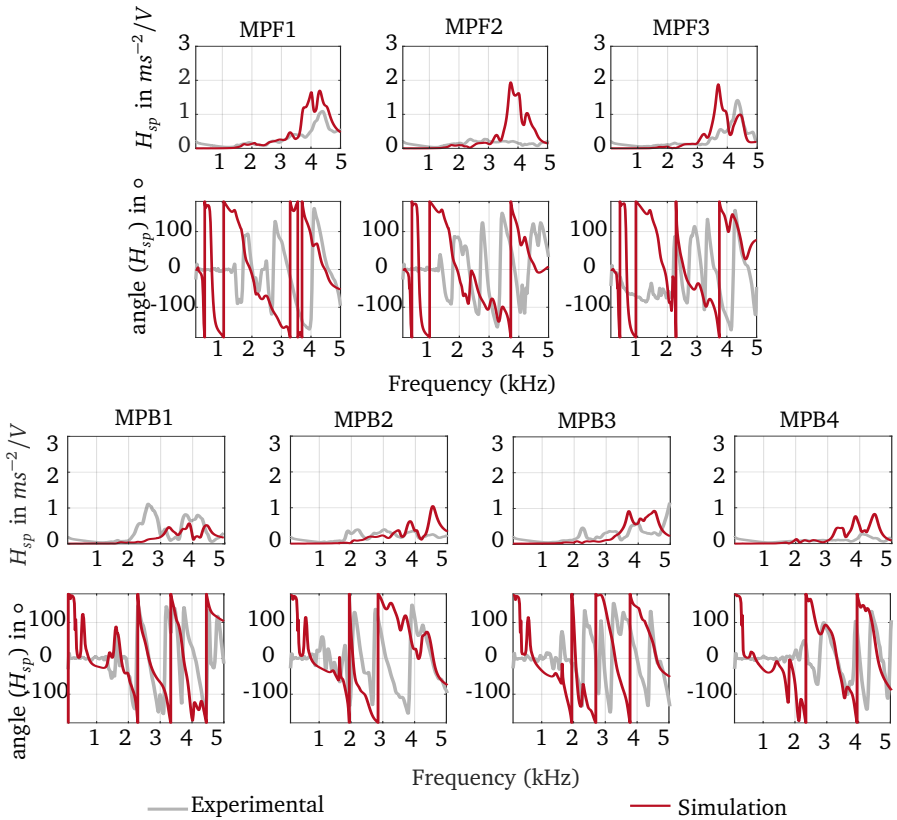


Figure 5.7: Prediction of secondary path responses from Coupled system model: here shown for Position 11

5.2 Actuator placement criteria

As already introduced in the Section 2.5.1 a variety of actuator placement criteria are applied in literature for deriving a suitable actuator location. The main disadvantage of extending the controllability Grammian for structures with complex dynamics (high number of DOFs and high modal density) that is becomes un-interpretable due to the scaling of state-matrix A . Also we need a quantitative measure to compare different actuator positions and/or layouts (in case of multiple actuators).

Since the gearbox is a complex system with spatially distributed mounting points that are required to be controlled, it is treated as a point-wise discrete system for the actuator placement problem. The complete problem of the optimal placement of actuators can be formulated by choosing from a possible set of actuator locations that satisfy spatial criteria of controllability developed by Moheimani et al. [95]. The new addition to the state of the art through the work of this thesis is that the concepts derived for continuous simple geometries like beams and plates in the literature is validated for a complex system like a gearbox for controlling high-frequency vibration. Also, the combination of these point-wise actuators is not found in literature so far. Therefore given the nature of the problem to be solved, spatial formulations fit the best.

Some terminology is introduced before proceeding to establish the placement criteria. The symbol Ω^a denotes the set of positions on the gearbox where an actuator could be possibly attached containing a number of possible positions. Let a point $P_i \in \Omega^a$ be one of those permissible actuator locations on the gearbox housing surface. As mentioned earlier, each P_i in set Ω^a is shortlisted based on the ease of integration on the gearbox housing and also spatial proximity. The total number of shortlisted actuator positions for evaluations is denoted as n_a .

The set \mathcal{B}^s contains all the points where a sensor could be attached with size s . Out of s number of sensor positions only $n_s = 7$ mounting points in the housing represented in Figure 5.6 are considered. Each of these points is represented by the symbol s_k where $k = 1, 2, \dots, n_s$. The order of numbering is: s_1, s_2 and s_3 represent the mounting points on the front i.e. MPF1, MPF2 and MPF3 respectively. Similarly, s_4 to s_7 represent the mounting points on the back i.e. MPB1 to MPB4 in the same numeric order. The secondary path frequency response functions are derived from the state space model used for sensor placement, with open loop force input at a particular actuator location and output measured at all spatially distributed sensors on the gearbox housing in the \mathcal{B}^s domain. The secondary path transfer function from each P_i to each of the mounting points s_k at each frequency point given by ω_n , where $n = 1, 2, \dots, N$ is represented by $\hat{H}(s_k, P_i, \omega_n)$. N is the total number of frequency points considered for the evaluation in the frequency band of interest.

When a combination of actuators is sought P_i is replaced by C_i , which is a vector of possible actuator positions in the combination set. For example, a 2-actuator combination C_i is represented as $[P_{i1} \ P_{i2}]$, where $i1, i2 \in [1 \ n_a]$. The total number of combina-

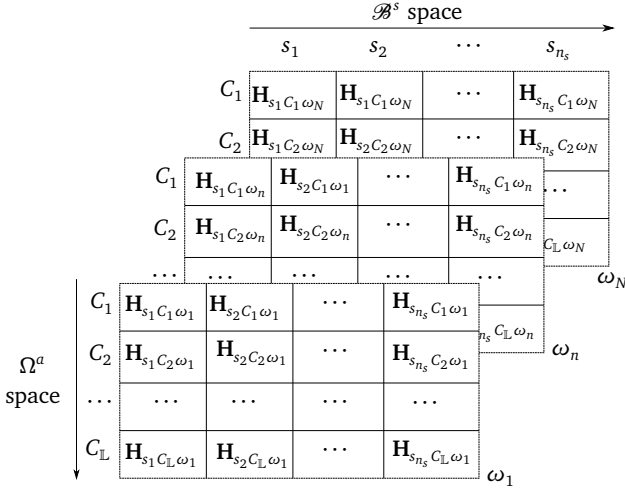


Figure 5.8: Secondary path transfer matrix for actuator combinations in set C^L

tions in this way is given by $\mathbb{L}\binom{n_a}{2}$ (choosing 2 actuators from $[1 \quad n_a]$). The actuator combination set can therefore be represented as C^L . The combined influence of control authority at a point s_k on the gearbox at a particular excited frequency ω_n is given by the combined transfer function of each actuator combination C_l as follows :

$$\mathbf{H}_{s_k C_l \omega_n} = [\hat{H}(s_k, P_{i1}, \omega_n) \quad \hat{H}(s_k, P_{i2}, \omega_n)]^T \quad (5.5)$$

where $[\cdot]^T$ denotes transpose. It should be carefully noted that \mathbf{H} represents a transfer function matrix of multi input (actuator) single-output (sensor) system, while \hat{H} represents a single input single output system, when considered for each mounting point. A schematic visualisation of this three-dimensional matrix, henceforth denoted by \mathbf{G} can be seen in Figure 5.8. The single actuator optimisation equivalent can be generated by replacing C_l with P_i and SIMO transfer function \mathbf{H} with H in each grid of the matrix.

An index has to be developed for each actuator or actuator combination to evaluate the authority of actuators over the entire mounting points set in the spatial domain, \mathcal{B}^s and also in the frequency band of interest ω . A systematic reformulation of the controllability concepts considering the spatial distribution in the system is needed to apply them to the actuator position optimisation problem. The ability of an actuator to influence multiple points on the gearbox housing is termed spatial controllability. The authority of the same actuator upon various operational modes (or frequencies) excited by the primary path is known as modal controllability. To derive an actuator position for vibration control of the

gearbox housing it is essential to consider both of these aspects simultaneously.

As introduced in Section 2.5.1, the spatial \mathcal{H}_2 norm was introduced in Equation 2.5, which can be rewritten here for both the discrete actuator points as well as the actuator combination as:

$$\begin{aligned}\|\hat{H}\|_{2,sp}^2 &= \frac{1}{2\pi} \int_{\beta^s} \int_0^\infty \text{tr}\{\hat{H}(s_k, P_i, \omega)\hat{H}^*(s_k, P_i, \omega)\} d\omega ds \\ &= \sum_{k=1}^{n_s} \|\hat{H}(s_k, P_i)\|_2^2\end{aligned}\quad (5.6)$$

$$\begin{aligned}\|\mathbf{H}\|_{2,sp}^2 &= \frac{1}{2\pi} \int_{\beta^s} \int_0^\infty \text{tr}\{\mathbf{H}(s_k, C_l, \omega)\mathbf{H}^*(s_k, C_l, \omega)\} d\omega ds \\ &= \sum_{k=1}^{n_s} \|\mathbf{H}(s_k, C_l)\|_2^2\end{aligned}\quad (5.7)$$

Using the \mathcal{H}_2 norm of the constructed secondary path matrix shown in Figure 5.8, two scores are developed to decide the actuator position. The first is a modal controllability score and the second is a spatial controllability score.

Measure of modal controllability

The first part of the index development is to calculate the actuator's ability to exert a significant amount of force at the spatial points on the housing. The notion of spatial \mathcal{H}_2 norm [95] is applied to each frequency ω_n by using the frequency response data from transfer function matrix shown in Figure 5.8. First, a term f_n is defined using the \mathcal{H}_2 norm in spatial sense at each frequency ω_n . For a single actuator the term is represented as $f_n(P_i)$ and for an actuator combination it is represented as $f_n(C_l)$.

$$f_n(P_i) = \sum_{k=1}^{n_s} \|\hat{H}(s_k, P_i, \omega_n)\|_2^2 \quad (5.8a)$$

$$f_n(C_l) = \sum_{k=1}^{n_s} \|\mathbf{H}(s_k, C_l, \omega_n)\|_2^2 \quad (5.8b)$$

Each of the above two represent the energy that an actuator or an actuator combination introduces across the spatially distributed sensor points at that particular frequency ω_n . The difference between calculating f_n for a single actuator and an actuator combination is the way the \mathcal{H}_2 norm is calculated. For a single actuator, the \mathcal{H}_2 norm is taken for the vector of size $1 \times n_s$. For a 2-actuator combination the \mathcal{H}_2 norm is calculated for the matrix of dimensions $2 \times n_s$.

Now, a modal controllability index is defined as a relative measure by dividing the value

with the maximum obtained value across all actuator positions or combinations possible for a given frequency ω_n as follows:

$$\begin{aligned}\mathcal{M}_n(P_i) &= \frac{f_n(P_i)}{\max_{P_i \in \Omega^{na}} f_n(P)} \\ \mathcal{M}_n(C_l) &= \frac{f_n(C_l)}{\max_{C_l \in C^L} f_n(C)}\end{aligned}\quad (5.9)$$

The relative modal controllability index is used to determine the authority of a selected actuator layout to cancel the primary path vibration at a particular excited frequency ω_n . If the index is very small, then the actuator layout is rendered ineffective for that particular frequency. Combining Equation 5.5 and Equation 5.8, the can be redefined as a two-dimensional modal controllability matrix. For individual actuator positions \mathcal{M}_p is given by:

$$\mathcal{M}_p = \begin{bmatrix} \mathcal{M}_1(P_1) & \mathcal{M}_2(P_1) & \cdots & \mathcal{M}_N(P_1) \\ \mathcal{M}_1(P_2) & \mathcal{M}_2(P_2) & \cdots & \mathcal{M}_N(P_2) \\ \cdots & \cdots & \cdots & \cdots \\ \mathcal{M}_1(P_i) & \mathcal{M}_2(P_i) & \cdots & \mathcal{M}_N(P_i) \\ \cdots & \cdots & \cdots & \cdots \\ \mathcal{M}_1(P_{n_a}) & \mathcal{M}_2(P_{n_a}) & \cdots & \mathcal{M}_N(P_{n_a}) \end{bmatrix} \quad (5.10)$$

For actuator combination C , the corresponding modal controllability matrix \mathcal{M}_C is shown below:

$$\mathcal{M}_C = \begin{bmatrix} \mathcal{M}_1(C_1) & \mathcal{M}_2(C_1) & \cdots & \mathcal{M}_N(C_1) \\ \mathcal{M}_1(C_2) & \mathcal{M}_2(C_2) & \cdots & \mathcal{M}_N(C_2) \\ \cdots & \cdots & \cdots & \cdots \\ \mathcal{M}_1(C_l) & \mathcal{M}_2(C_l) & \cdots & \mathcal{M}_N(C_l) \\ \cdots & \cdots & \cdots & \cdots \\ \mathcal{M}_1(C_L) & \mathcal{M}_2(C_L) & \cdots & \mathcal{M}_N(C_L) \end{bmatrix} \quad (5.11)$$

Measure of spatial controllability

Using the term in Equation 5.8, a spatial controllability measure is defined using the spatial \mathcal{H}_2 norm across the frequency band of interest. For a single actuator the spatial controllability measure is represented by \mathbf{S}_i and for an actuator combination, it is represented by \mathbf{S}_l . The quantities are defined as:

$$\mathbf{S}_i = \sqrt{\sum_{n=1}^N f_n^2(P_i)} \quad (5.12a)$$

$$\mathbf{S}_i = \sqrt{\sum_{n=1}^N f_n^2(C_l)} \quad (5.12b)$$

This results in a single performance score for each actuator and an actuator combination across the whole frequency range. The calculation performed by Equation 5.12, reduces the matrix \mathbf{G} to a column vector containing spatial controllability scores for each actuator P_i or actuator combination C_l . A relative index is formulated by normalising each score by dividing with the maximum value across all actuator combinations as follows :

$$\hat{\mathbf{S}}_i = \frac{\mathbf{S}_i}{\max_{P_i \in \Omega^{n_a}} \mathbf{S}_i} \quad (5.13a)$$

$$\hat{\mathbf{S}}_l = \frac{\mathbf{S}_l}{\max_{C_l \in C^L} \mathbf{S}_l} \quad (5.13b)$$

The entire process of the actuator layout selection is defined constrained mathematical optimization problem by maximizing the spatial controllability measure of a particular actuator layout that should have sufficient modal controllability, say β_m in the frequency band of interest. Mathematically this is depicted for a single actuator positioning problem as follows:

$$\begin{aligned} \max_{P_i \in \Omega^{n_a}} \quad & \hat{\mathbf{S}}_i(P_i) \\ \text{s.t.} \quad & \mathcal{M}_n(P_i) \geq \beta_m, \quad n = 1, 2, \dots, N \end{aligned} \quad (5.14)$$

The derived optimal single actuator position will be denoted as P_{opt} .

For deriving an actuator combination set the following optimisation criteria has to be satisfied:

$$\begin{aligned} \max_{C_l \in C^L} \quad & \hat{\mathbf{S}}_l(C_l) \\ \text{s.t.} \quad & \mathcal{M}_n(C_l) \geq \beta_m, \quad n = 1, 2, \dots, N \end{aligned} \quad (5.15)$$

The actuator combination hence obtained is denoted as C_{opt} containing n_c actuator positions. The additional constraint while deriving an appropriate actuator combination is the minimization of cross coupling of the secondary path transfer functions. So the optimization problem from Equation 5.15 can be rewritten as:

$$\begin{aligned} \max_{C_l \in C^L} \quad & \hat{\mathbf{S}}_{l,direct}(C_l) \\ \text{s.t.} \quad \min_{C_l \in C^L} \quad & \hat{\mathbf{S}}_{l,cross}(C_l) \\ \text{s.t.} \quad & \mathcal{M}_{n1,direct}(C_l) \geq \beta_m, \quad n = 1, 2, \dots, N \end{aligned} \quad (5.16)$$

where $\hat{S}_{l,direct}(C_l)$ represents the spatial controllability score obtained using the direct transfer function. In secondary path transfer function notation, this can be given as $\hat{H}(s_k, P_i, \omega_n)$ for all $k = i$. The cross coupling spatial controllability score $\hat{S}_{l,cross}(C_l)$ is obtained using $\hat{H}(s_k, P_i, \omega_n)$ for all $k \neq i$.

The value of minimum modal controllability, β_m is a designer specific objective. It denotes the percentage of frequencies in a given range the actuator position can achieve good controllability across all points. In the next sections, the actuator position and an actuator combination will be derived using the experimental transfer functions obtained by placing the IMA on these positions and compared with the actuator position obtained by using the transfer functions generated using the IMA coupled model introduced in Section 5.1. The comparison of the outcome of positioning problem using experimental data with the simulation data provides an insight into the confidence on the system level coupled model.

5.3 Single actuator positioning

The optimization problem of positioning a single actuator on the gearbox housing is done by evaluating the secondary path transfer functions at $n_a = 11$ shortlisted positions shown in Figure 5.6.

Using the single actuator modal controllability score according to Equations 5.8 and 5.9 to generate the modal controllability matrix for individual actuator positions. The modal controllability matrix is represented as a 2-D colour map in Figure 5.9. Each row in the figure corresponds to each row of the modal controllability matrix in Equation 5.10. The value of minimum modal controllability, β_m is set to 80% for this study. This means that each of the actuator combination should have sufficient influence on all mounting point for at least 80% of the frequencies in the range of 500 - 5000 Hz. Choosing a greater value of β_m allows the actuator to have greater influence on more frequency points. All frequencies are equally weighted here. This value of β_m can be more specific in design cases where the minimum modal controllability required to be achieved by the actuator position is higher in specific regions of the frequency band. In this study, for simpler design, β_m is set to 80% for the entire frequency range of interest 500 - 5000 Hz.

The modal controllability matrix is generated for $N = 25000$ frequency points in the range of interest 500 - 5000 Hz. The number mentioned on each of the horizontal rows of the colour map indicates, the number of frequency points where a modal controllability by Equation 5.9 was achieved. It can be observed that from experimental data IMA placed at Position 10 is able to achieve good modal controllability in 18735 out of 25000 frequency points. Using the simulated data, the modal controllability values are in the same trend as the values predicted from experimental data. Position 10 is the highest performing position. To check how the actuator positions rank in terms of controllability across the seven mounting points the spatial controllability index \hat{S}_i is calculated according to Equation 5.12a and are populated in Table 5.2.

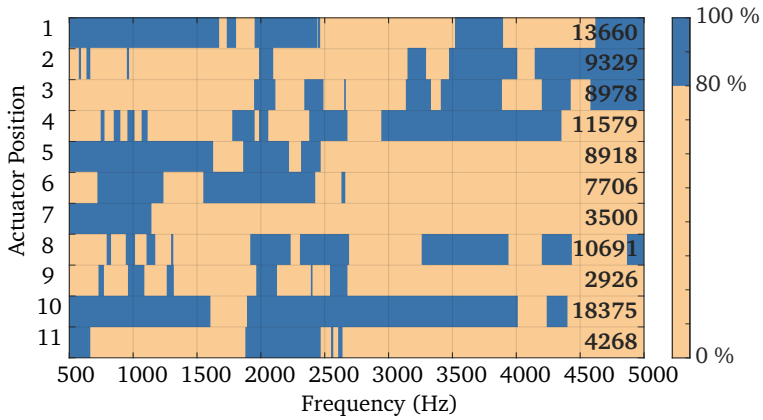


Figure 5.9: Modal controllability matrix for 11 positions using secondary path transfer functions derived from experimental data. Areas in blue represent the frequencies at which the modal controllability is $\geq 80\%$. Number of frequencies out of 25000 where the score is above 80% is also indicated in each row on the right corner

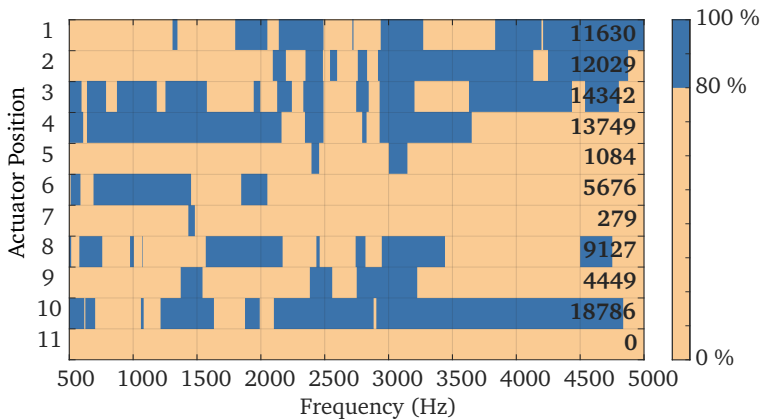


Figure 5.10: Modal controllability matrix for 11 positions using secondary path transfer functions derived from the coupled IMA model

Table 5.2: Summary of controllability indices for single actuator positioning

Actuator position	Experimental		Coupled model	
	Modal score	Spatial score	Modal score	Spatial score
1	13660	0.933	11630	0.943
2	9329	1.000	12029	0.928
3	8978	0.974	14342	0.870
4	11579	0.965	13749	0.715
5	8918	0.550	1084	0.584
6	7706	0.559	5676	0.541
7	3500	0.371	279	0.450
8	10691	0.912	9127	0.785
9	2926	0.691	4449	0.598
10	18375	0.975	18786	1.000
11	4268	0.563	0	0.607

From experimental data, the IMA placed at Position 2 has the best spatial controllability score among all seven mounting points hence obtaining a spatial score of 1. However, this position can control half as many of the frequency points compared to the second best position where IMA placed at Position 10, i.e. 9329 frequencies as opposed to 18375 frequencies from the analysed 25000 frequencies. Hence according to the experimental data, Position 10 is chosen as the best position to place the IMA for vibration control.

Position 10 has the best modal controllability score, when the position is derived using the secondary path information using the coupled IMA model. It has both the best spatial score and best modal controllability score, hence be chosen to be the best position for IMA placement. The discrepancies in the modal controllability score predicted from simulation data and IMA data arises due to the generalisation of the joint stiffness given in Table 5.1. However accurate predictions of joint stiffness at each actuator point would be a cumbersome exercise. Despite the mismatch in the modal controllability score, the trend in their values at various positions is reasonably predicted. Hence the position of the IMA on the gearbox can be identified using the generalised values as demonstrated in this analysis.

5.4 Derivation of actuator combination

The clutch case of the demonstration gearbox is rigidly attached to the engine plate of the test bench. This boundary condition also exists in the real operational condition in the car. The rigid attachment leads to some distinction in the stiffness of the two halves of the housing structure, i.e. one side of the gearbox is more rigid than the other. The difference in behaviour of the two enclosures has been reported by the authors in [101]

through impact hammer experiments. Hence, an actuator combination containing two actuators which can be placed on each side of the gearbox housing for controlling the spatial vibrations. Optimization of the number of actuators required is not performed at this stage as more actuators increase the cost of electronic hardware needed for the system. Using more actuators also introduces complicated coupling effects among the spatially distributed points on the housing leading to additional complexities of implementing the control algorithm. As a result, no further consideration has been given to this aspect.

To start with the actuator combination set, the positions shown in Figure 5.6 are divided into two groups: actuator positions on the clutch case (3 positions) and actuator positions on the transverse case (8 positions). Combination set is made by selecting one actuator from the first group positioned on clutch case and one from the second group. This gives a total of 24 possible actuator pairs.

Two types of transfer functions can be observed in the system:

- **Direct transfer functions:** These are the transfer functions corresponding to each actuator placed on one side of the housing to only the mounting points on that particular side of the housing.
- **Cross coupling transfer functions:** These represent the influence of actuator from one side of the housing to the mounting points on the other side of the housing.

Two transfer function matrices using Equation 5.5 need to be constructed. Let \mathbf{G}_1 contain only the direct transfer functions of each of the actuator positions; cross coupling transfer functions are populated as zero here. The spatial and modal controllability using this \mathbf{G}_1 matrix need to be maximised. They are denoted by $\hat{\mathbf{S}}_{l,direct}$ and $\mathcal{M}_{Cl,direct}$ respectively.

The second transfer matrix \mathbf{G}_2 is constructed using only the coupling transfer functions. The spatial and modal controllability obtained using this matrix need to be minimised in order to obtain a layout that has minimal cross coupling of actuator influences. The spatial and modal controllabilities are denoted by $\hat{\mathbf{S}}_{l,cross}$ and $\mathcal{M}_{i,cross}$ respectively.

Similar to the single actuator positioning, the limits for modal controllability β_m is 80% and the transfer functions are evaluated at $N = 25000$ frequency points in 500 - 5000 Hz.

In the decision making process the modal controllability of the direct transfer function is given first priority. The second deciding factor for choosing a combination is greater difference between the direct and cross spatial scores. If a combination has highest direct spatial score and also highest cross spatial score, this will be rejected as it indicates very high coupling among the actuators. A controller with a robust disturbance rejection feature needs to be designed to account for the cross-coupling effect. Cross coupling also introduces additional tuning complexity, in terms of increased number of parameters like the phase of the cross coupling transfer functions. If these parameters to tune have inherent errors due to incorrect modelling, the control performance and stability is highly affected. Hence, a sufficiently decoupled actuator combination is sought for, which can have high direct spatial scores with a good difference in cross score.

The resulting modal and spatial controllability scores of the actuator combinations are given in Table 5.3. Using the secondary transfer paths from experimental data, the actuator pair (P_1, P_4) i.e. one IMA positioned at Position 1 and Position 4 in Figure 5.6 is the best position. This position has the best spatial controllability score in the direct points while simultaneously having sufficient difference in cross spatial score ($1-0.826 = 12\%$).

Using the simulated secondary path information from the coupled model, it is pointed out in Table 5.3 that the actuator pairs (P_1, P_3) and (P_1, P_6) are close contenders for the best position. The actuator pair (P_1, P_3) has the best direct spatial score but the difference between the direct and cross spatial score is lower ($1-0.824 = 17.6\%$) compared to actuator pair (P_1, P_6) : $0.962 - 0.766 = 20\%$. Therefore actuator pair (P_1, P_6) is chosen if the simulated data is to be used.

It can be concluded that the actuator pairs derived using experimental and simulated transfer function data lead to the same position, i.e. Position 1 on the clutch case. The difference in the position obtained from the actuator that is to be positioned on the transverse case can be related to the generalisation of the joint stiffness for the entire rear case.

As seen from the spatial controllability scores of the direct and cross terms, there is significant amount of cross coupling. The cross spatial score differs only by 10 - 20%. This would make the control implementation with multiple actuators more complex. Typically for disturbance rejection a combination of feedforward control with a robust feedback control would be needed. Also, using two actuators would also require two power amplifiers, which can significantly increase the cost of the AVC system as the actuators and power amplifiers are the major components contributing to the cost (refer to Figure 7.13). Therefore in the subsequent chapter the control algorithm development and the experimental validation of the AVC system is done using only the single actuator position which is chosen to be Position 10 according to the results derived in Section 5.3 this chapter.

Table 5.3: Summary of controllability indices for derivation of actuator pairs

Actuator pair	Experimental				Coupled model			
	Modal score direct	Modal score cross	Spatial score direct	Spatial Score cross	Modal score direct	Modal score cross	Spatial score direct	Spatial score cross
(P_1, P_3)	19682	16603	0.946	0.819	22781	9157	1.000	0.824
(P_2, P_3)	17595	19902	0.938	0.989	19199	17952	0.906	0.941
(P_5, P_3)	18487	12487	0.929	0.725	17905	7471	0.874	0.796
(P_1, P_4)	23132	18675	1.000	0.826	23105	13421	0.981	0.820
(P_2, P_4)	19030	20437	0.954	0.988	17555	20151	0.848	0.934
(P_5, P_4)	19998	14136	0.932	0.749	15713	9996	0.807	0.781
(P_1, P_6)	16299	16136	0.857	0.780	21862	8445	0.962	0.763
(P_2, P_6)	12462	21388	0.781	0.989	13511	18488	0.818	0.919
(P_5, P_6)	11843	11968	0.738	0.631	9735	4178	0.747	0.714
(P_1, P_7)	15394	16108	0.840	0.778	16332	7376	0.962	0.766
(P_2, P_7)	8628	20158	0.736	0.986	7726	18305	0.811	0.919
(P_5, P_7)	9850	11966	0.671	0.624	3774	3408	0.743	0.719
(P_1, P_8)	19236	21064	0.907	0.872	17864	15245	0.976	0.833
(P_2, P_8)	14592	21280	0.850	0.996	10382	22607	0.830	0.932
(P_5, P_8)	15366	17782	0.836	0.818	8426	12620	0.798	0.808
(P_1, P_9)	16267	16464	0.861	0.788	16185	10481	0.966	0.785
(P_2, P_9)	9985	22229	0.772	0.991	8640	19018	0.824	0.926
(P_5, P_9)	11173	13131	0.740	0.682	4712	6476	0.756	0.743
(P_1, P_{10})	23149	20118	0.981	0.854	21595	16927	0.983	0.947
(P_2, P_{10})	19727	23684	0.938	1.000	18110	20500	0.881	1.000
(P_5, P_{10})	19981	18206	0.912	0.800	14942	16490	0.855	0.938
(P_1, P_{11})	16363	15937	0.856	0.785	15714	8675	0.963	0.808
(P_2, P_{11})	12276	21149	0.762	0.988	7287	17460	0.805	0.920
(P_5, P_{11})	12104	11967	0.707	0.654	3106	4319	0.748	0.769



6 Control algorithms for multi-point control

In this chapter a suitable control algorithm is derived for achieving multi-point control of vibration in the gearbox housing at the mounting points which will answer RQ 5. The term "multi-point" refers to the number of targeted points to be controlled. After having developed the sensing principle and the actuator location, a control principle has to be designed for implementing a closed loop control for the system. For active vibration control, the most widely used algorithm is the Filtered-x Least Mean Squares (FxLMS) algorithm.

In the context of this study on control algorithm, the nomenclature is undertaken from a system level perspective. The term "input" from here-on refers to the actuator input and "output" refers to the sensors measuring the vibration at the mounting points. In this study, the Single-Input Multi-Output FxLMS (SIMO-FxLMS) serves as the baseline for comparison of further explored control strategies in various aspects. The algorithms are compared in terms of various criteria such as stability, vibration reduction performance, computational complexity and robustness to model/plant uncertainties.

This chapter deals with the study of simplified versions of SIMO-FxLMS with the aim of achieving an acceptable level of multi-point control. The objective of multi-point control in the context of gearbox vibration is to avoid a significant increase in the transfer of gearbox vibration from each of the mounting points to the car body. Since the downstream path of vibration transfer from the mounting point to the body is outside the scope of the system, the objective is to reduce the vibration of each of the seven mounting points introduced in Figures 4.11 and 4.12 as much as possible.

From the review of state of the art hardware for control system implementation, it was determined that a microcontroller would be used to implement the control algorithms to drive the actuators. An appropriate control strategy needs to be designed which can be deployed on a microcontroller that has a relatively limited computing capacity compared to laboratory real-time systems. The simultaneous tasks of data acquisition and real-time control is preferred, hence a simple yet effective algorithm is developed.

In the subsequent sections of this chapter, the mathematical basics of the standard Single-Input Single-Output (SISO) FxLMS algorithm. Then using this basis, the SIMO-FxLMS is introduced which would serve as the baseline to compare the improvised versions of the subsequent proposed algorithms. Based on the status-quo algorithms, an improved version of the simplified multi-point control is suggested for the practicality of application in the gearbox scenario, using a projection (prediction algorithm) also known as the projected-FxLMS in this thesis. This is discussed in Section 7.2.

The important tuning parameters for each of the algorithms are studied in detail. The

algorithms are experimentally validated on the demonstration gearbox, with the actuator positioned at Position 10, determined from the previous chapter.

6.1 Mathematical basis of SISO FxLMS algorithm

In the context of this thesis, the target sensor will be called the error sensor from here on, and would refer to the sensors at the mounting locations of the gearbox housing that transfer energy due to structural vibrations to the downstream components such as the car frame and body.

To understand the mathematics of the FxLMS algorithm, the quantities of vibration and voltage are realised using complex quantities and are denoted with $(\hat{\cdot})$ ¹. This is because the secondary path transfer function is a complex quantity and a function of the frequency of gear mesh excitation ω_n . Let the vibration recorded at each of the mounting location of the gearbox using the MFC sensor be denoted by $\hat{q}_n(t)$, where n corresponds to frequency ω_n . The voltage generated by the control algorithm to drive the inertial mass actuator is denoted by $\hat{U}_{a_n}(t)$, also known as the control voltage. The secondary path, i.e. from the IMA control voltage to the error sensor, has a frequency-dependent transfer behaviour denoted by $\hat{H} = H_n e^{i\phi_n}$ at each frequency ω_n . This frequency response function is already estimated in the previous chapter, based on which the actuator location was finalized for control. The term ϕ_n is the phase lag experienced by the signal that travels from the controller to the IMA location and then to the mounting (sensing) point (via the secondary path) at particular frequency ω_n . This phase lag is a combination of mechanical and electrical delays.

During the operation of the gearbox under active vibration control, vibration at an error sensor in time domain is obtained as a result of both primary excitation caused by the gearbox, denoted by $\hat{d}_n(t)$ and secondary control excitations $\hat{H}_n * \hat{U}_{a_n}(t)$, where * denotes convolution. The resultant vibration measured at the sensor is given as follows:

$$\hat{q}_n(t) = \hat{d}_n(t) + \hat{H}_n * \hat{U}_{a_n}(t) \quad (6.1)$$

Gear-whine is harmonic in nature, hence the control voltage would also be harmonic, i.e., a combination of sine and cosine components at the gear mesh frequency ω_n . The control voltage in terms of sine and cosine components in complex form provided to its associated is power amplifier given as follows:

$$\hat{q}_n(t) = \hat{d}_n(t) + H_n e^{i\phi_n} (U_{a_n}^c + iU_{a_n}^s) e^{i(\omega_n t)} \quad (6.2)$$

The unknowns in the above equation are the control voltage components, $U_{a_n}^c$ and $U_{a_n}^s$, which will be adapted in an iterative manner. In experimental implementation of the control algorithm, only the real part of the sensor quantity is measured. Henceforth, only the real quantities resulting from Equation (6.2) will be used for further development of

¹Vectors are denoted with bold letters and complex quantities with $(\hat{\cdot})$

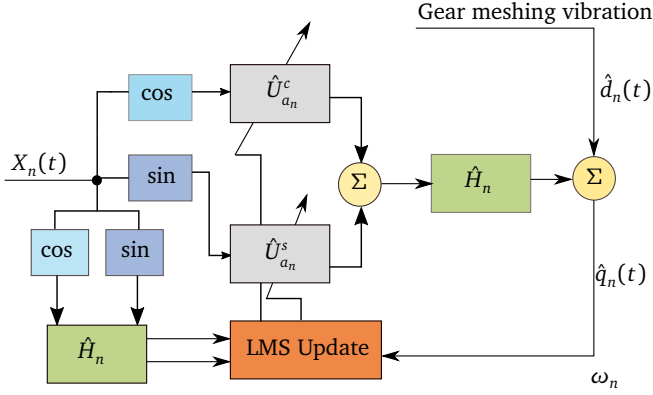


Figure 6.1: Schematic of SISO FxLMS algorithm

the algorithm. The real part of the control voltage is denoted by $U_{a_n}(t)$, can be rewritten in vector notation as follows:

$$\begin{aligned}
 U_{a_n}(t) &= U_{a_n}^c \cos(\omega_n t) + U_{a_n}^s \sin(\omega_n t) \\
 &= [\cos(\omega_n t) \quad \sin(\omega_n t)] \begin{Bmatrix} U_{a_n}^c \\ U_{a_n}^s \end{Bmatrix} \\
 &= X_n(t) \begin{Bmatrix} U_{a_n}^c \\ U_{a_n}^s \end{Bmatrix}
 \end{aligned} \tag{6.3}$$

The negative sign resulting at $U_{a_n}^s$ in the expansion of Equation 6.2 is absorbed as an unknown. In the above equation, the separation of terms of the real part of the control voltages, results in the reference signal, $X_n(t)$. This reference signal is correlated with the corresponding harmonic of the gear mesh frequency to be controlled ω_n . In the case of the gearbox, this is derived by multiplying the input rotation speed of the gearbox with the number of teeth on the pinion of the gear pair. The frequency of excitation can be derived directly from the operational gearbox via CAN signals from the test-bench and the gear teeth information for the transmission is readily available from the manufacturer. The two components of the reference signal along with the frequency-dependent lag can be generated in vector form as: $X_n(t) = [\cos(\omega_n t) \quad \sin(\omega_n t)]$.

The objective of the control algorithm at each target gear mesh frequency ω_n is to minimize the instantaneous squared quantity of the vibration signal, i.e., $\xi = (q_n(t))^2$. The steepest gradient descent algorithm [75] is employed to update the coefficients of $U_{a_n}(t)$ to minimize the vibration error signal. The gradient of the vibration signal for each

of the coefficients of $U_{a_n}(t)$ given as:

$$\begin{aligned}\nabla \xi &= \frac{d\xi}{d(U_{a_n}(t))} = 2q_n(t) \begin{Bmatrix} \frac{d(q_n(t))}{d(U_{a_n}^c)} \\ \frac{d(q_n(t))}{d(U_{a_n}^s)} \end{Bmatrix} \\ &= 2q_n(t) \begin{Bmatrix} H_n \cos(\omega_n t + \phi_n) \\ H_n \sin(\omega_n t + \phi_n) \end{Bmatrix}\end{aligned}\quad (6.4)$$

The coefficients $[U_{a_n}^c \quad U_{a_n}^s]^T$ are initialized to zero at the beginning of the adaptation. According to the algorithm, they are updated for each time step Δt as follows:

$$\begin{aligned}\begin{Bmatrix} U_{a_n}^c \\ U_{a_n}^s \end{Bmatrix}_{t+\Delta t} &= \begin{Bmatrix} U_{a_n}^c \\ U_{a_n}^s \end{Bmatrix}_t - \frac{1}{2}\mu\Delta t \nabla \xi \\ &= \begin{Bmatrix} U_{a_n}^c \\ U_{a_n}^s \end{Bmatrix}_t - \mu\Delta t q_n(t) \begin{Bmatrix} H_n \cos(\omega_n t + \phi_n) \\ H_n \sin(\omega_n t + \phi_n) \end{Bmatrix}\end{aligned}\quad (6.5)$$

The terms $[H_n \cos(\omega_n t + \phi_n) \quad H_n \sin(\omega_n t + \phi_n)]$ are similar to the nature of the reference signal including the secondary path delay. This is called the filtered-reference, hence the name FxLMS. To control multiple harmonics of the gear-mesh frequency, parallel FxLMS loops need to be implemented. The control voltage would then be a linear combination of the control voltages at each of these gear mesh harmonics.

The important parameters in a SISO-FxLMS algorithm are the step size μ and the phase angle of the secondary path ϕ_n . Several applications of the FxLMS algorithms exist where the phase delay is identified online to avoid divergence [45, 49]. The algorithm is robust if the actual secondary path phase delay during the operation is within 90° to -90° of the actual phase delay in operation [19].

The influence of step size on the convergence of the FxLMS algorithm has been extensively studied in several studies including geared transmissions [142]. Empirical formulations for choosing step size are based on the input power of the reference signal [58] also known as normalised FxLMS is also very popular. Variable step size algorithms have also been studied, where the step size is adapted according to various criteria [17]. In this study the step size is kept constant. It is further revealed how in multi-point control the step size gets implicitly customized by weighting of the sensors.

6.2 SIMO-FxLMS algorithm

When multiple target sensors need to be controlled simultaneously, the quantity of vibration measure $\hat{q}(t)$ is transformed into $\hat{\mathbf{q}}_n(t)$, which is a column vector of vibration measurements from the distributed sensors at the $n_s = 7$ mounting points. Each of the mounting points is denoted by s_k for control formulations. As introduced before, $\mathbf{H}_{s_k P; \omega_n}$ is the $n_s \times 1$ frequency response matrix of the secondary path at ω_n . For notational simplicity,

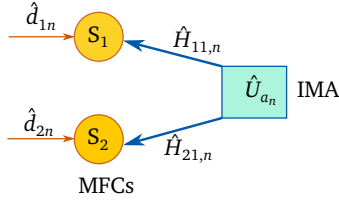


Figure 6.2: Schematic of multi-channel FxLMS algorithm

the frequency ω_n is simply denoted as n . P_i is the control actuator. Since there is only one actuator present, $P_i = 1$.

The schematic of the SIMO system is depicted in Figure 6.2. For the sake of simplicity, the mathematics of the system is derived using only two of the seven sensors as shown in the figure S_1 and S_2 . During implementation on the demonstration gearbox, it can be easily extended to all the seven mounting point sensors. Since only a single actuator system is explored which is positioned at Position 10 as derived from previous chapter, the secondary path notations are all referenced with the number 1. Hence, the secondary path transfer function between S_1 and actuator is termed as $H_{11,n}$.

The total vibration at each of the sensor can be written using Equation 6.1, where d_{1n} and d_{2n} are the primary path disturbances from the gear whine through the transfer path of shafts and bearings to the housing surface.

$$\begin{aligned}\hat{q}_{1n}(t) &= \hat{d}_{1n} + \hat{H}_{11,n} * \hat{U}_{a_n}(t) \\ \hat{q}_{2n}(t) &= \hat{d}_{2n} + \hat{H}_{21,n} * \hat{U}_{a_n}(t)\end{aligned}\quad (6.6)$$

The objective function for the SIMO-FxLMS algorithm is to minimize the following:

$$\xi_{simo} = \hat{\mathbf{q}}_n(t)^T W_s \hat{\mathbf{q}}_n(t) \quad (6.7)$$

where W_s is a $n_s \times n_s$ is a diagonal weighting matrix for each error sensor, where n_s is the total number of sensors. For a 2-sensor example shown in Figure 6.2, the error function transforms to:

$$\xi_{simo} = w_1(\hat{q}_{1n}(t))^2 + w_2(\hat{q}_{2n}(t))^2 \quad (6.8)$$

where w_1 and w_2 are the weights assigned to the error sensors S_1 and S_2 respectively. Using similar formulation for the real parts of the signal as the SISO algorithm formulation and the real part notation of the control voltage directly from Equation 6.3 along with the same reference signal $\mathbf{X}_n(t)$, the gradient of the SIMO-FxLMS algorithm is computed

as follows:

$$\begin{aligned}\nabla \xi_{simo} &= \frac{d\xi_{simo}}{d(U_{a_n}(t))} = 2\mathbf{q}_n(t) \left\{ \begin{array}{c} \frac{d(\mathbf{q}_n(t))}{d(U_{a_n}^c)} \\ \frac{d(\mathbf{q}_n(t))}{d(U_{a_n}^s)} \end{array} \right\}^T \\ &= 2\mathbf{q}_n^T(t) W_s \begin{bmatrix} H_{11,n} \cos(\omega_n t + \phi_{1n}) & H_{11,n} \sin(\omega_n t + \phi_{1n}) \\ H_{21,n} \cos(\omega_n t + \phi_{2n}) & H_{21,n} \sin(\omega_n t + \phi_{2n}) \end{bmatrix}\end{aligned}\quad (6.9)$$

The cosine and sine coefficients of the control voltage are updated for each time step Δt as follows:

$$\begin{aligned}\begin{Bmatrix} U_{a_n}^c \\ U_{a_n}^s \end{Bmatrix}_{t+\Delta t} &= \begin{Bmatrix} U_{a_n}^c \\ U_{a_n}^s \end{Bmatrix}_t - \frac{1}{2}\mu\Delta t \nabla \xi_{simo} \\ &= \begin{Bmatrix} U_{a_n}^c \\ U_{a_n}^s \end{Bmatrix}_t - \mu\Delta t \left\{ \begin{array}{l} w_1 q_{1n}(t) H_{11,n} \cos(\omega_n t + \phi_{1n}) + w_2 q_{2n}(t) H_{21,n} \cos(\omega_n t + \phi_{2n}) \\ w_1 q_{1n}(t) H_{11,n} \sin(\omega_n t + \phi_{1n}) + w_2 q_{2n}(t) H_{21,n} \sin(\omega_n t + \phi_{2n}) \end{array} \right\}\end{aligned}\quad (6.10)$$

After each update, the control voltage is updated using Equation 6.3. The coefficients are considered as converged, when no significant further increase occurs due to the $\xi_{simo} \rightarrow 0$. It may also happen that the maximum voltage limit of the power amplifier is reached, which limits the maximum amount of vibration reduction that can be achieved by the IMA.

Weighting of error signals

The weighting of the sensors is performed in various ways in literature. Of particular interest is how the step size affects the convergence capability of individual secondary paths $H_{k1,n}$. Out of the various weighting techniques, the weighting using the relative ratios of secondary path transfer functions [48] is implemented in this study. The main idea is to have smaller step size for secondary paths with smaller magnitudes. Hence, the weights implicitly tune the step size in the individual terms of the gradient update.

The weights for each error sensor s_k is given by:

$$w_k = \frac{H_{k1,n}}{\sum_{k=1}^{n_s} H_{k1,n}^2} \quad (6.11)$$

The weights at each frequency need to be tuned using the frequency dependent transfer function. The frequency dependency of the weights is not denoted as a subscript here. The complexity is quantified in terms of number of multiplications performed during the implementation of the control loop at each incremental time-step Δt . The total number of multiplications and additions will grow with consideration of all seven points in the $\mathbf{q}(t)$ vector sevenfold in each step; i.e. calculation of the gradient, update of the coefficients and the control voltage calculation. The complexity is summarised in Table 7.1 later in this chapter after implementing it on the gearbox. The need for reducing the controller

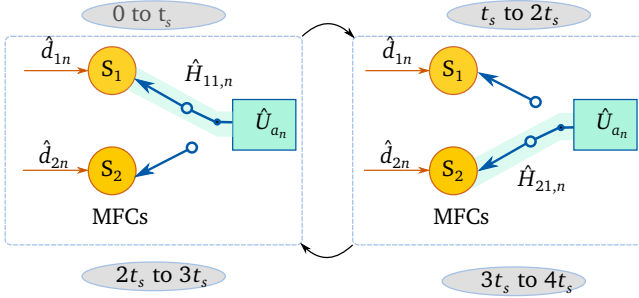


Figure 6.3: Schematic of Switched-Error FxLMS algorithm

complexity results from constraints on the computational resources in real time for high frequency vibrations. Therefore the important scientific question has to be raised here is whether the multi-point control strategy be simplified with similar performance (vibration reduction capabilities) and robustness as SIMO-FxLMS? Through simplification can some benefits be defined for a complex system such as a gearbox?

In the next sections, three simplifications of the SIMO-FxLMS are proposed. The main idea is to achieve global reduction but with converting effectively the SIMO-FxLMS into a SISO-FxLMS. In Section 6.3 a switching scheme algorithm is introduced followed by a mixed-error approach in Section 6.4. Each of the important parameters and assumptions are analysed in detail.

6.3 Switched-error FxLMS algorithm

The idea of a switched-error FxLMS is to effectively have only one error sensor (out of the multiple sensors), to adapt the control voltage to the actuator at any given instant of time. This significantly reduces the computational complexity when compared to the SIMO-FxLMS. From the time when control is activated, each error sensor will be used sequentially to adapt the force for a certain time period called the switching period, denoted by t_s . After all the sensors in the set are used once, the error sensor is again reset back to the first sensor in the set. This is called round-robin sequence of switching.

The objective function for the switched-error FxLMS can be defined as $\xi_{sw} = (\hat{q}_{sw}(t))^2$. The \hat{q}_{sw} is the instantaneous error sensor that is actively used to adapt the control voltage in time. In Figure 6.3, the algorithm is demonstrated with two sensors.

$$\xi_{sw} = \begin{cases} (\hat{q}_{1n}(t))^2, & \text{time } 0 \text{ to } t_s \\ (\hat{q}_{2n}(t))^2, & \text{time } t_s \text{ to } 2t_s \end{cases} \quad (6.12)$$

The adaptation of the control voltage is time dependent with each update essentially a SISO-FxLMS, and the gradient incorporates the active error sensor at that particular time instant. Using the real parts of the signals, gradient of the objective functions is defined as follows

$$\begin{aligned} \nabla \xi_{sw} &= \frac{d\xi_{sw}}{d(U_{a_n}(t))} = 2q_{sw}(t) \begin{Bmatrix} \frac{d(q_{sw}(t))}{d(U_{a_n}^c)} \\ \frac{d(q_{sw}(t))}{d(U_{a_n}^s)} \end{Bmatrix} \\ &= 2q_{sw}(t) \begin{Bmatrix} H_n \cos(\omega_n t + \phi_n) \\ H_n \sin(\omega_n t + \phi_n) \end{Bmatrix} \\ &= \begin{cases} 2q_{1n}(t) \begin{Bmatrix} H_{11,n} \cos(\omega_n t + \phi_{1n}) \\ H_{11,n} \sin(\omega_n t + \phi_{1n}) \end{Bmatrix}, & \text{time } 0 \text{ to } t_s \\ 2q_{2n}(t) \begin{Bmatrix} H_{21,n} \cos(\omega t + \phi_{2n}) \\ H_{21,n} \sin(\omega t + \phi_{2n}) \end{Bmatrix}, & \text{time } t_s \text{ to } 2t_s \end{cases} \end{aligned} \quad (6.13)$$

Using the gradient above, adaptation each of the coefficients of the control voltage can be calculated iteratively using the following:

$$\begin{aligned} \begin{Bmatrix} U_{a_n}^c \\ U_{a_n}^s \end{Bmatrix}_{t+\Delta t} &= \begin{Bmatrix} U_{a_n}^c \\ U_{a_n}^s \end{Bmatrix}_t - \frac{1}{2} \mu \Delta t \nabla \xi_{sw} \\ &= \begin{cases} \begin{Bmatrix} U_{a_n}^c \\ U_{a_n}^s \end{Bmatrix}_t - \mu \Delta t \begin{Bmatrix} q_{1n}(t) H_{11,n} \cos(\omega_n t + \phi_{1n}) \\ q_{1n}(t) H_{11,n} \sin(\omega_n t + \phi_{1n}) \end{Bmatrix}, & \text{time } 0 \text{ to } t_s \\ \begin{Bmatrix} U_{a_n}^c \\ U_{a_n}^s \end{Bmatrix}_t - \mu \Delta t \begin{Bmatrix} q_{2n}(t) H_{21,n} \cos(\omega_n t + \phi_{2n}) \\ q_{2n}(t) H_{21,n} \sin(\omega_n t + \phi_{2n}) \end{Bmatrix}, & \text{time } t_s \text{ to } 2t_s \end{cases} \end{aligned} \quad (6.14)$$

The control voltage is tuned as a summation of voltages tuned for each sensor. When the error sensor is switched, only coefficients of the voltage corresponding to the selected error are tuned. The last tuned values for the sensor before the switching event keeps the vibration at the previous sensor from growing in case the phase angle of the next sensor differs by more than $\pm 90^\circ$.

Selection of switching time

The concept of error switching for noise control has been demonstrated by Marek et al. [92] for active casings but detailed discussion about the effect of parameters such as the switching period on the effectiveness of the algorithm is absent in literature. The only statement stated in previous literature so far is that the switching time has to be "fast enough". It has been claimed in previous works by the same authors [91] that the

convergence speed of the switched-error FxLMS algorithm is slower compared to the MIMO-FxLMS. Despite the loss in convergence speed, the reduced complexity makes it the switched error algorithm a viable choice to implement for multi-point control with the selection of an appropriate switching time.

There could be two logical ways of selecting the switching time from the formulation of the algorithm:

1. Upper limit is based on the time taken to achieve convergence of weights, i.e. coefficients $U_{a_n}^c$ and $U_{a_n}^s$ of the control.
2. Lower limit is decided by the frequency of the signal to be controlled. It was empirically introduced in the previous work [91], i.e the switch shouldn't happen in each sample. This indicates that the switching is related to the sampling frequency. For example, if F_s is the sampling frequency of the controller, then the sample time $T_s = \frac{1}{F_s}$. In order to ensure that the switching does not occur in each sample, the switching time should at least be $2 \times T_s$.

For each of the above, the experimental study is performed for the control of vibrations on the gearbox. The switching time is studied on two different levels, 0.1 s and 0.001 s.

6.4 Mixed-error FxLMS algorithm

Another simplification that can be made to the SIMO-FxLMS algorithm is to combine the sensor information from multiple mounting points into a single quantity. This reduces the number of inputs required to adapt the actuator voltage using the control algorithm given in Equation 6.10. Combining sensors allows each control force to be optimized when the number of error sensors is greater than the number of control sources [128]. The combination of sensors into one mixed sensors can be termed as agglomeration. The sensor set is divided into two subsets - MPFs and MPBs as already introduced in Chapter 5. Sensors from each side of the gearbox will be "mixed" to form a virtual sensor. The main assumption based on which the "mixing" can be performed is the physical proximity of the sensors. The mixing of sensor information is done by simple addition of the absolute magnitudes of the sensor quantities, multiplied by a weight as shown in Figure 6.4. The actual number of physical sensors present in the system remains unchanged as they need to be present to calculate the real-time mixed error for adapting the control voltage for the actuator.

The objective of the mixed-error algorithm is defined as $\xi_{mix} = (\hat{q}_{mix,n}(t))^2$, where $\hat{q}_{mix,n}(t)$ is given by

$$\hat{q}_{mix}(t) = w_1 | \hat{q}_{1n}(t) | + w_2 | \hat{q}_{2n}(t) | \quad (6.15)$$

The mixed-error is treated as a new virtual sensor point with its own secondary path transfer function $\hat{H}_{mix,n} = H_{mix,n} e^{j\phi_{mix,n}}$. The physical effect of the actuator force at each

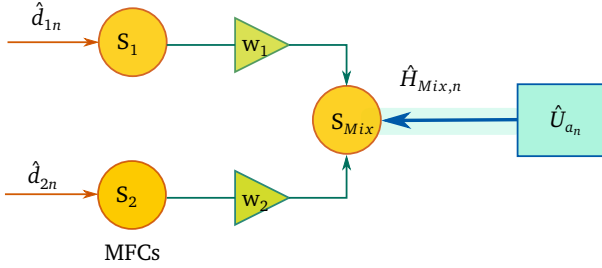


Figure 6.4: Schematic of Mixed-error FxLMS algorithm

individual sensors remains exactly as given in Equation 6.6. In addition, the mixed vibration can be written as:

$$\hat{q}_{mix}(t) = w_1 |\hat{d}_{1n}(t) + \hat{H}_{11,n} * \hat{U}_{a_n}(t)| + w_2 |\hat{d}_{2n}(t) + \hat{H}_{21,n} * \hat{U}_{a_n}(t)| \quad (6.16)$$

It is evident from above that $\hat{H}_{mix,n}$ is just a weighted sum of $\hat{H}_{11,n}$ and $\hat{H}_{21,n}$. The idea behind the assumption of mixing using physical proximity of the sensors, the secondary path phase delay from the actuator to each of the sensors in the subset does not differ. Therefore, once combined, the mixed phase ϕ_{mix} is not very different from the originally identified phase delays of the individual sensors ϕ_{1n} and ϕ_{2n} . The convergence criteria of the mixed error algorithm can be derived from the robustness of SISO-FxLMS with respect to the phase delay, $\phi_{mix,n}$ being in the range of $\pm 90^\circ$ of each of the individual secondary path phases in the mixture.

The adaptation of the sine and cosine components of the IMA control voltage is again a SISO-FxLMS with a slightly modified computation of the gradient. The gradient of the objective of mixed-error using the real parts of the signals can be written as:

$$\begin{aligned} \nabla \xi_{mix} &= \frac{d\xi_{mix}}{d(U_{a_n}(t))} \\ &= 2q_{mix}(t) \left\{ \begin{array}{l} \frac{d(q_{mix,n}(t))}{d(U_{a_n}^c(t))} \\ \frac{d(q_{mix,n}(t))}{d(U_{a_n}^s(t))} \end{array} \right\} \\ &= 2q_{mix,n}(t) \left\{ \begin{array}{l} w_1 \frac{d(q_{1n}(t))}{d(U_{a_n}^c(t))} + w_2 \frac{d(q_{2n}(t))}{d(U_{a_n}^c(t))} \\ w_1 \frac{d(q_{1n}(t))}{d(U_{a_n}^s(t))} + w_2 \frac{d(q_{2n}(t))}{d(U_{a_n}^s(t))} \end{array} \right\} \\ &= 2(w_1 |q_{1n}(t)| + w_2 |q_{2n}(t)|) \left\{ \begin{array}{l} w_1 H_{11,n} \cos(\omega_n t + \phi_{1n}) + w_2 H_{21,n} \cos(\omega_n t + \phi_{2n}) \\ w_1 H_{11,n} \sin(\omega_n t + \phi_{1n}) + w_2 H_{21,n} \sin(\omega_n t + \phi_{2n}) \end{array} \right\} \quad (6.17) \end{aligned}$$

Using the gradient above, the adaptation each of the components of the control voltage

can be calculated iteratively using the equations:

$$\begin{aligned} \begin{Bmatrix} U_{a_n}^c \\ U_{a_n}^s \end{Bmatrix}_{t+\Delta t} &= \begin{Bmatrix} U_{a_n}^c \\ U_{a_n}^s \end{Bmatrix}_t - \frac{1}{2}\mu\Delta t \nabla \xi_{mix} \\ &= \begin{Bmatrix} U_{a_n}^c \\ U_{a_n}^s \end{Bmatrix}_t - \mu\Delta t \sum_{k=1}^2 w_k q_{kn}(t) \left\{ \begin{array}{l} \sum_{k=1}^2 w_k H_{k1,n} \cos(\omega_n t + \phi_{kn}) \\ \sum_{k=1}^2 w_k H_{k1,n} \sin(\omega_n t + \phi_{kn}) \end{array} \right\} \end{aligned} \quad (6.18)$$

It should be noted that during implementation in hardware, the $q_{mix,n} = \sum_{k=1}^2 w_k H_{k1,n}$ is calculated externally before hand and feed into the control loop, along with the pre-determined $H_{mix,n}$. This leads to an equivalent SISO-operation in the control loop and gradient calculation hence reducing the computational complexity.

The main difference between the calculation of weights in the SIMO-FxLMS and the mixed-error approach is the multiplication of the individual secondary path transfer functions in the gradient. Let $n_{mix} < n_s$ indicate the number of sensors mixed. The gradient for the mixed-error is compared with the SIMO algorithm using the same n_{mix} sensors to understand the difference in the gradient computation. Only the cos term gradient is shown as follows:

$$\begin{aligned} \nabla \xi_{simo,c} &= \sum_{k=1}^{n_{mix}} w_k q_{kn}(t) H_{k1,n} \cos(\omega_n t + \phi_{kn}) \\ \nabla \xi_{mix,c} &= \sum_{k=1}^{n_{mix}} w_k q_{kn}(t) \sum_{k=1}^{n_{mix}} H_{k1,n} \cos(\omega_n t + \phi_{kn}) \end{aligned} \quad (6.19)$$

It is to be noted that there are the additional terms of multiplication in the gradient of the mixed-error essentially leading to a difference between the two algorithms. If the output of each of the mixed sensor is identical and the secondary path transfer functions of each of them is identical to each other then the gradient $\nabla \xi_{mix,c}$ would be proportional to $\nabla \xi_{simo,c}$. Due to the small wavelengths of vibration at frequencies in the order of kHz, the vibration would differ even with a 1 mm change in distance making this proportionality of gradients highly unlikely.

6.4.1 Selection of weights in mixed-error FxLMS

From Equation 6.15, the mixed-error is a weighted sum of the errors. Similar to the SIMO-FxLMS, the weighting of the individual errors is dependant on the secondary path transfer functions of each of the individual error sensors, given by Equation 6.11.

Apart from the magnitude of the individual weights, the sign of weights is also very important in the mixed-error approach. For example, in case of a group of sensors that are physically proximate, the assumption of phase delay similarity may not be valid with high frequency vibrations. Continuing the example of the two-sensor mixing, if the phase

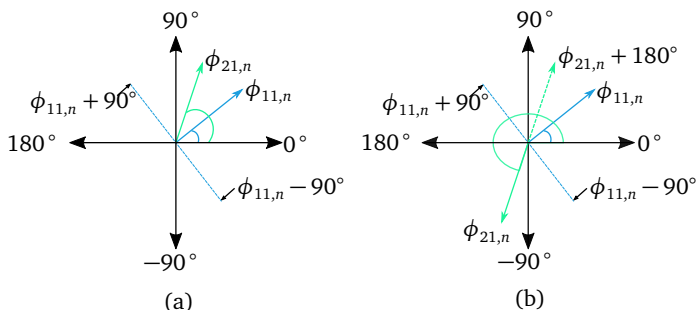


Figure 6.5: Weighting of mixed-errors. Left (a): Phases of secondary path FRFs within 90° range - all positive weights in mixing; Right (b): Phases of secondary path FRFs outside $\pm 90^\circ$ range - negative weight assigned to second sensor to flip the phase by 180°

angle of the sensor S_2 falls within the range of $\pm 90^\circ$ of the sensor S_1 , this would still lead to convergence based on the behaviour of the FxLMS algorithm. In this case the $\phi_{mix,n}$ would lie in between the two angles $\phi_{11,n}$ and $\phi_{21,n}$ and the mixing can be done using only positive weights, shown in Figure 6.5 (a).

In the case, where the secondary path response of the second sensor falls outside the $\phi_1 \pm 90^\circ$ range then the weight of the sensor can be multiplied by -1. As shown in Figure 6.5 (b), the multiplication with -1 flips the phase by 180° of the original phase, aligning it in the direction of the sensors of the group. This aids the convergence of the mixed-error algorithm.

All the three algorithms discussed here are validated together with the developed AVC on the 7HDT300 transmission. The performance and complexity of implementation are all discussed in the following chapter.

7 Experimental validation

The validation of each algorithm was conducted on the demonstration gearbox. During the experimental investigations, an unexpected short circuit event rendered one of the load machines non-operational. Therefore, to ensure accurate and reliable results, the non-functioning load machine was promptly isolated from the test bench to prevent any interference with the ongoing tests.

This meant there were two possibilities for the operational tests:

1. The non-operational load side would be electrically disconnected but mechanically still present. The unloaded side would be freely rotating. But due to the limitation of the test-bench system, no input torque can be applied in any operational case. The only torque generated would be due to drag torque caused by gear friction and oil churning.
2. The non-operational load side is disconnected mechanically from the test-bench and replaced by a frame essentially locking one side of the differential. In this condition, input torque can be applied to the gearbox. This mode of operation although non-idealistic, generates significant observable gear mesh harmonics that can be controlled. This is shown in Figure 7.1.

For the experimental performance evaluation of the control algorithms, the locked condition is used. The transmission was engaged in 3rd gear and run in steady state at 500 RPM. Higher speeds are not recommended for the locked condition. Figure 7.1 shows the vibration recorded at mounting points both on the clutch and transverse case by MPF2 and MPB2 sensors respectively. The gear mesh frequencies observed clearly are 1958 Hz, 2500 Hz, 2936 Hz and 4056 Hz. Of all the peaks, the 2500 Hz has the highest magnitude and also corresponds to a prominent resonance point observed from the speed ramp experiments from Chapter 3, Figure 3.19. Therefore all the algorithms will be tuned to control the 2500 Hz gear mesh frequency.

Performance of SIMO-FxLMS

The SIMO-FxLMS was applied to the 2500 Hz gear mesh frequency both with equal weights and with weights given by Equation 6.11 to tune the IMA control voltage. The results are presented in Figure 7.2 for all the mounting points on the clutch case and in Figure 7.3 for all the mounting points on the transverse case. The left column in each figure represents the equal weights assigned to each of the mounting points when the objective is calculated according to Equation 6.8. The results on the left column of Figures

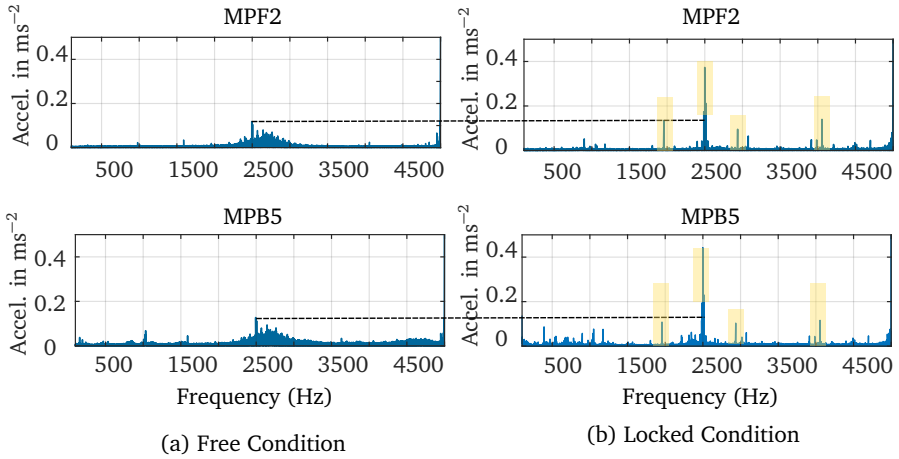


Figure 7.1: Vibrations recorded for free (a) and locked (b) test bench condition at IMS Connect

7.2 and 7.3 show that assigning equal weights, caused the vibration in all points except MPF2 to increase, hence proving that equal weights is a very bad choice for multi-point control. The weights calculated using the secondary path transfer function using Equation 6.11 showed that the appropriate control voltage magnitudes to improve the reduction of vibration at the mounting points is possible.

It is to be noted that the SIMO-FxLMS would not always cause a reduction among all points. Since it is the weighted sum of squares objective, it is not necessary that the individual quantities will be reduced but the global sum would be reduced. Hence, similar result as for 2500 Hz may not be expected for other frequencies.

Performance of Switched-Error FxLMS

Using the SISO-FxLMS algorithm on each of the errors, the order of time of convergence for adapting the weight is about 0.1 s - 0.5 s. Hence, the upper limit of switching time is $t_s = 0.1$ s. The lower limit was set based on the sampling frequency in the experiment (20 kHz), and therefore to allow sufficient switching time $t_s = 0.001$ s is chosen which switches after 20 samples.

During the implementation of the switching-error, the control voltage is given as a sum of 7 voltages. Each voltage corresponding to each of the seven sensors. When the algorithm is "switched" to a particular error sensor, the voltage coefficients are adapted only for that sensor. After the time t_s when the error switches, the adapted coefficients

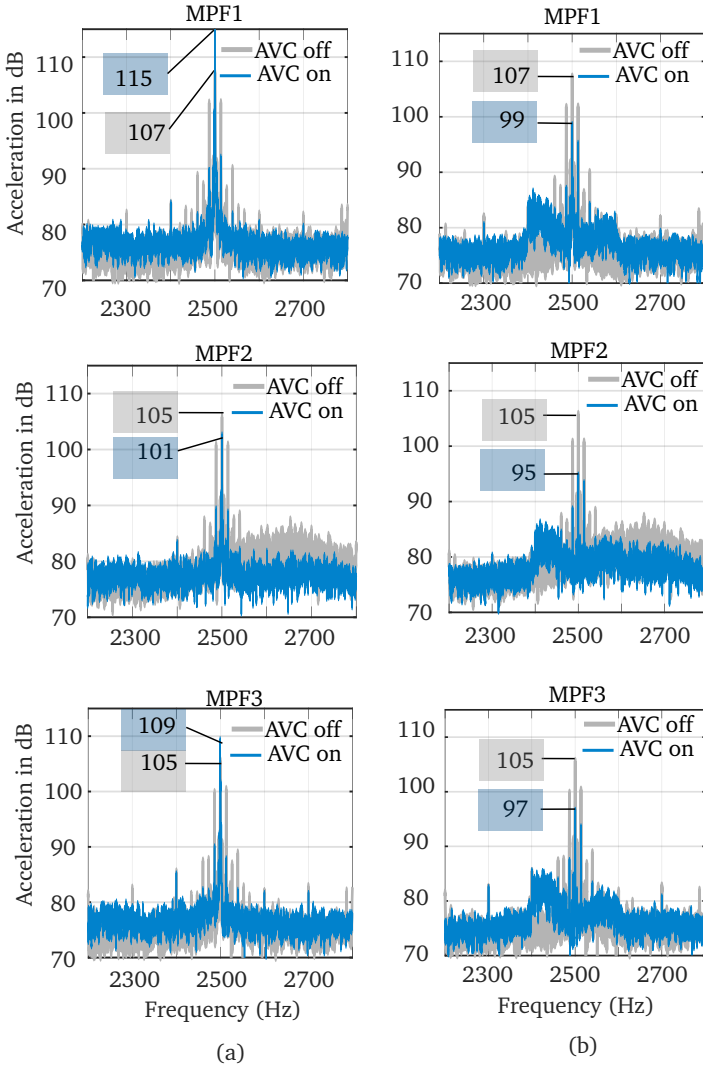


Figure 7.2: Performance of SIMO-FxLMS algorithm at MPF1-3. Left (a): all sensors weighted equally. Right (b): Sensors weighted according to Equation 6.11

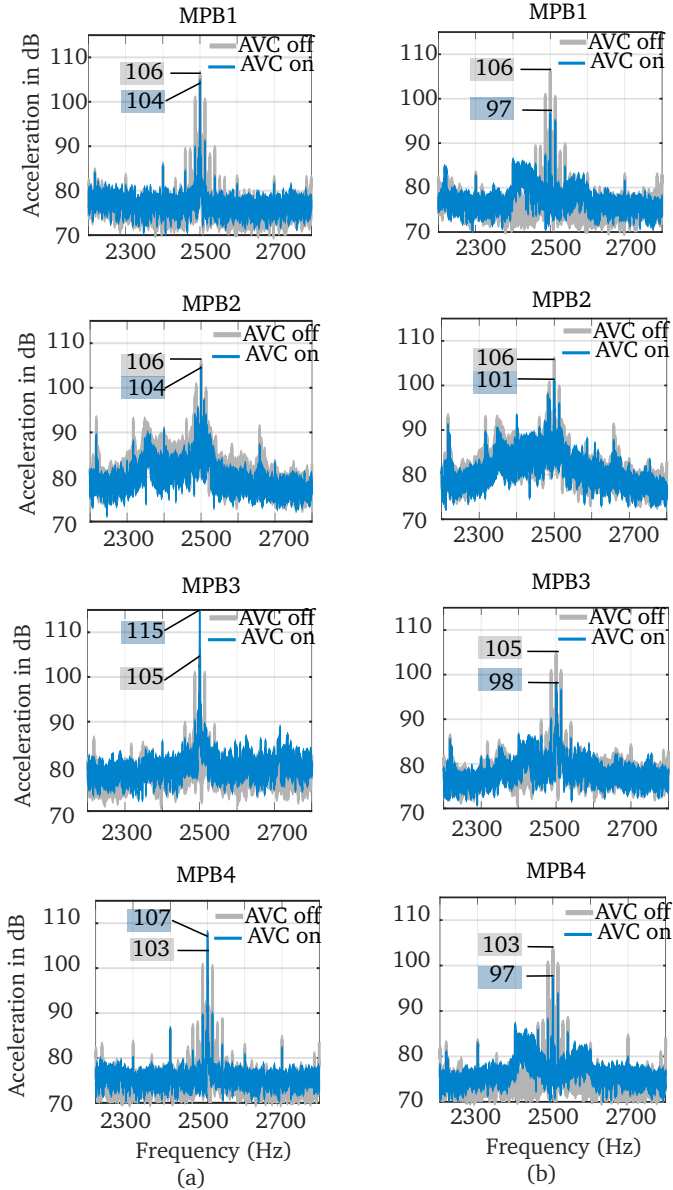


Figure 7.3: Performance of SIMO-FxLMS algorithm at MPB1-4. Left (a): all sensors weighted equally. Right (b): Sensors weighted according to Equation 6.11

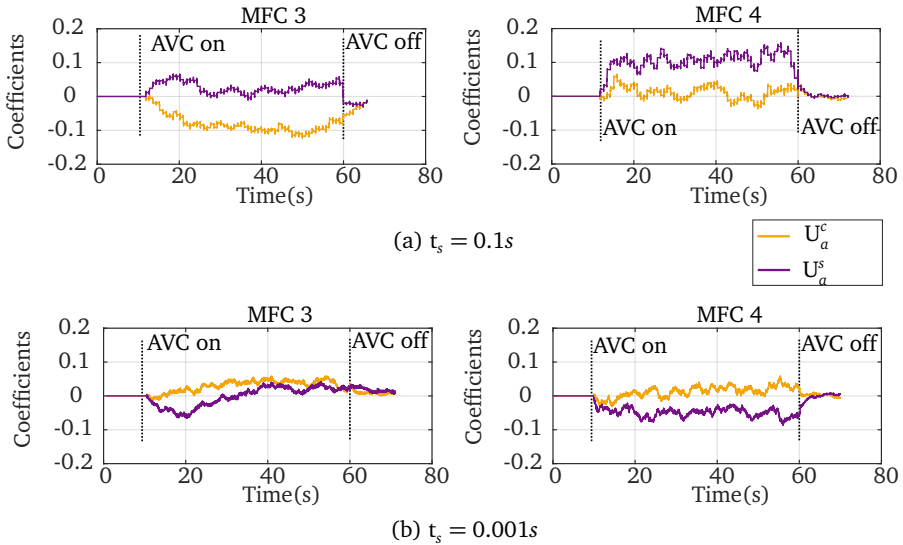


Figure 7.4: Convergence of coefficients with switching time: Top (a) $t_s = 0.1$ s coefficients converge within 1s of start of AVC. Bottom (b) $t_s = 0.001$ s coefficients converge within 10-20 s of start of AVC.

for the previous sensor are held constant until that sensor is active again. This is done to make sure when the adaptation of coefficients take place on a sensor, whose secondary path phase is outside the range of $\pm 90^\circ$ of the other sensors, instability is avoided. Hence, it can be seen that the coefficients in Figure 7.4 are held for a certain period of time. For the coefficient when $t_s = 0.001$ s, the holding period is not very apparent due to the short switching time.

Similar to the SIMO-FxLMS results, the Switched-error FxLMS are also organised in two separate plots: Figures 7.5 and 7.6. In each figure, the left column corresponds to the switching time $t_s = 0.1$ s and the right column corresponds to the switching time $t_s = 0.001$ s.

The main disadvantage of slower switching time, $t_s = 0.1$ s is during the time the force adapts using one error sensor as the objective, there could be an increase in vibration in another sensor in the error set. Therefore it was observed that vibration at only two of the seven sensors, MPF1 and MPF3 were reduced by 5 dB and 4 dB respectively. One way of dealing with overcoming this problem is to alter the sequence of error sensors in the round-robin sequential technique gradually increasing phase angles. But this would have to be customised for each frequency point and would eventually be a cumbersome tuning

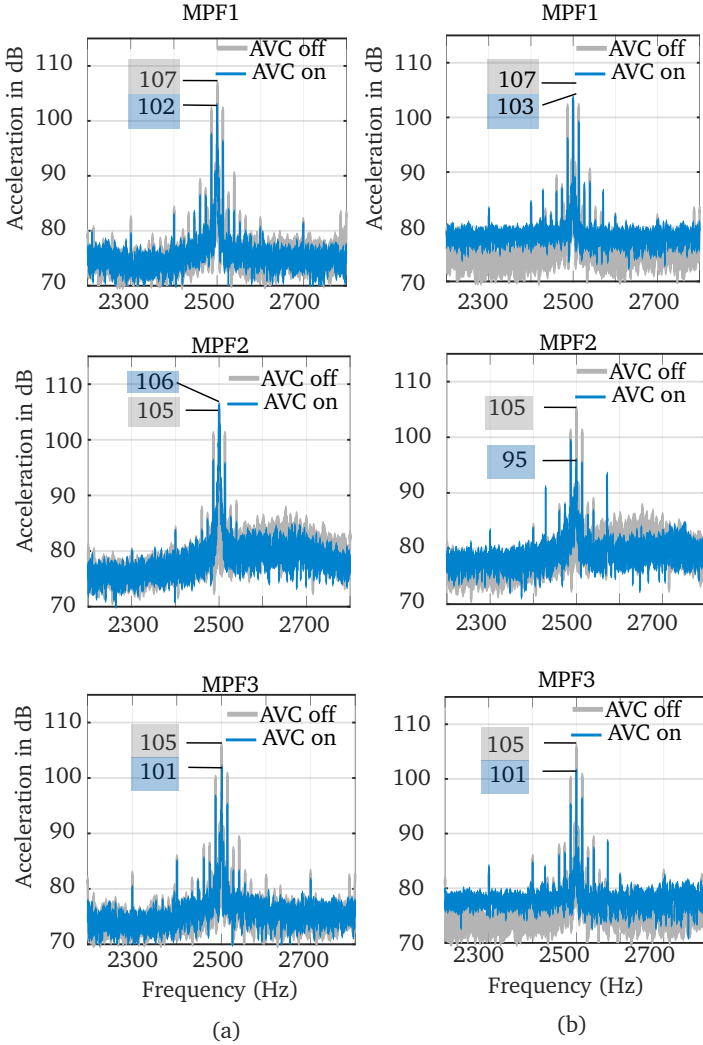


Figure 7.5: Switched error FxLMS validation on mounting points on clutch case
 MPFs: Left side (a): $t_s = 0.1s$; Right (b): $t_s = 0.001s$

process. Lower switching time although guarantees a faster convergence of individual weights as seen in Figure 7.4 (a). However, this may lead to global instability when the phase delay of the error sensors are not oriented in a favourable manner i.e within $\pm 90^\circ$ of one another.

The advantage of a faster switching time, $t_s = 0.001$ s is that the control signal quickly adapts instantaneously to each of the error signals, leaving less time for the vibration at unfavourably placed error sensor (in terms of secondary path phase delays) to increase. With faster switching time, vibration at all mounting points except MPB2 were controlled - refer right hand column of Figure 7.6. For the front points the faster switching time also lead to greater reduction in MPF2 (10 dB compared to the slower switching time response) However, the increase in vibration at MPB2 is relatively low compared to the case of the slower switching time. Hence, the faster switching time i.e. $t_s = 0.001$ s is preferred for high frequency control applications.

Performance of mixed-error-FxLMS

From the derivation in Section 6.4, there are two cases of mixing validated on the gearbox: using only the mounting point sensors on the clutch case - MPFs and using only the mounting points on the transverse case. It is to be noted that the mixed-error experiments for MPFs and MPBs were conducted independently and no simultaneous mixing was done. Which means that when the front mounting points are mixed, the transverse case mounting points are not taken into consideration, hence the vibration there is not tracked. Same condition was also valid for when the mixed-error experiment was performed with the transverse case mounting points. This was done because of the assumption on which the mixed-error algorithm is based, spatial proximity. Having two clusters of mixed points will lead to SIMO-control which is again a different class of multi-point control which is not dealt here.

When the front points are mixed with equal weights, the vibration is reduced in all three sensors as seen in Figure 7.8. Both with equal weighting and using the weights given by Equation 6.11, a reduction across all the mounting points is possible. This is because the phase of the secondary paths of these mounting points are within the $\pm 90^\circ$ range of one another as shown in Figure 7.7 (a). The individual weighting using the secondary path information helped in achieving greater reduction in the mounting point MPF2 from 7 dB to 12 dB.

In the experiment with the mixing of the mounting points on the transverse case, the vibration could be reduced at all points with equal weighting except for mounting point MPB2. This is because of the orientation the phase angle of MPB2 with respect to the phase of MPB3 as shown in Figure 7.7(b). For this experiment, the phase angle of MPB3 was used as a reference. Even with assigning a negative weight to MPB2 meant it would be on the other end of the stability margin. Hence, a negative weight is assigned as well as a slight shift in the phase angle was made so that it would be in the stability range of the mixed phase angles as shown in Figure 7.7(b). With this weight correction, a reduction

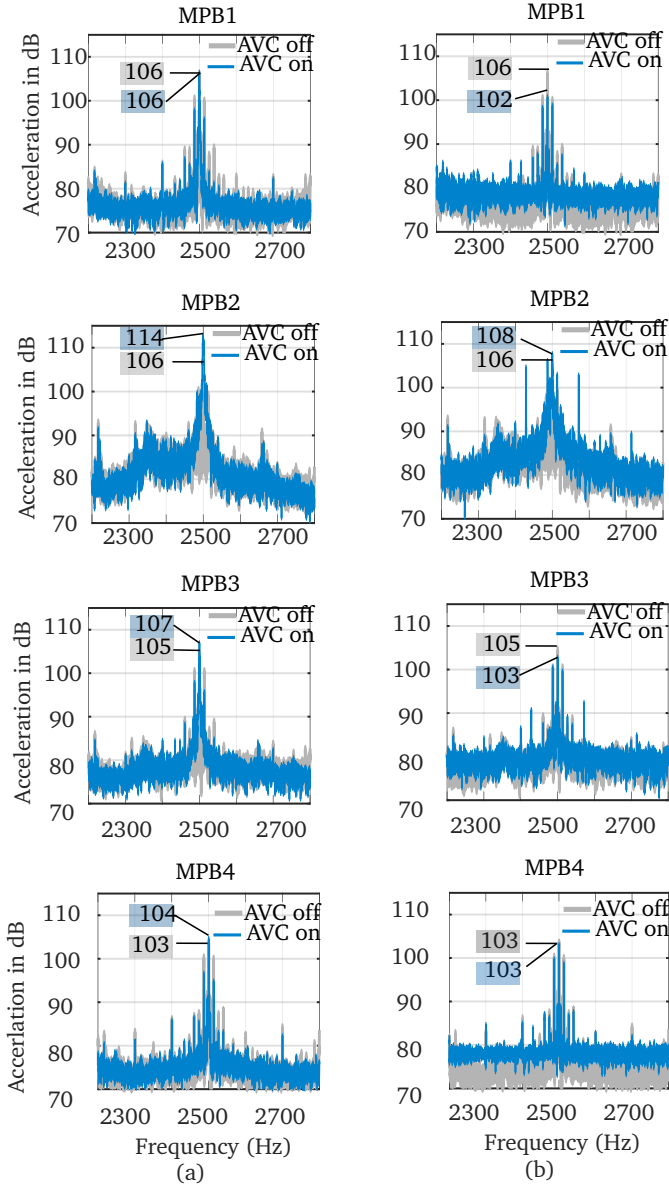


Figure 7.6: Switched error FxLMS validation on mounting points on transverse case
 MPBs:Left side (a): $t_s = 0.1\text{ s}$; Right (b): $t_s = 0.001\text{ s}$

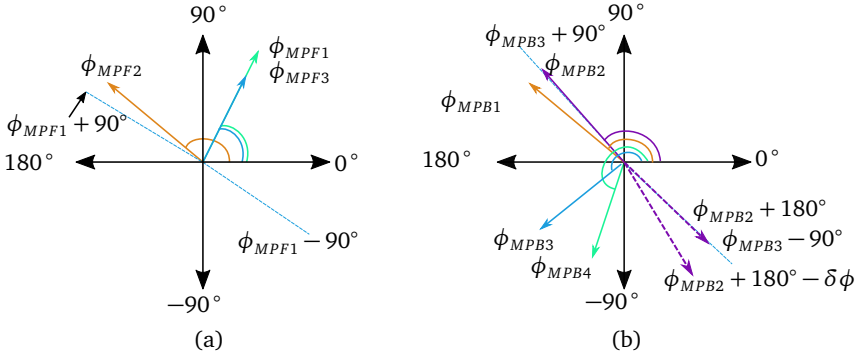


Figure 7.7: Weighting of mixed-errors at 2500 Hz. Left (a): Phase of secondary path for mounting points MPFs. ; Right (b): Phase of secondary path for mounting points MPBs.

in vibration at mounting MPB2 of 4 dB could be achieved.

Another solution could have been to use MPB4 as the reference and then negatively weight the MPB1 and MPB2 phase angles. Therefore there are various possibilities to obtain the mixed-error.

7.1 Comparison of algorithms

To summarize and compare the performance of the control algorithms introduced in this chapter, the assessment is made on different aspects. Firstly the summary of vibration reduction achieved at all the mounting point is presented in Figure 7.10. The summary here is presented for the weighed SIMO, Switched-error with $t_s = 0.001$ s and weighted mixed-error algorithms. It can be seen that, mixed-error algorithm provides the greatest reductions at the mounting points.

Computational complexity is calculated in the order of number of multiplication operations performed for each of the algorithms. In digital computation, multiplications are more resource intensive as they consist of multiple additions hence only the number of multiplications are listed out in the steps in each algorithm listed in Table 7.1. As mentioned before $n_s = 7$ represent the total number of error sensors. The number of reference signals used is denoted by $n_r = 2$, since only sine and cosine components of the input RPM are used in signal $X_n(t)$. Number of actuators here is $n_a = 1$ with two coefficients of the control voltage. All calculations are presented for one actuator input.

The algorithms are then compared on aspects such as computational complexity, number of parameters to tune and stability criteria in Table 7.1. In the second column, the

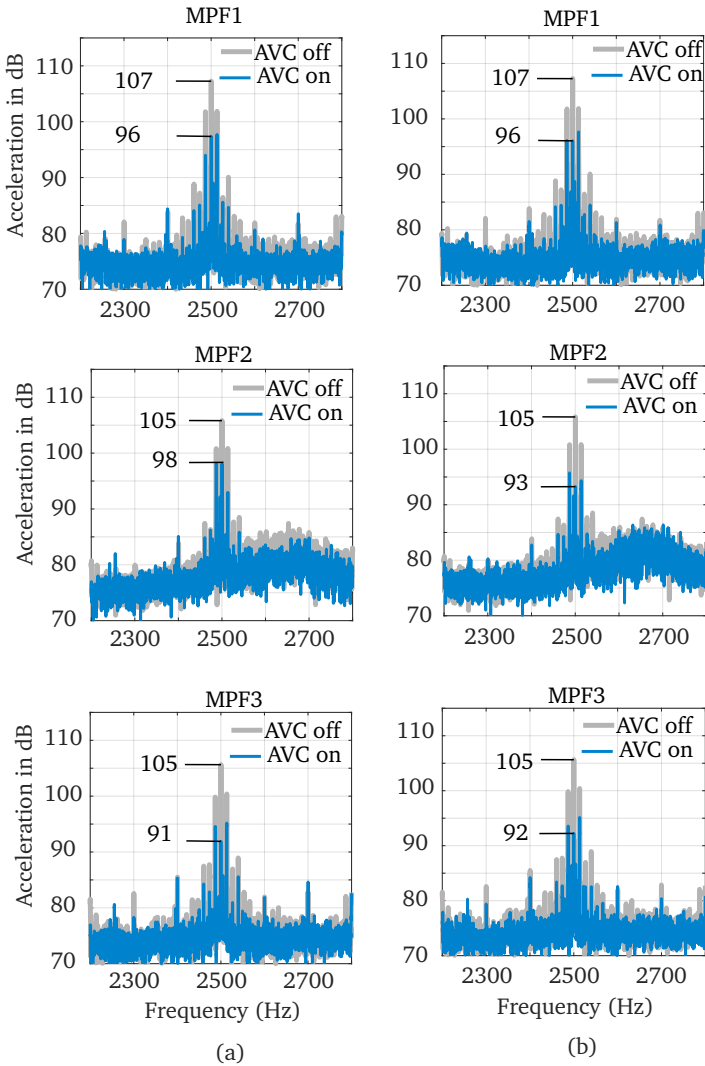


Figure 7.8: Mixed-error FxLMS validation on mounting points on clutch case MPFs. Left side (a): Mixed with equal weights, i.e. $w_k = 1$; Right (b): Mixed with weights according to Equation 6.11

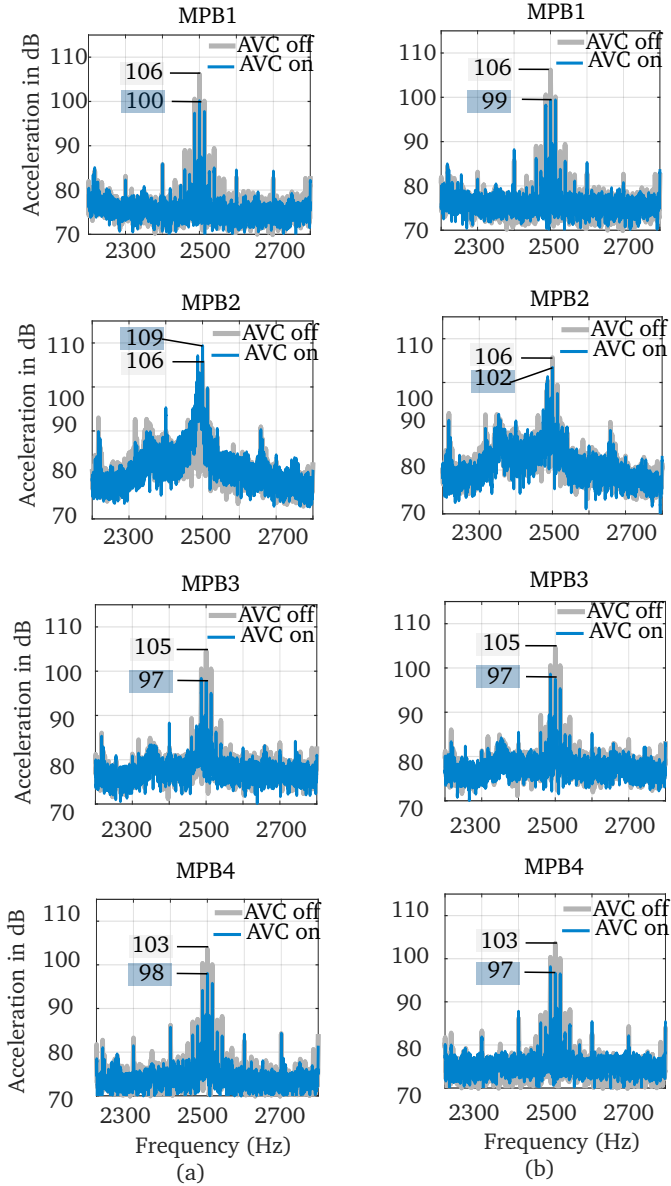


Figure 7.9: Mixed-error FxLMS validation on mounting points on transverse case MPFs. Left side (a): Mixed with equal weights, i.e. $w_k = 1$; Right (b): Mixed with weights according to Equation 6.11

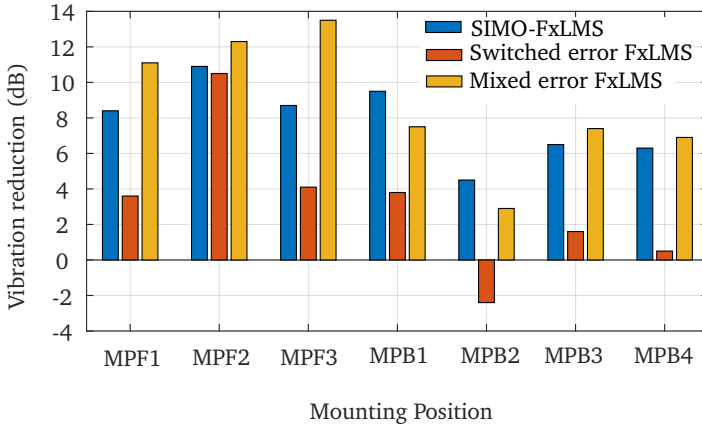


Figure 7.10: Summary of vibration reduction achieved at 2500Hz using the three control algorithms (negative value indicates increase in vibration)

Table 7.1: Number of multiplication operations in each control algorithm

Algorithm	Step 0	Step 1	Step 2	Step 3
	Calculation of error signal	Calculation of filtered secondary path	Gradient Update	Calculation of voltage output
SISO-FxLMS Baseline	-	2	2	2
SIMO-FxLMS		$2 \times n_s$	$2 \times n_s$	2
Switched-error FxLMS	-	2	2	2
Mixed-error FxLMS	n_{mix}	2	2	2

computational complexity is obtained by adding the rows in Table 7.1 for each algorithm. It is noted here that the computational complexity of mixed-error algorithm is calculated using $n_{mix} = 4$ as a conservative case.

Table 7.2: Summary control algorithm comparison; All calculations carried out for $n_s = 7$ number of mounting points to be controlled

Algorithm	Computational complexity	Parameters to tune	Robustness criteria
SIMO-FxLMS	30	7 weights, 7 phase angles	For each $\phi_{ki,n}$ the estimated value should be within $\pm 90^\circ$ of the actual delay
Switched-error FxLMS	6	7 phase angles	same as SIMO
Mixed-error FxLMS	10	1 phase angle per mix, 4 weights in the mixed-error	For each $\phi_{mix,n}$ the estimated value should be within $\pm 90^\circ$ of the all the mixed sensors

As an overview from the analysis, the mixed-error algorithm offers the best solution due to best performance, low parameters to tune and compared to SIMO-FxLMS. Although, the switched-error is least computationally intensive, the number of parameters to tune simultaneously makes it the next best option.

7.2 Projected FxLMS algorithm

There is an apparent drawback in the previous three algorithms discussed in this chapter. All points that are to be controlled need to be actively monitored with a sensor. This contributes to additional cost of the system and could be infeasible for industrial applications. In the given scenario, that a correlated model of the gearbox is available, the opportunity of predicting responses of unmeasured points can be leveraged. This gives rise to the idea of Projected Error FxLMS. The main idea is to predict the value of vibration at the targeted point of vibration reduction and use this for control.

Using the transmissibility concept presented in Section 3.2, the primary path vibration

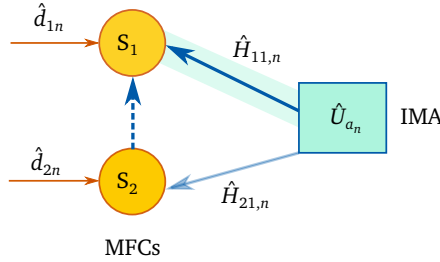


Figure 7.11: Schematic of Projected -Error FxLMS Algorithm, vibration at S_2 is predicted from S_1

at S_2 is predicted from S_1 . The prediction of vibration at S_2 is given as follows:

$$\hat{d}_{2,pred}(t) = TF_{S21} * \hat{d}_{1n}(t) \quad (7.1)$$

The quantity $TF_{S21,n}$ represents the transmissibility of primary path vibrations between S_1 and S_2 given as $\frac{\hat{D}_{2n}\hat{D}_{2n}^*}{\hat{D}_{1n}\hat{D}_{1n}^*}$, where \hat{D}_{1n} and \hat{D}_{2n} are Laplace transformations of $\hat{q}_{1n}(t)$ and $\hat{q}_{2n}(t)$ respectively. \hat{D}^* represents the complex conjugate. It should be noted that this approach can be used to predict multiple sensors from a single reference sensor S_1 , but the example with only one sensor is presented here.

The total vibration at S_2 predicted from S_1 under the influence of control is given by:

$$\begin{aligned} \hat{q}_{2,proj} &= \hat{d}_{2,pred}(t) + \hat{H}_{21,n} * \hat{U}_{a_n}(t) \\ &= TF_{S21,n} * \hat{d}_{1n}(t) + \hat{H}_{21,n} * \hat{U}_{a_n}(t) \\ &= TF_{S21,n} * (\hat{q}_1(t) - \hat{H}_{11,n} * \hat{U}_{a_n}(t)) + \hat{H}_{21,n} * \hat{U}_{a_n}(t) \text{ from Equation 6.6} \end{aligned} \quad (7.2)$$

Using the above equations in frequency domain and writing the prediction in terms of total vibration at S_1 :

$$\hat{Q}_{2,proj} = TF_{S21,n} * \hat{Q}_{1n} + (\hat{H}_{21,n} - TF_{S21,n}\hat{H}_{11,n})\hat{U}_{a_n} \quad (7.3)$$

Due to the prediction capability, the sensor S_2 can be eliminated, thereby reducing the number of actively mounted sensors on the gearbox. There are two main ideas based on which the reference sensor S_1 is selected so that vibration at the required sensor S_2 can be predicted accurately:

1. Physical proximity: S_1 and S_2 being close to each other ensures there is not much change in the secondary path influence and also the transmissibility $TF_{S21,n}$ is close to 1. This will ensure that the behaviour of S_2 is exactly same as S_1 according to Equation 7.3. Therefore no additional parameters need to be calculated for S_2 .

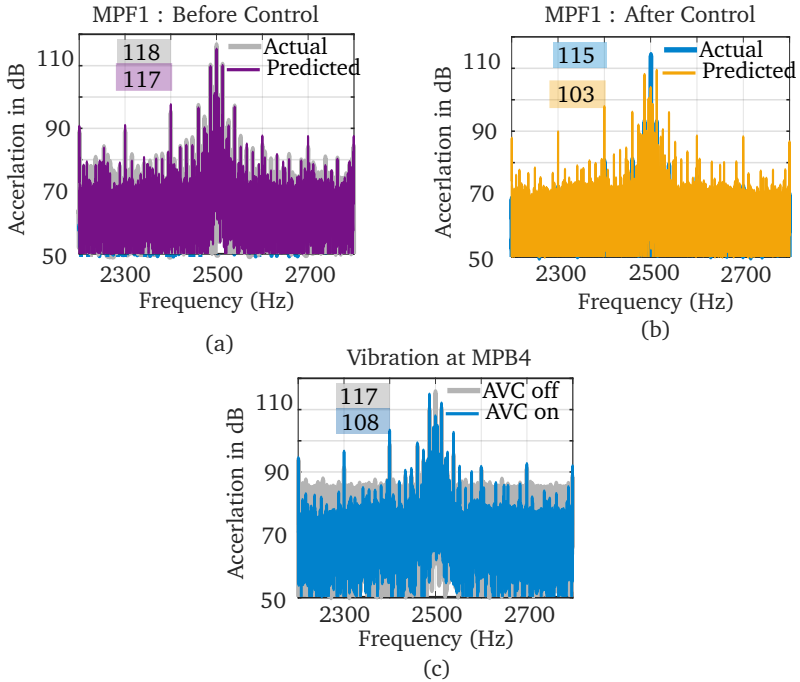


Figure 7.12: Projected Error with MPB4 as reference and controlling MPF1

2. Minimal actuator influence on S_1 : In contrast to the above reasoning, if the active control cancels the vibration at S_1 , then according to Equation 7.3, the prediction of vibration at S_2 will be zero. This will halt the adaptation of control voltage, although actual vibration at S_2 is still present.

Following the second idea, the projected error FxLMS is applied to the demonstration gearbox to control the vibration at MPF1 (S_2). The reference sensor chosen is MPB4 so that actuator influence is minimal in comparison to other mounting points, because it had the least magnitude of the secondary path transfer function. It can be seen from Figure 7.12(a), the vibration at MPF1 before control was predicted with reasonable accuracy. After the control was activated, the prediction stated that the vibration went down to 103 dB, while in reality the vibration was 115 dB. This discrepancy arises because the vibration at reference sensor MPB4 itself was reduced by a great amount (by 9 dB), which lead to erroneous prediction after the control was activated.

Even though the proposed projected algorithm presents a promising way of reducing

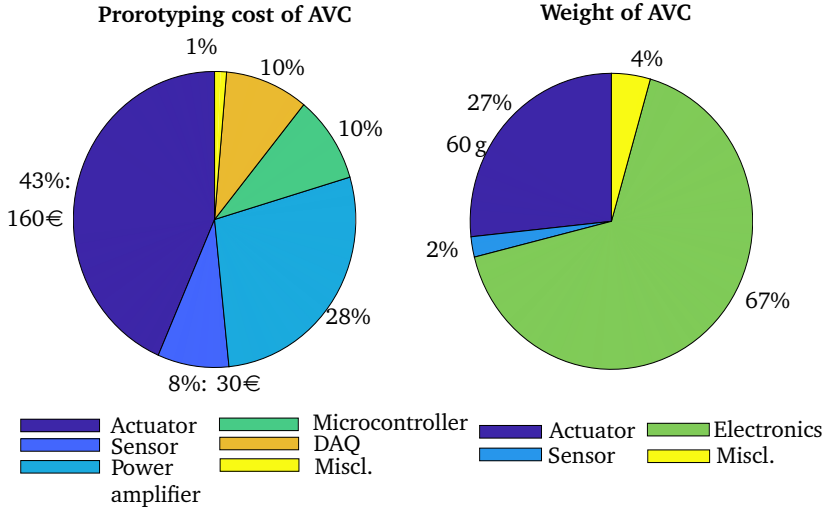


Figure 7.13: Cost (left) and Weight (right) analysis of the designed AVC system

cost in an active vibration control system, inherent disadvantages like the inability to predict the vibration accurately upon activation of control makes is undesirable to use at high frequencies. Looking for a position with minimal actuator influence so that the second part of Equation 7.3 can be purely be determined from the controlled sensor position, is highly unlikely for a complicated system like a transmission.

7.3 System level economics

The developed system level model can be used to develop an active vibration control system for any kind of transmission or gearbox by replacing the dynamic model in the UUT block. In fact, this is also applicable to any mechanical system for example a beam, plate, etc. Several control algorithms can be tested in the same system-level and simultaneously various control actuators can be integrated to prove their concepts before even proceeding to the hardware prototyping stage. This kind of plug and play modelling at system level enables accelerated the product design process for next generation products of a series production.

The costs of the system is depicted in Figure 7.13 and is analysed for prototyping stage. The prototype development incurred a cost of 360€. Each of the sensors costs 35€ per piece (Source : Smart Material website), however mass production up to 100

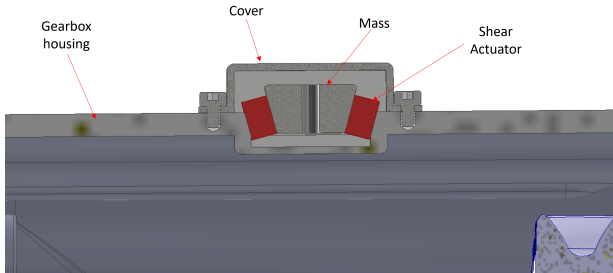


Figure 7.14: Schematic showing the integration of the proposed dual mode shear actuator in the gearbox housing

units can bring down its costs to 5€ per piece (as per quote provided by Smart Material GmbH). 71 % of the costs are incurred by the actuator and the power amplifier. These costs therefore need to be optimized for series production.

The total mass added to the transmission with the current developed AVC concept was estimated to be about 225 g out of which the actuator weighs about 60 g, which is considered of importance in terms of the added weight implications to a lightweight transmission.

Cost reduction strategies

1. **Sensor:** There are two ways, the cost associated with the sensors can be reduced. One way is to perform an optimisation of the number of sensors which would lead to minimum number of sensors that could predict the vibration at the mounting points accurately. Sensors can be miniaturised and embedded in the bolting connections of the mounts if needed. An optimisation of the number of sensors can also be performed which has been demonstrated as part of a publication [100].
2. **Actuator:** Another integrated concept of actuator based on dual mode shear actuator was proposed as a part of the research of the collaborating researcher in the project. Directly using the housing thickness as the inertial mass would be both cost effective and would not add any additional weight to the gearbox. This actuator principle is shown in Figure 7.14.
3. **Miscellaneous electronics:** The microcontroller including the signal conditioning circuit and the power electronics can be merged into the TCU for compact electrical integration. This can help to reduce the PCB prototyping indicating the miscellaneous cost in Figure 7.13.



8 Conclusions and outlook

In this thesis, each of the Chapters 3 to 6 dealt with sequentially building an active vibration control system to efficiently control the vibrations transferred from the mounting points of a gearbox housing. The thesis systematically addressed each subsystem of the system-level model in sequential chapters. Prior to the development of each subsystem, a comprehensive analysis of the state-of-the-art was conducted, encompassing relevant tools and algorithms.

The main results and contributions of this thesis are summarized by addressing the research questions introduced in Chapter 1, Section 1.4. This approach provides a structured overview of the key insights and advancements achieved through this research work.

RQ 1: Modelling approach

The goal of the modelling of gear-whine was two fold. One was to model the level of vibrations generated on the housing due to gear whine. The second was to generate a system level model to provide a unified modelling approach for the development of the AVC system, specifically in regards to the actuator design and its placement.

In Chapter 1, two main models were introduced: the prototype gearbox and the demonstration gearbox. From the review of state of art of modelling approaches, it was established that Finite-Element approaches were still suitable for quantifying frequency ranges 500 - 5000 Hz. For the prototyping gearbox, although no realistic excitation was imposed, comparable levels of vibration were able to be reproduced using the artificial piezo-exciter. The experimental method however revealed that only the vibrations up to 2000 Hz, transferred to the housing structure via the bearing while the high frequency vibrations transferred through the test-rig fixture. The accuracy of prediction of vibration peaks matched the resonances observed from experimental data. Mismatch in the magnitude was attributed to the simplification of the contacts and boundary conditions.

For the demonstration gearbox, however it was possible to test with real-operating conditions with rotating gears. Romax was chosen to be the best analysis tool for modelling the high frequency gear whine. Due to the implicit nature of the gear whine excitations, the correlation of the developed model was performed using transmissibility function with the EOL position as the reference sensor. Major resonances correlated well with experiment and the model at all the measured points. However due to the stated assumptions and simplifications made to the model, deficiencies in predicting gearbox housing vibration in certain frequency ranges were identified.



Another major outcome of the modelling of the gearbox housing vibrations was the need for a single model for the AVC development. Since the control actuator would be mounted on the housing and would not interfere with gear-whine transfer path, the secondary path model was not affected by the operational condition (speed and torque in operation) of the gearbox. Hence, only one single model was needed to develop further subsystems of the AVC system.

RQ 2: Actuator force requirements

In Section 3.1.4, using the model of the prototyping gearbox. It was determined that most of the vibrations lie in the frequency range of 1500 - 5000Hz. The result of the analysis of mounting point vibration showed that an actuator that could generate a force of 100N on the housing in this frequency range would be suitable to control the vibration at the mounting points.

In parallel investigation of this study within the framework of the project, it was proven that piezoelectric inertial mass actuators were ideal in generating this level of forces while adding minimal weight to the system. Hence, the further development of the actuator was performed with the established requirement. The design of the actuator however was not in the scope of this thesis.

RQ 3: Alternate sensing approach

In review of the industrially accepted sensors for measuring vibrations, it was found that MFCs were the most suitable components to establish a sensing scheme for a complex geometry like an automotive gearbox. Due to their conformability to complex surfaces and high bandwidth they were chosen as sensors to capture the structure borne vibrations. Based on the comparison of MFC types, the M0714P2 type was chosen for this study. A charge amplifier circuit was built that converted the charge to readable voltage output in the range of 0 - 2.5V. The microcontroller based data acquisition system can read and record these values at a sampling frequency of up to 25 kHz. This data acquisition unit can be easily integrated into the existing Transmission Control Unit (TCU) in the vehicle.

A systematic calibration of the MFCs was performed to predict the vibrations at the mounting points in terms of acceleration using the transfer function given by Equation 4.13. The decision of selecting MFCs was based on the cost to utility benefit provided by the number of sensors that would be used in the AVC system. Despite their low cost, the reliability and seamless integration into the gearbox housing proved beneficial of their usage for measuring high frequency gearbox vibrations.

RQ 4: Actuator position

The inclusion of actuator dynamics with the gearbox model proved important to consider due to the coupling of dynamics at the actuator attachment point. Adding the spatial



dimension to the controllability concept proved effective in determining the actuator position. The process of selecting an actuator position described in Chapter 5, was ultimately based on the modal and spatial controllability scores. The derivation of a single actuator and 2- actuator combination was derived systematically. The derivation of position was compared with the strategy applied to the experimentally derived secondary path transfer function. Even though the secondary path transfer functions were not perfectly accurate with experiment due to the generalisation of the joint stiffness, it did not effect the position derived. Same position could be derived for single and 2-actuator layouts.

RQ 5 : Control Algorithm

The control algorithm and data acquisition were deployed in hardware using a 600 MHz microcontroller development board. This called for implementation of control algorithms that had low computational complexity to achieve the simultaneous control and data acquisition at a high rate of 20 kHz.

Based on the SISO-FxLMS, three algorithms were compared for multipoint control in Chapter 6. The SIMO-FxLMS served as a baseline for comparison for the proposed switching and mixed error algorithms. In each of the algorithms, the relevant parameters were analysed in detail. For the SIMO algorithm, the weighting of the error sensors as a function of the secondary path transfer function improved its vibration reduction performance.

Both the mixed and switching error algorithms simplified the SIMO-FxLMS into a SISO-FxLMS thereby reducing the computational complexity by more than half in each case. For the switched error algorithm, using a faster switching time provided better vibration reduction performance but at the expense of slow convergence in adaptation of control coefficients in the order of 5 - 10 s.

For the mixed-error, in addition to the weights calculated similar to the SIMO-FxLMS approach, the sign assigned to each individual weight was also important for the stability and performance of the algorithm. From overall comparison of the three algorithms, mixed-error algorithm provided the best computational complexity to performance benefit.

The projected error control algorithm was introduced based on remotely predicting the vibration at the desired control location. This algorithm promised the reduction of the number of sensors to be actively placed on the gearbox. The limitations of erroneous predictions at high frequency vibrations was shown. This proved that the projected-error algorithm was ineffective by using only one reference sensor. Further optimisation of number of sensors and their positions is necessary to exploit the full potential of this algorithm using the system level model.

RQ 6 : System level economics

The developed system level model can be used to develop an active vibration control system for any kind of transmission or gearbox by replacing the dynamic model in the UUT block. In fact, this is also applicable to any mechanical system for example a beam, plate, etc. Several control algorithms can be tested in the same system-level and simultaneously various control actuators can be integrated to prove their concepts before even proceeding to the hardware prototyping stage. This kind of plug and play modelling at system level accelerates the product design process for next generation products of a series production.

Given the trade off of vibration increase with about 1 kg reduction in gearbox weight with the use of lightweight materials, the addition of 225 g with the developed AVC represents a lesser percentage of increase in weight, given the functional benefit. Out of the electronics, the power amplifier contributes to the majority of the weight, where there is great scope for optimization and integration into the current on-board electronics.

Outlook and future work

The study performed in this thesis identified major avenues for development of the AVC as future work. From the modelling point of view, the commercial software could implement the damping update routine as demonstrated in Chapter 3. Also the consideration of inertia and apparent stiffness of the neglected components of the gearbox could be implemented in future iterations of the software update.

MFCs could not only be used as sensors but also effective actuators. There are studies undertaken to have MFCs as actuators themselves [106] proving some potential for application of these elements as actuators for high frequency structure borne vibrations. Since the inertial effect to produce the external force similar to the IMA is lacking in an MFC, careful design and integration of it in the structure needs to be undertaken. One such example is demonstrated in the thesis of Schmitt [113], where the author stacked multiple piezo-foil actuators to generate a direct excitation at the gear-tooth. Similar direction could be undertaken, keeping in mind the cost factor of using multiple actuators.

The major aim in Chapter 6 was to provide simplifications to the already established multi-point control methods based on the basic FxLMS algorithms with nominal step size and known secondary path transfer function. However, there are several variations in terms of variable step-size and online secondary path identification methods applied in literature which have not been addressed in this thesis. As a future direction the switched error and mixed error algorithms can be developed further with online phase identification or even model-free methods.

The mixed error approach was independently testing on mounting points on the clutch case and transverse case. Another possibility of investigation is the simultaneous application of mixed error on mounting points on the clutch and transverse case and employing either SIMO or switched error algorithm.

The projected error algorithm proposed at the end of Chapter 6, still provides some

potential to implement with relevant virtual sensing techniques and reference sensor optimisation. However a detailed investigation into both the approaches needs to be undertaken.

The active vibration control system developed as part of this thesis is not only restricted to automotive transmissions. It can be extended to any kind of vibrating structure where the vibrations need to be monitored actively.



A Hardware details of developed AVC system

A.1 Sensor data and actuator data

Piezoelectric Accelerometer	86450AT from KISTLER IEPE Range : $\pm 5g$ Sensitivity : 1000 mV g^{-1} Resonance frequency : 17 kHz Mass : 3.5 g
Macro fibre composite	MFC0714P1 from SMART MATERIAL Capacitance: 11 nF Dimension : 7 mm \times 14 mm Piezoelectric coefficient d_{31} : 170 pC/N
Inertial Mass Actuator	PA4FLW from THORLABS Maximum driving voltage : 150 V Piezoelectric stack dimensions : 5 mm \times 5 mm \times 5 mm Dimensions of the IMA : ϕ 25 mm \times 20 mm Blocking Force (N) : 1000 N Piezoelectric stack stiffness : $180 \text{ N } \mu\text{m}^{-1}$ Piezoelectric stack capacitance : 460 50 nF Displacement (Free Stroke) at 150 V : 6.1 15 μm IMA weight : 59.6 g

A.2 Data Acquisition (DAQ) board

The data acquisition was performed using a board custom developed for this thesis. The acquisition and control algorithms are deployed using a Teensy 4.1 microcontroller development board. The ADC on this board is limited to 10bit, hence an external ADC consisting of 8 channels is used. The 8 signal conditioning units based on the circuit shown in Figure 4.6 are highlighted in Figure A.1. The microcontroller also lacks a Digital to Analog Converter, hence an external DAC is incorporated in the board which can support upto two actuators simultaneously. The DAQ board can be powered externally with 15 - 20 V power. All the data is stored on an SD card that can be accessed via the USB cable.

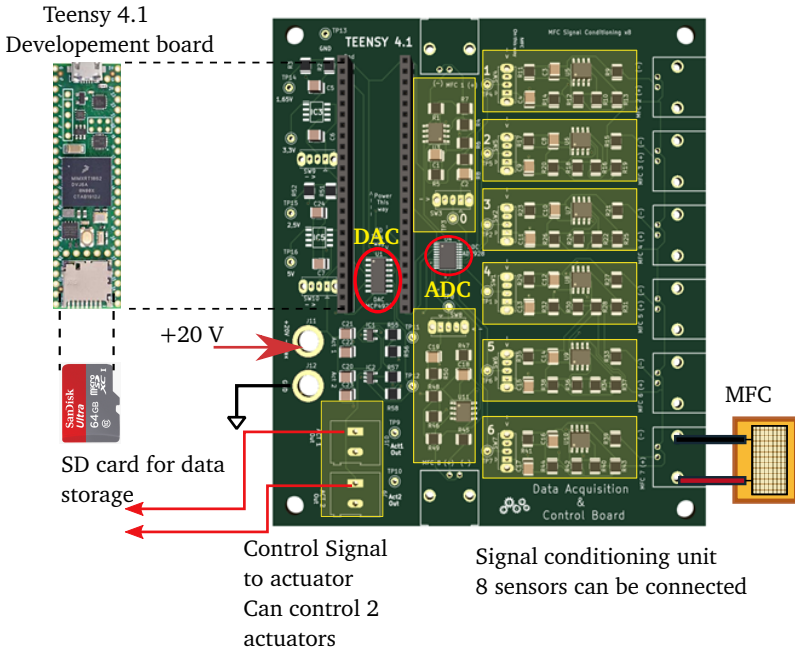


Figure A.1: DAQ Board schematic

A.3 Details of IC chips used

Analog to Digital Converter	AD7928 from ANALOG DEVICES
	Range : 0 - 2.5V
	Channels : 8
	Resolution : 12 - bit
	Single-supply operation: 2.7 - 5.5V
	Throughput rate: : 1 MSPS
	Interface : SPI

Digital to Analog Converter	MCP4922 from MICROCHIP TECHNOLOGY
	Range : 0 - 3.3V
	Resolution : 12 - bit
	Single-supply operation: 2.7 - 5.5V
	Throughput rate: : 1 MSPS
	Interface : SPI



B MADYN analysis for bearing stiffness

In this chapter, a short overview of the analysis of the load dependent behaviour of the bearings in the static test-rig is presented.

The model of the gear train of the static test-rig was built in MADYN 2000, extensive rotor-dynamic program, which is suited for general rotor-gear-bearing systems for lateral, torsional and coupled analyses with all types of bearings [2]. The aim here is to simulate the load dependant nature of the bearings in the gear-train of the 7DCT300 gearbox for correlating the modal damping of the test-rig.

The bearing positions are shown in Figure B.1

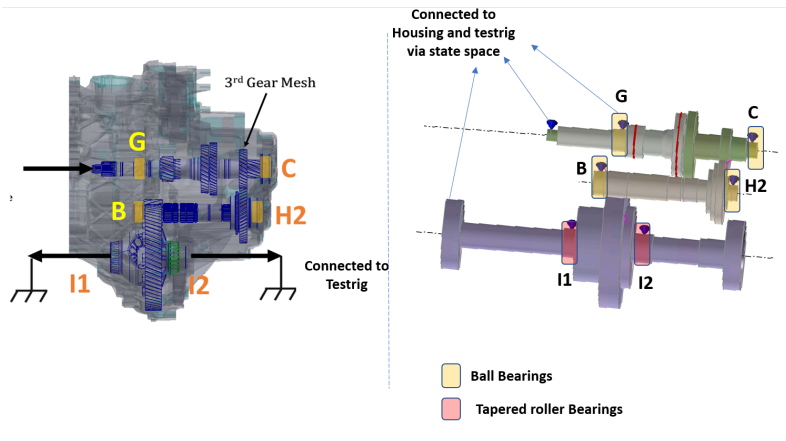


Figure B.1: Bearing nomenclature in Prototyping gearbox

The housing and test rig frame is also included in the analysis via ANSYS SPMWrite export into MADYN2000. Dynamic analysis model of the whole gearbox is linearised at each input torque case, using load dependent bearing properties. The static analysis performed on the shaft interpolate the bearing stiffness behaviour. Bearing outer ring is fixed in the housing while the inner ring will deflect in radial or axial direction.

The bearing stiffness matrix used in rotor dynamics is a 5×5 matrix, contains useful

information of bearing stiffness like radial stiffness, axial stiffness and tilting stiffness. It can be represented as:

$$K_{bea} = \begin{bmatrix} K_{11} & K_{12} & K_{13} & K_{14} & K_{15} \\ K_{21} & K_{22} & K_{23} & K_{24} & K_{25} \\ K_{31} & K_{32} & K_{33} & K_{34} & K_{35} \\ K_{41} & K_{42} & K_{43} & K_{44} & K_{45} \\ K_{51} & K_{52} & K_{53} & K_{54} & K_{55} \end{bmatrix} \quad (B.1)$$

where the directions 1 and 2 are the radial directions in the plane (also indicated as X and Y as shown in Figure B.2 and 3 represents the axial direction. 4 and 5 are the angular deflections around the 1 and 2 axes respectively.

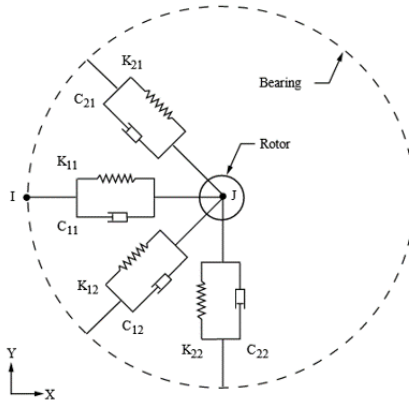


Figure B.2: Bearing stiffness nomenclature in prototyping gearbox

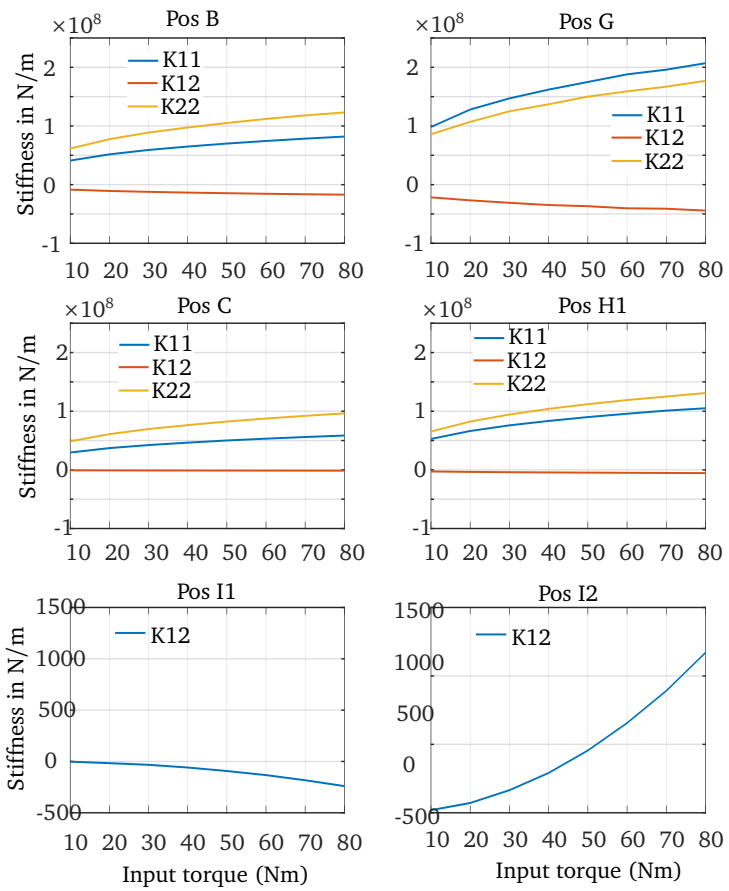


Figure B.3: Bearing stiffness results at various static input torque levels



C References

References

- [1] O. Abidi, M. Hached, and K. Jbilou. “A global rational Arnoldi method for model reduction”. In: *Journal of Computational and Applied Mathematics* 325 (2017), pp. 175–187. ISSN: 0377-0427. DOI: <https://doi.org/10.1016/j.cam.2017.05.003>.
- [2] Delta JS AG. *MADYN 2000 for Rotordynamics*. <https://www.delta-js.ch/en/software/madyn-2000-for-rotordynamics/index.html>. 6/3/2024.
- [3] H.R. Ahmadi and A.H. Muhr. “Vibration control using rubber components”. In: *International Journal of Materials and Product Technology* 7.1 (1992), pp. 65–88. DOI: 10.1504/IJMPT.1992.036500. eprint: <https://www.inderscienceonline.com/doi/pdf/10.1504/IJMPT.1992.036500>.
- [4] D. R. Amaral et al. “Lightweight gearbox housing with enhanced vibro-acoustic behavior through the use of locally resonant metamaterials”. In: *Applied Acoustics* 210 (2023), p. 109435. ISSN: 0003-682X. DOI: <https://doi.org/10.1016/j.apacoust.2023.109435>.
- [5] P. Ambrosio, F. Resta, and F. Ripamonti. “An H2 norm approach for the actuator and sensor placement in vibration control of a smart structure”. In: *Smart Materials and Structures* 21.12 (2012), p. 125016. ISSN: 1361-665X. DOI: 10.1088/0964-1726/21/12/125016.
- [6] Paulo Antunes et al. “SHM TB30-Numerical Study of an Aircraft Structural Condition”. In: 2019.
- [7] N. Aouf, B. Boulet, and R. Botez. “Model and controller reduction for flexible aircraft preserving robust performance”. In: *IEEE Transactions on Control Systems Technology* 10.2 (2002), pp. 229–237. ISSN: 10636536. DOI: 10.1109/87.987068.
- [8] A. Armaou and M. Demetriou. “Using spatial H2 norm for sensor placement in parabolic partial differential equations”. In: *2006 American Control Conference* (2006).
- [9] Ashley L. Dunn, Donald R. Houser, and Teik C. Lim. “Methods for Researching Gear Whine in Automotive Transaxles”. In: SAE International, 1999. ISBN: 2688-3627. DOI: 10.4271/1999-01-1768.

-
- [10] S. Asiri, A. Baz, and D. Pines. “Periodic Struts for Gearbox Support System”. In: *Journal of Vibration and Control* 11.6 (2005), pp. 709–721. DOI: 10.1177/1077546305052784. eprint: <https://doi.org/10.1177/1077546305052784>.
- [11] Limna S. Attoor and Mahmoud Al Ahmad. *Piezoelectric Coefficient Characterization Using Combined Electrical and Light-Based Methodology*. 2023. DOI: 10.1109/access.2023.3295784.
- [12] AVL. *AVL PUMA Open 2TM - The ease of automation*. <https://www.avl.com/de/presse/press-release/avl-puma-open-2-ease-automation>. 6/3/2024.
- [13] Peter Benner et al. “Novel Model Reduction Techniques for Control of Machine Tools”. In: 2009.
- [14] B. Besselink et al. “A comparison of model reduction techniques from structural dynamics, numerical mathematics and systems and control”. In: *Journal of Sound and Vibration* 332.19 (2013), pp. 4403–4422. ISSN: 0022-460X. DOI: <https://doi.org/10.1016/j.jsv.2013.03.025>.
- [15] Mojtaba Biglar et al. “Optimal configuration of piezoelectric sensors and actuators for active vibration control of a plate using a genetic algorithm”. In: *Acta Mechanica* 226.10 (2015), pp. 3451–3462. ISSN: 0001-5970. DOI: 10.1007/s00707-015-1388-1.
- [16] Li Bin et al. “Maximal Modal Force Rule for Optimal Placement of Point Piezoelectric Actuators for Plates”. In: *Journal of Intelligent Material Systems and Structures* 11.7 (2000), pp. 512–515. DOI: 10.1106/DE9J-B8Y5-1T4U-UM09.
- [17] Dariusz Bismor, Krzysztof Czyz, and Zbigniew Ogonowski. “Review and Comparison of Variable Step-Size LMS Algorithms”. In: *The International Journal of Acoustics and Vibration* 21 (2016), pp. 24–39. DOI: 10.20855/ijav.2016.21.1392.
- [18] Uli Christian Blessing et al. “Scalable hybrid dual-clutch transmission”. In: *Auto Tech Review* 4.9 (2015), pp. 46–51. ISSN: 2250-3390. DOI: 10.1365/s40112-015-0982-x.
- [19] CC Boucher, SJ Elliott, and PA Nelson. “Effect of errors in the plant model on the performance of algorithms for adaptive feedforward control”. In: *IEE Proceedings F (Radar and Signal Processing)*. Vol. 138. IET, 1991, pp. 313–319.
- [20] Rune Brincker and Carlos E. Ventura. *Introduction to Operational Modal Analysis*. Wiley, 2015. ISBN: 9781118535141. DOI: 10.1002/9781118535141.
- [21] I. Bruant and L. Proslie. “Optimal Location of Actuators and Sensors in Active Vibration Control”. In: *Journal of Intelligent Material Systems and Structures* 16.3 (2005), pp. 197–206. ISSN: 1045-389X. DOI: 10.1177/1045389X05047989.

- [22] Isabelle Bruant, Laurent Gallimard, and Shahram Nikoukar. “Optimal piezoelectric actuator and sensor location for active vibration control, using genetic algorithm”. In: *Journal of Sound and Vibration* 329.10 (2010), pp. 1615–1635. ISSN: 0022-460X. DOI: 10.1016/j.jsv.2009.12.001.
- [23] Dariusz Buchczik and Marek Pawelczyk. “Calibration of Accelerometers Using Multisinusoidal Excitation”. In: *Advances in Condition Monitoring of Machinery in Non-Stationary Operations*. Ed. by Anna Timofiejczuk et al. Cham: Springer International Publishing, 2018, pp. 213–222. ISBN: 978-3-319-61927-9.
- [25] Bianca CĂȘERIU and Petruța BLAGA. “ANALYSIS OF INTERIOR NOISE IN SPECIAL PURPOSE VEHICLES”. In: *Review of the Air Force Academy XXI.1* (2023), pp. 33–46. ISSN: 18429238. DOI: 10.19062/1842-9238.2023.21.1.5.
- [26] K. Chen and D.W. Herrin. “Blocked force determination on plate structures using an offset interface”. In: *Applied Acoustics* 158 (2020), p. 107044. ISSN: 0003-682X. DOI: <https://doi.org/10.1016/j.apacoust.2019.107044>.
- [27] Roy R. Craig and M. C. C. Bampton. “Coupling of substructures for dynamic analyses”. In: *AIAA Journal* 6.7 (1968), pp. 1313–1319. DOI: 10.2514/3.4741.
- [28] Sarah Curtis et al. *An Analytical Method to Reduce Gear Whine Noise, Including Validation with Test Data*. 2005. DOI: 10.4271/2005-01-1819.
- [29] Frank Czerwinski. “Current Trends in Automotive Lightweighting Strategies and Materials”. In: *Materials* 14.21 (2021). ISSN: 1996-1944. DOI: 10.3390/ma14216631.
- [30] N. Darivandi, K. Morris, and A. Khajepour. “LQ optimal actuator location in structures”. In: *American Control Conference (ACC), 2012: 27-29 June 2012, Montreal, QC, Canada*. Piscataway, NJ: IEEE, 2012, pp. 646–651. ISBN: 978-1-4577-1096-4. DOI: 10.1109/ACC.2012.6314992.
- [31] Sidharth Dave et al. “A fundamental investigation of the interaction and impact of controlled torque ripples on gear mesh dynamics”. In: *Applied and Computational Mechanics* 17.2 (2023). ISSN: 1802680X. DOI: 10.24132/acm.2023.838.
- [32] Elke Deckers et al. “The wave based method: An overview of 15 years of research”. In: *Wave Motion* 51.4 (2014), pp. 550–565. ISSN: 0165-2125. DOI: <https://doi.org/10.1016/j.wavemoti.2013.12.003>.
- [33] M.A. Demetriou and T. Moghani. “Robust actuator placement in flexible plates subject to worst-case spatial distribution of disturbances”. In: *Proceedings of the 2004 American Control Conference*. Vol. 4. 2004, 3550–3555 vol.4. DOI: 10.23919/ACC.2004.1384462.

- [34] Michael A. Demetriou. “Incorporating spatial frequency weighting and frequency domain methods in integrated actuator and controller design for a class of parabolic partial differential equations”. In: *American Control Conference, 2007. ACC '07*. IEEE / Institute of Electrical and Electronics Engineers Incorporated, 2007, pp. 2072–2077. ISBN: 1-4244-0988-8. DOI: 10.1109/ACC.2007.4282386.
- [35] Arnaud Deraemaeker et al. “Analytical and numerical computation of homogenized properties of MFCs: Application to a composite boom with MFC actuators and sensors”. In: 2007.
- [36] S. Devasia et al. “Piezoelectric actuator design for vibration suppression: placement and sizing”. In: *[1992] Proceedings of the 31st IEEE Conference on Decision and Control*. IEEE, 1992, pp. 1367–1372. ISBN: 0-7803-0872-7. DOI: 10.1109/CDC.1992.371487.
- [37] Christof Devriendt and Patrick Guillaume. “Identification of modal parameters from transmissibility measurements”. In: *Journal of Sound and Vibration* 314.1 (2008), pp. 343–356. ISSN: 0022-460X. DOI: <https://doi.org/10.1016/j.jsv.2007.12.022>.
- [38] K. D. Dhuri and P. Seshu. “Multi-objective optimization of piezo actuator placement and sizing using genetic algorithm”. In: *Journal of Sound and Vibration* 323.3-5 (2009), pp. 495–514. ISSN: 0022460X. DOI: 10.1016/j.jsv.2009.01.007.
- [39] R. S. O. Dias, M. Martarelli, and P. Chiariotti. “Lagrange Multiplier State-Space Substructuring”. In: *Journal of Physics: Conference Series* 2041.1 (2021), p. 012016. DOI: 10.1088/1742-6596/2041/1/012016.
- [40] Runze Ding et al. “An optimal sensor/actuator placement method for flexible structures considering spatially varying disturbances”. In: *Journal of Vibration and Control* 28.23-24 (2022), pp. 3575–3585. DOI: 10.1177/10775463211035893.
- [41] Hans Dresig. *Schwingungen mechanischer Antriebsysteme*. Springer Berlin Heidelberg, 2001. ISBN: 9783662098332. DOI: 10.1007/978-3-662-09833-2.
- [42] Mark Eaton et al. “Use of Macro Fibre Composite Transducers as Acoustic Emission Sensors”. In: *Remote Sensing* 1.2 (2009), pp. 68–79. ISSN: 2072-4292. DOI: 10.3390/rs1020068.
- [43] Christian Ehmann and Rainer Nordmann. “Low Cost Actuator for Active Damping of Large Machines”. In: *IFAC Proceedings Volumes* 35.2 (2002), pp. 179–184. ISSN: 1474-6670. DOI: [https://doi.org/10.1016/S1474-6670\(17\)33938-1](https://doi.org/10.1016/S1474-6670(17)33938-1).
- [44] S. Elliott, I. Stothers, and P. Nelson. “A multiple error LMS algorithm and its application to the active control of sound and vibration”. In: *IEEE Transactions on Acoustics, Speech, and Signal Processing* 35.10 (1987), pp. 1423–1434. DOI: 10.1109/TASSP.1987.1165044.

-
- [45] Larry J. Eriksson and Mark C. Allie. “Use of random noise for on-line transducer modeling in an adaptive active attenuation system”. In: *Journal of the Acoustical Society of America* 85 (1986), pp. 797–802.
- [46] Jan Flek et al. “Determination of Mesh Stiffness of Gear Analytical Approach FEM Analysis”. In: *Applied Sciences* 11.11 (2021). ISSN: 2076-3417. DOI: 10.3390/app11114960.
- [47] Kensaku Fujii et al. “Verification of simultaneous equations method by an experimental active noise control system”. In: *Acoustical science and technology* 27.5 (2006), pp. 270–277.
- [48] Gunnar Gäbel et al. “Development and Implementation of a Multi-Channel Active Control System for the Reduction of Road Induced Vehicle Interior Noise”. In: *Actuators* 7.3 (2018), p. 52. DOI: 10.3390/act7030052.
- [49] Weijin Gao, Liang Wang, and Yongguang Liu. “A modified adaptive filtering algorithm with online secondary path identification used for suppressing gearbox vibration”. In: *Journal of Mechanical Science and Technology* 30.11 (2016), pp. 4833–4843. ISSN: 1738-494X. DOI: 10.1007/s12206-016-1002-z.
- [50] W. Gawronski. “ACTUATOR AND SENSOR PLACEMENT FOR STRUCTURAL TESTING AND CONTROL”. In: *Journal of Sound and Vibration* 208.1 (1997), pp. 101–109. ISSN: 0022460X. DOI: 10.1006/jsvi.1997.1190.
- [51] A. Ghorbel et al. “Modal Analysis and Dynamic Behavior for Analytical Drivetrain Model”. In: *Journal of Mechanics* 34.4 (2018), pp. 399–415. ISSN: 1727-7191. DOI: 10.1017/jmech.2017.23.
- [52] Yuan H. Guan, Teik C. Lim, and W. Steve Shepard. “Experimental study on active vibration control of a gearbox system”. In: *Journal of Sound and Vibration* 282.3-5 (2005), pp. 713–733. ISSN: 0022460X. DOI: 10.1016/j.jsv.2004.03.043.
- [53] Yuan H. Guan et al. “Comparative analysis of actuator concepts for active gear pair vibration control”. In: *Journal of Sound and Vibration* 269.1-2 (2004), pp. 273–294. ISSN: 0022460X. DOI: 10.1016/S0022-460X(03)00072-5.
- [54] Vivek Gupta, Manu Sharma, and Nagesh Thakur. “Optimization Criteria for Optimal Placement of Piezoelectric Sensors and Actuators on a Smart Structure: A Technical Review”. In: *Journal of Intelligent Material Systems and Structures* 21.12 (2010), pp. 1227–1243. ISSN: 1045-389X. DOI: 10.1177/1045389X10381659.
- [55] Thomas Haase, Malte Misol, and Michael Rose. “Optimal placement of flat piezoceramic actuators for feedforward systems under the influence of real-time hardware delays”. In: *Journal of Sound and Vibration* 345 (2015), pp. 34–46. ISSN: 0022460X. DOI: 10.1016/j.jsv.2015.02.009.

- [56] A. Hać and L. Liu. “Sensor And Actuator Location In Motion Control Of Flexible Structures”. In: *Journal of Sound and Vibration* 167.2 (1993), pp. 239–261. ISSN: 0022-460X. DOI: <https://doi.org/10.1006/jsvi.1993.1333>.
- [57] Stephen Hambric. “Structural Acoustics Tutorial—Part 1: Vibrations in Structures”. In: *Acoustics Today* 2 (2006). DOI: 10.1121/1.2961142.
- [58] S Haykin. “Adaptive filter theory”. In: *Adaptive filter theory*. 1996, pp. 989–989.
- [59] K Hiramoto, H Doki, and G Obinata. “Optimal sensor/actuator placement for active vibration control using explicit solution of algebraic Riccati equation”. In: *Journal of Sound and Vibration* 229.5 (2000), pp. 1057–1075.
- [60] P Hughes and D. McCormick. “Boundary Element Method for Vibration Analysis of Gearbox Housing”. In: *Journal of Sound and Vibration* 329.24 (2010), pp. 4954–4967. DOI: 10.1016/j.jsv.2010.06.012.
- [61] Takanori Ide et al. “Structural optimization methods of nonlinear static analysis with contact and its application to design lightweight gear box of automatic transmission of vehicles”. In: *Structural and Multidisciplinary Optimization* 53.6 (2016), pp. 1383–1394. ISSN: 1615-1488. DOI: 10.1007/s00158-015-1369-y.
- [62] Institut für Mechatronische Systeme – TU Darmstadt. *IMS Connect*. https://www.ims.tu-darmstadt.de/industrie_1/pruefsstaende_1/antriebsstrangpruefstand_connect_/IMSConnect.de.jsp. 6/3/2024.
- [63] Lars A. L. Janssen et al. “Mode selection for component mode synthesis with guaranteed assembly accuracy”. In: *Journal of Sound and Vibration* 589 (2024), p. 118596. ISSN: 0022-460X. DOI: <https://doi.org/10.1016/j.jsv.2024.118596>.
- [64] Lin Ji et al. “A review of mid-frequency vibro-acoustic modelling for high-speed train extruded aluminium panels as well as the most recent developments in hybrid modelling techniques”. In: *Journal of Modern Transportation* 23.3 (2015), pp. 159–168. ISSN: 2196-0577. DOI: 10.1007/s40534-015-0080-4.
- [65] Y. Kajikawa and Y. Nomura. “Active noise control without a secondary path model by using a frequency-domain simultaneous perturbation method with variable perturbation”. In: *2003 IEEE International Conference on Acoustics, Speech, and Signal Processing, 2003. Proceedings. (ICASSP '03)*. Vol. 5. 2003, pp. V–580. DOI: 10.1109/ICASSP2003.1200036.
- [66] Ashish Kanase, Yogiraj Mane, and Amey Kulkarni. “Manual Gearbox Gear Whine Noise Prediction and Importance of Parametric Sensitivity in NVH”. In: *SAE Technical Paper Series*. SAE Technical Paper Series. SAE International400 Commonwealth Drive, Warrendale, PA, United States, 2013. DOI: 10.4271/2013-26-0091.

- [67] Dhanaraja Kasinathan and Kirsten Morris. “Convergence of -optimal actuator locations”. In: *2011 50th IEEE Conference on Decision and Control and European Control Conference: (CDC-ECC) ; 12-15 Dec. 2011, Orlando, FL, USA*. Piscataway, NJ: IEEE, 2011, pp. 627–632. ISBN: 978-1-61284-801-3. DOI: 10.1109/CDC.2011.6160732.
- [68] Dhanaraja Kasinathan and Kirsten Morris. “H -Optimal Actuator Location”. In: *IEEE Transactions on Automatic Control* 58.10 (2013), pp. 2522–2535. ISSN: 0018-9286. DOI: 10.1109/TAC.2013.2266870.
- [69] Nicole J. Kessissoglou, Patrik Ragnarsson, and Anders Löfgren. “An analytical and experimental comparison of optimal actuator and error sensor location for vibration attenuation”. In: *Journal of Sound and Vibration* 260.4 (2003), pp. 671–691. ISSN: 0022-460X. DOI: [https://doi.org/10.1016/S0022-460X\(02\)00987-2](https://doi.org/10.1016/S0022-460X(02)00987-2).
- [70] Ellis Kessler et al. “Active vibration control actuator placement for a planetary gearbox based on operational modal analysis”. In: 2019.
- [71] Dong-Chan Kim et al. “Hardware Implementation of High-Speed Active Vibration Control System Based on DSP320C6713 Processor”. In: *Journal of the Korean Society of Marine Engineering* 32.3 (2008), pp. 437–445. ISSN: 2234-7925. DOI: 10.5916/jkosme.2008.32.3.437.
- [72] Robin Kleinwort, Philipp Weishaupt, and Michael F. Zaeh. “Simulation-Based Dimensioning of the Required Actuator Force for Active Vibration Control”. In: *International Journal of Automation Technology* 12.5 (2018), pp. 658–668. DOI: 10.20965/ijat.2018.p0658.
- [73] Xiannian Kong et al. “Effects of gearbox housing flexibility on dynamic characteristics of gear transmission system”. In: *Journal of Vibration and Control* 27.17-18 (2021), pp. 2097–2108. DOI: 10.1177/1077546320953733.
- [74] A. Kumar and R. Singh. “Application of the Boundary Element Method for Gearbox Noise and Vibration Analysis”. In: *Mechanical Systems and Signal Processing* 60.1 (2015), pp. 387–403. DOI: 10.1016/j.ymssp.2014.11.018.
- [75] Sen M Kuo. “Adaptive active noise control systems: algorithms and digital signal processing (DSP) implementations”. In: *Digital Signal Processing Technology: A Critical Review*. Vol. 10279. SPIE, 1995, pp. 26–52.
- [76] Robin S. Langley, Jeremy R. D. Smith, and Paul G. Bremner. “A hybrid FEA/SEA technique for the analysis of complex systems: Application to plate and beam structures”. In: *The Journal of the Acoustical Society of America* 106.4_Supplement (1999), pp. 2117–2117. ISSN: 0001-4966. DOI: 10.1121/1.427965.
- [77] Giovanni Lapicciarella, Jens Rohlfing, and M.G. Tehrani. *Optimal placement of six inertial mass actuators for MIMO active vibration control on a laboratory truss structure*. 2017.

- [78] Giovanni Lapicciarella, Jens Rohlfing, and M.G. Tehrani. *Optimal placement of six inertial mass actuators for MIMO active vibration control on a laboratory truss structure*. 2017.
- [79] J. Lee and H. Park. “Boundary Element Method for Analysis of Gearbox Vibration Modes”. In: *International Journal of Mechanical Sciences* 139 (2018), pp. 485–494. DOI: 10.1016/j.ijmesci.2018.03.006.
- [80] Lucyna Leniowska and Dominik Mazan. “MFC Sensors and Actuators in Active Vibration Control of the Circular Plate”. In: *Archives of Acoustics* 40.2 (2015), pp. 257–265. DOI: 10.1515/aoa-2015-0028.
- [81] Mingfeng Li et al. “Actuator design and experimental validation for active gearbox vibration control”. In: *Smart Materials and Structures* 15.1 (2006), pp. 1–6. ISSN: 0964-1726. DOI: 10.1088/0964-1726/15/1/N01.
- [82] K. B. LIM. “Disturbance Rejection Approach to Actuator and Sensor Placement”. In: *Journal of Guidance, Control, and Dynamics* 20.1 (1997), pp. 202–204. ISSN: 0731-5090. DOI: 10.2514/2.4022.
- [83] S-F Liu et al. “DC bias dependence of piezoelectric properties of < 111 > oriented Pb (Zn/sub 1/3/Nb/sub 2/3/) O/sub 3/-PbTiO/sub 3/single crystals”. In: *Proceedings of the 13th IEEE International Symposium on Applications of Ferroelectrics, 2002. ISAF 2002*. IEEE, 2002, pp. 427–430.
- [84] Yang Lu, Fengjiao Wang, and Xunjun Ma. “Helicopter interior noise reduction using compounded periodic struts”. In: *Journal of Sound and Vibration* 435 (2018), pp. 264–280. ISSN: 0022-460X. DOI: <https://doi.org/10.1016/j.jsv.2018.07.024>.
- [85] Richard H. Lyon, Richard G. DeJong, and Manfred Heckl. “Theory and Application of Statistical Energy Analysis, Second Edition”. In: *The Journal of the Acoustical Society of America* 98.6 (1995), pp. 3021–3021. ISSN: 0001-4966. DOI: 10.1121/1.413875.
- [86] P. G. Maghami and S. M. Joshi. “Sensor-Actuator Placement for Flexible Structures with Actuator Dynamics”. In: *Journal of Guidance, Control, and Dynamics* 16.2 (1993), pp. 301–307. ISSN: 0731-5090. DOI: 10.2514/3.56599.
- [87] Dario Magliacano et al. “Feasibility study for a tonal vibration control system of a mounting bracket for automotive gearboxes”. In: *International Journal of Mechanics* 10 (2016), pp. 403–410.
- [88] D Magliacano et al. “Active vibration control of a mounting bracket for automotive gearboxes”. In: *Int. J. Mech Eng* 1 (2016), pp. 69–74.
- [89] Gargi Majumder and Rajiv Tiwari. “Experimental study on vibration control of spur geared rotor system with active magnetic bearings”. In: *Journal of Sound and Vibration* 532 (2022), p. 117005. ISSN: 0022-460X. DOI: <https://doi.org/10.1016/j.jsv.2022.117005>.

- [90] Howard M. Matt and Francesco Lanza Di Scalea. “Macro-fiber composite piezoelectric rosettes for acoustic source location in complex structures”. In: *Smart Materials and Structures* 16.4 (2007), pp. 1489–1499. ISSN: 1361-665X. DOI: 10.1088/0964-1726/16/4/064.
- [91] Krzysztof Mazur, Stanislaw Wrona, and Marek Pawelczyk. “Design and implementation of multichannel global active structural acoustic control for a device casing”. In: *Mechanical Systems and Signal Processing* 98 (2018), pp. 877–889. ISSN: 08883270. DOI: 10.1016/j.ymssp.2017.05.025.
- [92] Krzysztof MAZUR et al. “FXLMS with Multiple Error Switching for Active Noise-Cancelling Casings”. In: *Archives of Acoustics* 44.4 (2019), pp. 775–782.
- [94] J. Minkoff. “The operation of multichannel feedforward adaptive systems”. In: *IEEE Transactions on Signal Processing* 45.12 (1997), pp. 2993–3005. ISSN: 1941-0476. DOI: 10.1109/78.650259.
- [95] S. O. Reza Moheimani, Dunant Halim, and Andrew J. Fleming. *Spatial control of vibration: Theory and experiments*. Vol. v. 10. Series on stability, vibration, and control of systems. Series A. River Edge, N.J.: World Scientific, 2003. ISBN: 978-981-279-428-4.
- [96] Gerald T. Montague et al. “Feedforward Control of Gear Mesh Vibration Using Piezoelectric Actuators”. In: *Shock and Vibration* 1.5 (1994), p. 959651. DOI: <https://doi.org/10.3233/SAV-1994-1507>. eprint: <https://onlinelibrary.wiley.com/doi/pdf/10.3233/SAV-1994-1507>.
- [97] Kirsten Morris and Michael A. Demetriou. “Using H2-control metrics for the optimal actuator location of infinite-dimensional systems”. In: *2010 American Control Conference*. Ed. by IEEE Staff Corporate Author. IEEE, 2010, pp. 4899–4904. ISBN: 978-1-4244-7427-1. DOI: 10.1109/ACC.2010.5530915.
- [98] Kirsten Morris and Steven Yang. “Comparison of actuator placement criteria for control of structures”. In: *Journal of Sound and Vibration* 353 (2015), pp. 1–18. ISSN: 0022460X. DOI: 10.1016/j.jsv.2015.05.002.
- [99] Tatsuya Murao et al. “Mixed-error approach for multi-channel active noise control of open windows”. In: *Applied Acoustics* 127 (2017), pp. 305–315. ISSN: 0003-682X. DOI: 10.1016/j.apacoust.2017.06.024.
- [102] Harald Naunheimer et al. *Automotive Transmissions*. Berlin, Heidelberg: Springer Berlin Heidelberg, 2011. DOI: 10.1007/978-3-642-16214-5.
- [103] Sherif Okda. “Development of Actuator-Amplifier Systems for Active Vibration Control of Gearboxes”. PhD Thesis. Darmstadt: Technische Universität Darmstadt, 2024. DOI: <https://doi.org/10.26083/tuprints-00027879>.

- [106] Akash Pandey and A. Arockiarajan. “Actuation performance of macro-fiber composite (MFC): Modeling and experimental studies”. In: *Sensors and Actuators A: Physical* 248 (2016), pp. 114–129. ISSN: 0924-4247. DOI: 10.1016/j.sna.2016.07.022.
- [107] Cosima Du Pasquier and Kristina Shea. “Actuator placement optimization in an active lattice structure using generalized pattern search and verification”. In: *Smart Materials and Structures* 30.11 (2021), p. 115007. DOI: 10.1088/1361-665X/ac24ef.
- [108] Jamie Pears et al. *Investigation of methods to predict parallel and epicyclic gear transmission error*. Tech. rep. SAE Technical Paper, 2005.
- [109] Jamie Pears et al. “Predicting Variation in the NVH Characteristics of an Automatic Transmission using a Detailed Parametric Modelling Approach”. In: *SAE Technical Paper Series*. SAE Technical Paper Series. SAE International 400 Commonwealth Drive, Warrendale, PA, United States, 2007. DOI: 10.4271/2007-01-2234.
- [110] André Preumont. *Vibration Control of Active Structures*. Vol. 246. Cham: Springer International Publishing, 2018. DOI: 10.1007/978-3-319-72296-2.
- [111] B. Rebbechi, Carl Howard, and Colin Hansen. “Active control of gearbox vibration”. In: *Proceedings of the Active Control of Sound and Vibration Conference* (1999), pp. 295–304.
- [112] D Sachau and S Jukkert. “Real-time implementation of the frequency-domain FxLMS algorithm without block delay for an adaptive noise blocker”. In: *Proceedings of the ISMA, Leuven, Belgium* (2014), pp. 15–17.
- [113] Carsten Schmitt. “Beitrag zur Prädiktion von Schalltransferpfaden in Fahrzeuggetrieben”. PhD thesis. Technische Universität Chemnitz, 2019.
- [114] Thomas Schneider. “Lightweight construction: First composite gearbox housing with layer-optimized organo sheeting weighs 30% less than a comparable aluminum component”. In: *Reinforced Plastics* 63.1 (2019), pp. 40–45. DOI: 10.1016/j.repl.2017.11.018.
- [115] Daniel Schweigert et al. “Advanced method of including housing stiffness into calculation of gear systems”. In: *Forschung im Ingenieurwesen* 86.2 (2022), pp. 241–248. ISSN: 1434-0860. DOI: 10.1007/s10010-022-00585-z.
- [116] Sridhar N Shastry and S Subrahmanya Swamy. “Study on High Frequency Vibrations using Statistical Energy Analysis for Different Composite Materials”. In: *IOP Conference Series: Materials Science and Engineering* 925.1 (2020), p. 012044. DOI: 10.1088/1757-899X/925/1/012044.
- [117] Li Shu, Wang Bo, and Hu Ji-zhong. “Sensitivity analysis based on Lanczos algorithm in structural dynamics”. In: *Applied Mathematics and Mechanics* 24 (2003), pp. 92–98. DOI: 10.1007/BF02439382.

-
- [118] Luo Shun-an et al. “Active vibration control of gear drive system based on FxRLS algorithm”. In: *2017 International Conference on Advanced Mechatronic Systems (ICAMechS)*. 2017, pp. 1–4. DOI: 10.1109/ICAMechS.2017.8316472.
- [119] Smart Material GMBH. *Macro Fiber Composites - Overview*. 2021.
- [120] J.D. Smith. *Gear Noise and Vibration*. Mechanical engineering (Marcel Dekker) : a series of textbooks and reference books. Marcel Dekker, 1999. ISBN: 9780824760052.
- [121] Henry A. Sodano, Gyuhae Park, and Daniel J. Inman. “An investigation into the performance of macro-fiber composites for sensing and structural vibration applications”. In: *Mechanical Systems and Signal Processing* 18.3 (2004), pp. 683–697. ISSN: 08883270. DOI: 10.1016/S0888-3270(03)00081-5.
- [122] Jung Woo Sohn, Juncheol Jeon, and Seung-Bok Choi. “An Investigation on Dynamic Signals of MFC and PVDF Sensors: Experimental Work”. In: *Advances in Mechanical Engineering* 5 (2013), p. 420345. ISSN: 1687-8140. DOI: 10.1155/2013/420345.
- [123] Britta Späh. “Schwingungsbeeinflussung geometrisch komplexer Strukturen mittels piezoelektrischer Flächenwandler am Beispiel des Getriebeheulens”. PhD thesis. Darmstadt: Technische Universität Darmstadt, 2015.
- [124] Britta Späh, Rudolf Sebastian Schittenhelm, and Stephan Rinderknecht. “Optimal Sensor and Actuator Placement for Active Vibration Control Systems”. In: vol. ASME 2012 Noise Control and Acoustics Division Conference. Noise Control and Acoustics Division Conference. New York, 2012. DOI: 10.1115/NCAD2012-0982.
- [125] Tyler H. Summers and John Lygeros. “Optimal Sensor and Actuator Placement in Complex Dynamical Networks”. In: *IFAC Proceedings Volumes* 47.3 (2014), pp. 3784–3789. ISSN: 14746670. DOI: 10.3182/20140824-6-ZA-1003.00226.
- [126] Wei Sun et al. “Active Gear Pair Vibration Control Based on Filtered-X RLS Algorithm”. In: *Advances in Power Transmission Science and Technology*. Vol. 86. Applied Mechanics and Materials. Trans Tech Publications Ltd, 2011, pp. 166–169. DOI: 10.4028/www.scientific.net/AMM.86.166.
- [127] Wenhao Sun et al. “A Comparative Study Based on Different Control Algorithms for Suppressing Multistage Gear Transmission System Vibrations”. In: *Shock and Vibration* 2018 (2018), pp. 1–16. ISSN: 1070-9622. DOI: 10.1155/2018/7984283.
- [128] David C Swanson. *Signal processing for intelligent sensor systems with MATLAB*. CRC Press, 2011.
- [129] Julian Theling, Jens Brimmers, and Christian Brecher. “Reducing mass while improving the operational behavior: form optimization of planetary gearbox housings”. In: *Forschung im Ingenieurwesen* 85.2 (2021), pp. 543–551. ISSN: 1434-0860. DOI: 10.1007/s10010-021-00445-2.

- [130] V. Tzoumas et al. “Minimal actuator placement with optimal control constraints”. In: *2015 American Control Conference (ACC)*. 2015, pp. 2081–2086. DOI: 10.1109/ACC.2015.7171040.
- [131] Rafet Can Ümütlü et al. “Effect of inner stiffeners on vibration and noise levels of gearbox housing without changing the mass”. In: *Journal of Measurements in Engineering* 7.2 (2019), pp. 58–66. DOI: 10.21595/jme.2019.20337.
- [132] Han Wang et al. “Experimental Analysis of an Active Vibration Frequency Control in Gearbox”. In: *Shock and Vibration* 2018 (2018), pp. 1–9. DOI: 10.1155/2018/1402697.
- [133] Han Wang et al. “Multi-stage gear vibration active control based on AFPID control”. In: *2017 International Conference on Advanced Mechatronic Systems (ICAMechS)*. 2017, pp. 1–6. DOI: 10.1109/ICAMechS.2017.8316477.
- [134] C. Weber, G. Niemann, and K. Banaschek. *Formänderung und Profilrücknahme bei gerad- und schrägverzahnten Rädern*. Schriftenreihe Antriebstechnik. Vieweg, 1955.
- [135] D. Williams et al. “Active vibration control using piezoelectric actuators employing practical components”. In: *Journal of Vibration and Control* 25.21-22 (2019), pp. 2784–2798. ISSN: 1077-5463. DOI: 10.1177/1077546319870933.
- [136] Stanislaw Wrona and Marek Pawelczyk. “Active reduction of device narrowband noise by controlling vibration of its casing based on structural sensors”. In: *Proceedings of the 22nd International Congress on Sound and Vibration, Florence, Italy*. 2015, pp. 12–16.
- [137] Tao Wu et al. “Optimization of the location of piezoelectric actuator and sensor in active vibration control using Multi-Verse Optimizer algorithm”. In: *Journal of Intelligent Material Systems and Structures* 34.4 (2023), pp. 401–414. DOI: 10.1177/1045389X221111537.
- [138] Yasunori Kanda et al. “Experimental Transfer Path Analysis of Gear Whine”. In: SAE International, 2005. ISBN: 2688-3627. DOI: 10.4271/2005-01-2288.
- [139] Yuji Ogata, Satoru Suzuki, and Masami Hiraoka. “Development of Topology Optimization Method for Reduction of Transmission Housing Weight”. In: SAE International, 2005. ISBN: 2688-3627. DOI: 10.4271/2005-01-1699.
- [140] Philipp Zech. “Aktive Reduktion modulierter Zahneingriffsvibrationen von Planetengetrieben”. PhD thesis. Darmstadt, 2019.
- [141] Philipp Zech, Daniel Fritz Plöger, and Stephan Rinderknecht. “Active control of planetary gearbox vibration using phase-exact and narrowband simultaneous equations adaptation without explicitly identified secondary path models”. In: *Mechanical Systems and Signal Processing* 120 (2019), pp. 234–251. ISSN: 08883270. DOI: 10.1016/j.ymssp.2018.10.030.

-
- [142] Feng Zhang et al. “Application of Multichannel Active Vibration Control in a Multistage Gear Transmission System”. In: *Shock and Vibration* 2022.1 (2022), p. 9970106. DOI: <https://doi.org/10.1155/2022/9970106>.
- [143] Hui-fu Zhang and Wei Kang. “Design of the Data Acquisition System Based on STM32”. In: *Procedia Computer Science* 17 (2013), pp. 222–228. ISSN: 1877-0509. DOI: [10.1016/j.procs.2013.05.030](https://doi.org/10.1016/j.procs.2013.05.030).
- [144] Wen Zhang and Jun Xu. “Advanced lightweight materials for Automobiles: A review”. In: *Materials & Design* 221 (2022), p. 110994. ISSN: 0264-1275. DOI: <https://doi.org/10.1016/j.matdes.2022.110994>.
- [145] G. Zhao et al. “Adaptive-passive control of structure-borne noise of rotating machinery using a pair of shunted inertial actuators”. In: *Journal of Intelligent Material Systems and Structures* 27 (2015). DOI: [10.1177/1045389X15600080](https://doi.org/10.1177/1045389X15600080).
- [146] Xiaojin Zhu et al. “Analysis and implementation of MIMO FULMS algorithm for active vibration control”. In: *Transactions of the Institute of Measurement and Control* 34.7 (2012), pp. 815–828.
- [147] Y. Zhu et al. “Simultaneous optimal design of structural topology, actuator locations and control parameters for a plate structure”. In: *Computational Mechanics* 29 (2002), pp. 89–97. ISSN: 1432-0924. DOI: [10.1007/s00466-002-0316-0](https://doi.org/10.1007/s00466-002-0316-0).
- [148] David C. Zimmerman and Daniel J. Inman. “On the nature of the interaction between structures and proof-mass actuators”. In: *Journal of Guidance, Control, and Dynamics* 13.1 (1990), pp. 82–88. ISSN: 0731-5090. DOI: [10.2514/3.20520](https://doi.org/10.2514/3.20520).

List of Publications from this work

- [100] Sneha Rupa Nampally, Mauro Fontana, Rainer Nordmann, and Stephan Rinderknecht. “Derivation of Sensor-Actuator Layout for Active Control of Gearbox Housing Vibration”. In: vol. Volume 12: 35th Conference on Mechanical Vibration and Sound (VIB). International Design Engineering Technical Conferences and Computers and Information in Engineering Conference. 2023, V012T12A011. DOI: [10.1115/DETC2023-110297](https://doi.org/10.1115/DETC2023-110297).
- [101] Sneha Nampally, Sherif Okda, Mauro Fontana, Rainer Nordmann, and Stephan Rinderknecht. “Experimental Studies on the Influence of Static Torque in a Novel Gearbox Test-Rig”. In: *Book of Abstracts and Selected Papers - 7th European Conference on Structural Control*. Vol. 7. 2022, pp. 210–216. ISBN: 978-83-65550-37-8.
- [104] Sherif Okda, Sneha Rupa Nampally, Mauro Fontana, Sven Herold, Rainer Nordmann, Stephan Rinderknecht, and Tobias Melz. “Active vibration control of gearbox housing using inertial mass actuators”. In: *Smart Materials and Structures* (2024).

-
- [105] Sherif Okda, Sneha Nampally, Mauro Fontana, Sven Herold, Rainer Nordmann, Stephan Rinderknecht, and Tobias Melz. “Experimental Vibro-Acoustic Analysis of Gearbox Behavior Using Piezoelectric Stack Actuator Excitation”. In: *Book of Abstracts and Selected Papers - 7th European Conference on Structural Control*. Vol. 7. 2022, pp. 217–222. ISBN: 978-83-65550-37-8.

Standards

- [24] *Calculation of load capacity of spur and helical gears — Part 1: Basic principles, introduction and general influence factors*. ISO 6336-1:2019. Geneva, CH: International Organization for Standardization, 2019.
- [93] *Methods for the calibration of vibration and shock transducers — Part 21: Vibration calibration by comparison to a reference transducer*. ISO 16063-21:2003/Amd 1:2016. Geneva, CH: International Organization for Standardization, 2016.